technische universität
dortmund

Optical Electron-Spin Tomography and Hole-Spin Coherence Studies in (In,Ga)As/GaAs Quantum Dots

Dissertation

submitted in partial fulfillment of
the requirements for the degree of

Dr. rer. nat.

to the Faculty of Physics
TU Dortmund University, Germany

by

Steffen Varwig

Dortmund, September 2014

Contents

1 Introduction

The field of *quantum computing* or rather the search for systems that can be used for the realization of quantum information processing is one of the big issues in modern physics [Ste98]. Such systems are formed by quantum mechanical quantities, which can serve as a so-called *quantum bit* (qubit), the unit of information in a quantum computer analogous to a bit in a classical computer, and interactions between them. In contrast to classical bits, a qubit cannot only be in either of two states $|0\rangle$ or $|1\rangle$, but also in a superposition $|\psi\rangle = \alpha |0\rangle + \beta |1\rangle$ of them. A system of several n qubits can then be used to perform 2^n logical operations in parallel [Sto04], leading to a tremendous increase in the processing speed for complex mathematical problems. As an example, the prime factorization of large numbers, as it is used for encryption nowadays, would be possible in months or days instead of several thousand years with adequate quantum algorithms [Sho97]. Moreover, quantum computers would enable the simulation of any physical, especially quantum mechanical, system [Fey82].

Generally, any quantum mechanical quantity with two distinguishable states can serve as a qubit. As an example, this could be realized by the two orthogonal polarizations of a photon or the up and down states of a spin-1/2 particle. However, in any case the system shall fulfill a few basic requirements in order to be implemented as a qubit, which were formulated as the *DiVincenzo criteria* [DiV00]:
(1) The system shall provide *well characterized qubits* and shall be *scalable*. The internal Hamiltonian and coupling to other qubits and external fields shall be known. It shall in principle be possible to extend the number of qubits within the system.
(2) It shall be possible to *initialize* the system to a simple (reference) state. The starting point of any operation shall be known.
(3) A universal set of *logical quantum gates* shall be provided. These are unitary transformations acting on one or more qubits. The transformations are generated by interactions, which need to be turned on and off during certain time frames.
(4) The quantum mechanical *coherence time*, the “qubit lifetime”, shall be as long as possible, at least much longer than the gate operation times.
(5) It shall be possible to measure, to *read out*, every individual qubit reliably.
Without going into further details of quantum information processing, it is clear that the physics of the quantum system hosting the qubits need to be well-known and therefore need to be studied with regard to these five criteria.

There are several approaches for qubit implementations, which all have certain advantages and disadvantages in this respect. Early promising qubit realizations were presented in the field of nuclear magnetic resonance (NMR), where the nuclear spins of hydrogen or other atoms of dissolved molecules are manipulated by pulsed radio-frequency fields [Chu98, Jon98]. Even at room temperature, the coherence times are sufficiently long here, but the number of qubits is limited to the number of atoms in each molecule [Sto04]. Another system that has been used for implementing basic quantum algorithms is provided by ionized atoms in electromagnetic traps [Gul03, Bri05]. They provide well isolated qubits, which can easily be read out, but the interactions between them are challenging to control [Sto04]. A third example of qubit implementations is given by superconducting circuits. Here, the presence or absence of a Cooper pair or the direction of the superconductive current can serve as a qubit [Cla08, DiC09]. An advantage of this solid-state implementation is that the qubits can be coupled via simple electrical elements [Dev04]. On the other hand, a strong coupling to the environment and material imperfections substantially reduce the coherence time of superconducting qubits [Pai11].

Another appealing solid-state approach of implementing qubits, which is studied in this thesis, is represented by carrier spins in semiconductor nanostructures. As a two-level system, the spin of an electron is an obvious qubit candidate. An essential advantage of semiconductor-based systems over liquid state NMR or trapped ions, which may be way ahead in terms of the number of entangled qubits [Mon11], is their integration capability into the existing silicon-based information technology [Llo93]. The electron's spin degree of freedom is of high interest in any case, as it is (in addition to its charge) exploited, e. g., to reduce the energy dissipation in electronic components such as spin-based transistors or diodes in the so-called *spintronics* [Bur00, Wol01]. Electron-spin qubits in semiconductor structures can be addressed electrically [Now07], but also optically. Selection rules of interband transitions allow for the spin orientation, manipulation, and the read-out of quantum information. In this way, spatially confined qubits could be transformed into "flying" qubits, photons, which are already used for data transfer today and could couple spatially separated spin qubits.

The electron and hole spins, which are subject of this thesis, are confined in semiconductor *quantum dots* (QDs). In such a low-dimensional structure, the carriers are decoupled from many environmental influences so that the spin coherence times are prolonged by two orders of magnitude compared to those in bulk semiconductor materials [Kik98, Pet05]. The spatial confinement on the scale of nanometers also leads to a discretization of the energy levels offering precisely addressable optical transitions with large dipole moments [Gam02]. Thus, the qubit initialization and gate operations can be performed on a picosecond timescale by means of short laser pulses. To increase the weak optical response for the spin-qubit read-out, not a single spin, but an ensemble of QD spins is addressed, although single-spin qubits are often preferred to avoid inhomogeneities [War13]. These inhomogeneities broaden the transition linewidth and lead to a fast carrier-spin dephasing. On the other hand, ensembles offer a scalable pool of qubits and might enhance the mutual interactions, which are necessary for gate operations [Wei13].

In previous works on QD electron-spin ensembles by A. Greilich and S. Spatzek, it was shown that the inhomogeneous spin dephasing can be overcome by (i) temporally periodic excitation pulses, leading to a discretization and phase synchronization of spin precession modes contributing to the measured signal (*spin mode-locking*, see Sec. 2.3.1) [Gre06b, Gre07a], or (ii) by additional laser-pulse trains which rotate the spins by a desired angle at a certain time (see Sec. 2.3.2). The latter can be exploited to invert the dephasing process within the ensemble and create *spin echoes*, which reveal the coherence [Gre09a, Spa11a]. Together with an external magnetic field these optically induced spin rotations enable to reorient the spins along any direction in space. This can be used to switch an orientation-dependent interaction between two spin ensembles, each representing a qubit, on and off. Such an interaction between two spin subsets within one QD ensemble was introduced in Refs. [Spa11a] and [Spa11c] (see Sec. 2.4). It was shown that a continuous phase shift in the precession of one spin subset emerges when another subset is oriented parallel or antiparallel to the first one. A theoretical model describing this behavior also predicts the buildup of a spin-vector component along the magnetic field, which shall be zero in absence of the interaction. However, this component could not yet be measured with the standard *pump-probe technique* used for the optical orientation and detection of QD electron-spin dynamics, which is only sensitive to the spin component along the optical axis perpendicular to the external field (see Sec. 3.1).

In Chap. 4 of this thesis, the tool of optical spin rotations is further exploited to implement an all-optical spin tomography measurement, by which the spin component along the magnetic field in presence of the spin-spin interaction can be obtained. The idea is to rotate the spin vector precessing in an external magnetic field by an angle of $\pi/2$ at a certain moment during the precessional evolution so that the spin component in the precession plane is replaced by the component along the field, which can then be measured. Such a tomography measurement is essential to gain full information on a qubit or an entangled qubit pair, and has not yet been developed optically. In addition to that, an experiment is presented, which reveals the orientation patterns of mode-locked spins in a dephased spin ensemble by adjusting the excitation protocol so that higher harmonics of the fundamental spin precession frequency can be observed. The chapter targets on gathering novel insight into the spin-spin interaction and implementing a read-out technique that allows the measurement of all spin-vector components.

Studies on QD hole-spin coherence in similar semiconductor QD ensembles are up to now less advanced compared to those on electron spins in such structures. However, hole spins might be an interesting qubit candidate as their coherence time is expected to be longer than that of electrons, because the shape of their valence band p-orbitals should lead to a much weaker interaction with the nuclear spin bath, which was found to be the main source for electron-spin decoherence [Mer02, Kha02]. The effects of the hole-nuclear spin interaction on the hole-spin mode-locking in a QD ensemble are studied in the first part of Chap. 5. The second part of this chapter focuses on the hole-spin coherence time and especially its dependence on the temperature. In the last part of Chap. 5 an experiment is presented in which a pulse sequence is used to dynamically decouple the hole spins from interactions with the environment in order to prolong their coherence time.

The thesis presents a promising expansion of the sophisticated optical techniques for manipulating electron spins in QD ensembles and novel approaches to address hole spins in such systems. It thus represents a treatment of the DiVincenzo criteria (3) and (5) for electron spins as well as criterion (4) for hole spins in semiconductor QD structures.

2 Physical background

In this chapter, an overview of essential physical concepts and results of previous studies on topics related to this work is given. It provides fundamental information to understand the subsequently presented experiments.

2.1 (In,Ga)As/GaAs quantum dots

The charge carriers, whose spins are subject to the studies of this work, are not free particles; they are confined in semiconductor quantum dots (QDs). In this section the embedding materials InAs and GaAs and the concept of self-assembled QDs are introduced briefly.

2.1.1 Energy level structure in InAs and GaAs

Indium arsenide (InAs) and Gallium arsenide (GaAs) are compound semiconductors. Their elements are listed in the third (Indium, Gallium) and fifth (Arsenic) main group of the periodic table and therefore they are commonly called III-V semiconductors. Both crystallize in the same cubic crystal structure called zincblende. It is formed by two interpenetrating face-centered cubic lattices resulting in a structure similar to diamond, but with altering elements at neighboring lattice sites [Kit89]. The lattice constant for InAs is $a_{\mathrm{InAs}} = 6.06\,\text{Å}$, while it is $a_{\mathrm{GaAs}} = 5.65\,\text{Å}$ for GaAs [Sik01].

These III-V compounds are direct band gap semiconductors, i. e., the minimum of the conduction band and the maximum of the valence band are at the same value in k-space. An extract of the band structure of bulk InAs is exemplarily shown in Fig. 2.1. At room temperature $T = 300\,\mathrm{K}$ the energy gap between the conduction band (CB) and the valence band (VB) is $E_{\mathrm{g}}^{\mathrm{InAs}} = 0.354\,\mathrm{eV}$. The band structure of GaAs is similar to the one of InAs, but the band gap is $E_{\mathrm{g}}^{\mathrm{GaAs}} = 1.424\,\mathrm{eV}$ [Sik01]. For very low temperatures close to $0\,\mathrm{K}$ the CB is empty, while the VB is completely filled with electrons. They can be excited into the CB by thermal or, e.g., optical means, leaving a vacancy in the VB behind. This vacancy can be treated as a positively charged carrier and is called *hole.* In the vicinity of the Γ point at $k = 0$ the energy dispersion of the CB and the three valence subbands are assumed to be parabolic [Dya08]. The inverse of their second derivative or curvature determines the effective mass of the respective charge carrier. This accounts for the descriptions

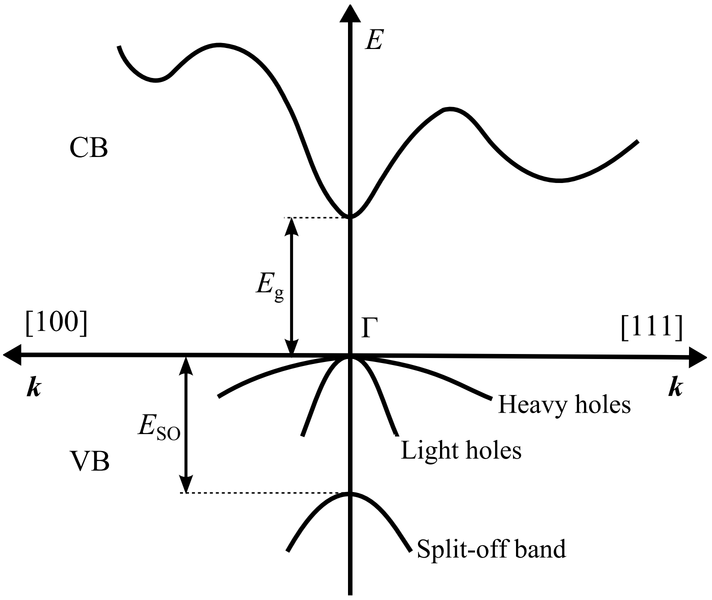

Figure 2.1 Band structure of bulk InAs in the vicinity of the Γ point. The minimum of the conduction band (CB) is separated by an energy gap E_g from the maximum of the valence Band (VB). The two hole subbands are degenerate in energy for $k = 0$, while the third subband is split-off by E_{SO}. According to Ref. [Sik01].

light and *heavy* for the holes occupying the two upper valence subbands. The valence band structure can be described by the Luttinger Hamiltonian [Lut56].

The lowest state in the conduction band has an orbital angular momentum of $l = 0$ and is hence called s-type referring to atomic physics. At zero magnetic field it is twofold degenerate with spin eigenvalues $m_s = \pm 1/2$. The p-type valence band has $l = 1$ and would be threefold degenerate ($m_l = 0, \pm 1$), if the spin was disregarded. However, the spin does not only double the number of states, but also couples to the orbital angular momentum. This spin-orbit coupling originates from the fact that in the frame of reference of an electron with orbital angular momentum the charged nuclei circulate [Dya08]. This leads to an effective magnetic field acting on the electron spin vector $\boldsymbol{S}$. In a simplified form the spin-orbit (SO) coupling can be written as

$$H_{SO} = \lambda_{SO} \boldsymbol{L} \cdot \boldsymbol{S} \; . \tag{2.1}$$

The orbital momentum vector $\boldsymbol{L}$ and the factor λ_{SO} depend on the state of the electron [Dya08], i. e., the occupied band, its Bloch wave function, and the distance from the nucleus. Considering the total angular momentum $\boldsymbol{J} = \boldsymbol{L} + \boldsymbol{S}$ one finds two energy levels in the valence band at $k = 0$, one with $j = 3/2$ and one with $j = 1/2$. The latter is split-off by the spin-orbit energy E_{SO} (see Fig. 2.1), which is 0.41 eV for InAs and 0.34 eV for GaAs. These values are on the order of the InAs band gap and can be neglected for the experiments discussed in this work. For $k \neq 0$ the $j = 3/2$ level splits into the heavy hole ($m_j = \pm 3/2$) and the light hole ($m_j = \pm 1/2$) subband. Each of them is twofold spin degenerate. At $k = 0$ they form a fourfold degenerate energy level in ideal bulk crystals. However, this degeneracy between heavy and light holes is lifted in QDs (see next Sec. 2.1.2). The mixing of heavy and light hole states and the problems arising from the description of the heavy-hole spin by its total angular momentum j instead of the pure spin s are discussed in Sec. 2.2.2.

All three elements Indium, Gallium, and Arsenic also carry a nuclear spin. The common isotopes ^{113}In and ^{115}In have the nuclear spin $I_{\mathrm{In}} = 9/2$; ^{69}Ga, ^{71}Ga, and ^{75}As each have $I_{\mathrm{Ga}} = I_{\mathrm{As}} = 3/2$ [Way61]. These nuclear spins or rather their magnetic moments induce a nuclear magnetic field $\boldsymbol{B}_{\mathrm{n}}$ that interacts with the electron and hole spins. This is known as hyperfine (HF) interaction. In a general form it can be written as

$$H_{\mathrm{HF}} = \lambda_{\mathrm{HF}} \boldsymbol{I} \cdot \boldsymbol{S} \ , \tag{2.2}$$

with $\boldsymbol{I}$ being the nuclear spin vector. The parameter λ_{HF} depends on the spatial position $\boldsymbol{r}$ of the electron (or hole) with respect to the magnetic dipole of the nucleus. Since the field of a magnetic dipole is singular at $r = 0$, the HF interaction is separated into two contributions [Sch02]: (1) The Fermi-contact interaction is valid for an infinitesimally small sphere around the nucleus, if the electron wave function does not vanish there ($\psi(r = 0) \neq 0$). In this case, λ_{HF} is directly proportional to the probability amplitude at the nucleus $|\psi(0)|^2$. This affects, e. g., electrons in the conduction band with their s-type wave function. The Fermi-contact interaction strongly influences the dynamics of electron spins in QDs, which is discussed in Sec. 2.2.3. (2) The dipole-dipole interaction applies for the region outside this sphere. Here, λ_{HF} decreases with r and is in most cases much weaker than the Fermi-contact interaction [Dya08]. It plays a role when the carrier wave function does not overlap with that of the nucleus, as for the club-shaped p-orbitals of holes in the valence band. In this case, the interaction also depends on the angle between the orbital axis and the magnetic moment of the nucleus [Den02].

2.1.2 Quantum dots

The electronic properties of electrons and holes change when they are confined in a potential well of a size comparable to their de Broglie wavelength. If this potential well confines the carriers in all three dimensions on a nm scale, it is called quantum dot (QD). In such a zero-dimensional system, the density of states is reduced to delta functions. In contrast to the energy bands in bulk crystals, the level structure in QDs is discrete [Gyw10].

Such QDs are built as heterostructures of similar semiconductor materials with different band gap energies. (In,Ga)As/GaAs QDs are type-I heterostructures [Ivc04]. Here, 10^4 to 10^5 atoms [Mal09] of a semiconductor with lower CB and higher VB energies are surrounded by a semiconductor with higher CB and lower VB energies. Hence, the embedded atoms serve as a potential trap for both electrons and holes, which can be temporarily excited or resident in doped structures. Figure 2.2(a) illustrates this situation for an n-doped InAs QD surrounded by GaAs. The CB and

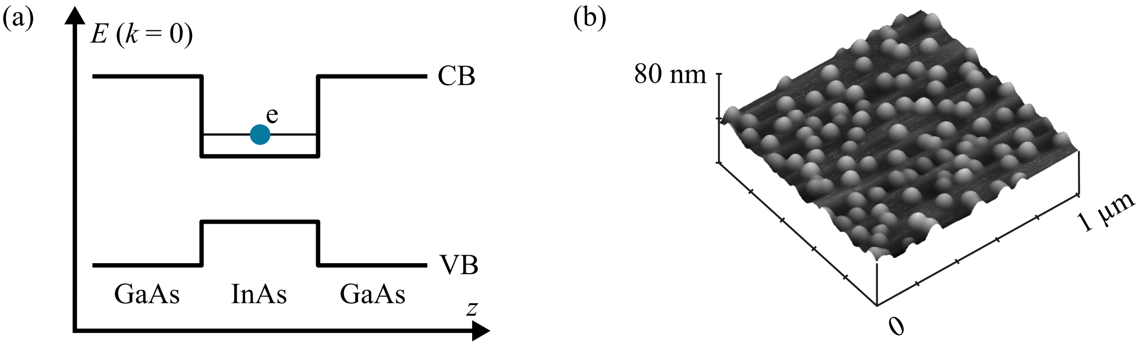

Figure 2.2 (a) Schematic illustration of a QD formed of InAs surrounded by GaAs. The conduction band (CB) and valence band (VB) energies at $k = 0$ are depicted as a function of the spatial z direction. The semiconductor with smaller band gap (InAs) serves as a potential trap for charge carriers, here a resident electron. **(b)** Atomic force micrograph of self-assembled QDs before annealing or capping. The islands are formed from two monolayers of InAs that were grown on a GaAs substrate. The height of each island is about 9 nm; the base diameter is about 30 nm. From Ref. [Boc10], modified.

VB energies at $k = 0$ are schematically drawn as a function of a spatial direction, here the z direction, which corresponds to the growth direction (see below).

Beside direct fabrication methods like lithography and etching, QDs are often grown by the self-assembling *Stranski-Krastanov* method [Str39]. It allows very clean and defect-free material compositions. Considering (In,Ga)As/GaAs QDs, very few monolayers of InAs are deposited on GaAs by molecular beam epitaxy [Her96]. At a critical thickness the strain caused by the different lattice constants of InAs and GaAs coaxes the InAs atoms to lump and to form pyramidal islands [Cus96]. The density and size of the islands can be adjusted to some extent by the molecular beams and the temperature during the growth process; however, the island positions are randomly distributed. QDs formed in this way are usually 5 to 10 nm high and the base is about 20 to 30 nm wide [Gyw10]. An atomic force micrograph of such a QD layer is shown in Fig. 2.2(b). As a next step, the QD islands are covered with GaAs and additional QD layers before a final GaAs capping can be grown. After that, the sample can be annealed by heating up to temperatures around 900 °C. Thereby, lattice defects are reduced, the QD geometries are homogenized, and Ga and In atoms diffuse into and out of the QDs, respectively. As a result, the band gap energies of different QDs equalize, reducing the inhomogeneous broadening of the ensemble emission linewidth, and shift to higher values.

Resident charge carriers can be embedded into QDs by depositing, e. g., Silicon a few nanometers beneath each QD layer. This doping provides additional electrons that become localized inside the QDs. Unintentionally, crystal impurities can also serve as electron donors or acceptors and lead to resident carriers in QDs.

Due to the spatial confinement of the carriers and the strain between the two materials, the energy level structure in QDs is altered compared to the case of bulk crystals (Sec. 2.1.1). The confinement leads to a discretization of the density of states. For a QD described above, the in-plane confinement along x and y can be modeled by a radially symmetric two-dimensional harmonic oscillator. The solutions are equidistant energy levels for electrons and holes that are named s, p, d, ... shells referring to atomic physics. The QD height is about three times smaller than its base diameter. Hence, the confinement in growth direction z is stronger, such that only the lowest energy state is relevant [Gyw10].

The confinement along z also leads to an increase in energy of the light hole subband with respect to the heavy-hole subband at the Γ point. However, this increase is mostly overcompensated by strain effects, which also lifts the degeneracy between heavy and light holes at $k = 0$ [Gyw10]. The absolute value and direction of the splitting depends on the magnitude and sign of the strain, whether it is compression or stretch [Cus96]. Typically, the heavy-hole–light-hole splitting $E_{\text{HH-LH}}$ is assumed to be a few 10 meV and positive, i. e., the heavy-hole subband is higher in energy and thus providing the ground state for holes [Kre09].

2.2 Spin basics

The spin of a particle is an intrinsic property that manifests in magnetic fields. A mathematical description of the spin is discussed in the following. The electron as a fermion with spin $s = 1/2$ can have two eigenvalues $m_s = \pm 1/2$ of the spin projection S_z along the quantization axis z.[1] The corresponding eigenstates will in the following be referred to as

$$\begin{aligned} |s_z\rangle_+ &= |{}^1\!/\!_2, +{}^1\!/\!_2\rangle = |\!\uparrow\rangle \quad \text{(up)}, \\ |s_z\rangle_- &= |{}^1\!/\!_2, -{}^1\!/\!_2\rangle = |\!\downarrow\rangle \quad \text{(down)}. \end{aligned} \tag{2.3}$$

In this two-dimensional basis the full spin vector $\boldsymbol{S}$ can be described by the Pauli matrices:

$$\boldsymbol{S} = \begin{pmatrix} S_x \\ S_y \\ S_z \end{pmatrix} = \frac{\hbar}{2} \begin{pmatrix} \sigma_x \\ \sigma_y \\ \sigma_z \end{pmatrix} , \tag{2.4}$$

$$\sigma_x = \begin{pmatrix} 0 & 1 \\ 1 & 0 \end{pmatrix} , \; \sigma_y = \begin{pmatrix} 0 & -\mathrm{i} \\ \mathrm{i} & 0 \end{pmatrix} , \; \sigma_z = \begin{pmatrix} 1 & 0 \\ 0 & -1 \end{pmatrix} . \tag{2.5}$$

An arbitrary spin state

$$|\psi\rangle = \alpha\,|\!\uparrow\rangle + \beta\,|\!\downarrow\rangle \tag{2.6}$$

---

[1] It should be noted that the quantization axis, chosen without loss of generality, coincides with the optical axis in the experiments. Unlike in many textbooks introducing the spin, it does not coincide with the direction of the external magnetic field, which will be along the x direction (*Voigt geometry*).

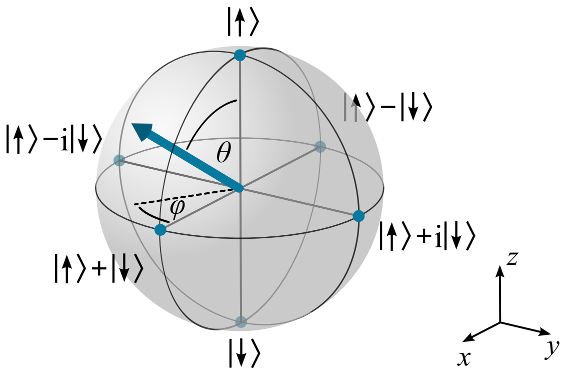

Figure 2.3 Bloch sphere representation of an arbitrary spin 1/2 state given by Eq. (2.7). North and south pole correspond to the eigenstates $|\uparrow\rangle$ and $|\downarrow\rangle$, respectively. All other points on the sphere are superpositions of them. The normalization prefactor $1/\sqrt{2}$ of the equatorial states is omitted for clarity. According to Ref. [Gyw10].

is given by the superposition of the eigenstates with complex coefficients α and β satisfying the normalization condition $|\alpha|^2 + |\beta|^2 = 1$. Neglecting a global phase, this condition allows for a description of a spin state by two angles θ and ϕ:

$$|\psi\rangle = \cos\frac{\theta}{2}\,|\uparrow\rangle + \mathrm{e}^{\mathrm{i}\phi}\sin\frac{\theta}{2}\,|\downarrow\rangle \quad . \tag{2.7}$$

These angles can be considered as the polar and the azimuthal angle of any coordinate on a sphere. This sphere is called *Bloch sphere* and can serve as a representation of any two level system and its complex superpositions. Figure 2.3 shows a Bloch sphere representing the spin state given by Eq. (2.7). The north pole and the south pole correspond here to the eigenstates $|\uparrow\rangle$ and $|\downarrow\rangle$, respectively. In this picture the expectation values of the spin components in Eq. (2.4) are equivalent to the components of the *Bloch vector* pointing from the center of the Bloch sphere to its surface, depicted by the blue arrow in Fig. 2.3 [Gyw10]:

$$\langle \boldsymbol{S}\rangle = \langle\psi|\,\boldsymbol{S}\,|\psi\rangle = \frac{\hbar}{2}\begin{pmatrix}\cos\phi\sin\theta\\ \sin\phi\sin\theta\\ \cos\theta\end{pmatrix} . \tag{2.8}$$

2.2.1 Larmor precession

The electron spin couples to a magnetic field as described by the Zeeman Hamiltonian

$$H_B = \frac{g_\mathrm{e}\mu_\mathrm{B}}{\hbar}\boldsymbol{B}\cdot\boldsymbol{S} . \tag{2.9}$$

Bohr's magneton $\mu_\mathrm{B} = \frac{e\hbar}{2m_0}$ is given by the elementary charge e and the electron mass m_0. g_e is the effective Landé g factor, which describes the magnetic moment of the electron spin in relation to the magnetic moment of a classical angular momentum of the same value and hence the strength of the Zeeman interaction. In self-assembled QDs the electron g factor is mostly determined by the band gap, which slightly varies from dot to dot within an ensemble [Sch11]. The g factor dispersion follows the Roth-Lax-Zwerdling relation [Rot59]

$$g_{\mathrm{e}}(E_{\mathrm{g}}) = g_0 \left[1 - \left(\frac{m_0}{m_{\mathrm{e}}}\right) \frac{E_{\mathrm{SO}}}{3E_{\mathrm{g}} + 2E_{\mathrm{SO}}}\right] , \tag{2.10}$$

with $g_0 \approx 2$ being the g factor of a free electron and m_{e} the QD electron's effective mass. In (In,Ga)As/GaAs QD structures as used in the experiments of this work, the g factor dispersion can be assumed to be nearly linear [Sch11].

Assuming a magnetic field $\boldsymbol{B} = (B, 0, 0)^T$ along the x axis, the Zeeman Hamiltonian can be written as

$$H_B = \frac{g_{\mathrm{e}}\mu_{\mathrm{B}}B}{2} \begin{pmatrix} 0 & 1 \\ 1 & 0 \end{pmatrix} , \tag{2.11}$$

using the Pauli matrix σ_x. In this form it is clear that there is no energy splitting between the basis states $|\uparrow\rangle$ and $|\downarrow\rangle$. However, the two superposition states

$$|s_x\rangle_{\pm} = \frac{1}{\sqrt{2}} \left(|\uparrow\rangle \pm |\downarrow\rangle\right) \tag{2.12}$$

along the magnetic field axis x are split by the Zeeman energy

$$\Delta E_B = g_{\mathrm{e}}\mu_{\mathrm{B}}B =: \hbar\omega_{\mathrm{L}} \, . \tag{2.13}$$

The introduced frequency ω_{L} is called *Larmor frequency* and determines a precession of the spin components perpendicular to the magnetic field axis. This can be understood by looking at the time evolution of a spin state $|\psi\rangle$, which can be shown to be given by

$$|\psi(t)\rangle = \mathrm{e}^{-\frac{\mathrm{i}H_B}{\hbar}t} |\psi\rangle = \left[\cos\left(\frac{\omega_{\mathrm{L}}}{2}t\right) \mathbb{1} - \mathrm{i}\sin\left(\frac{\omega_{\mathrm{L}}}{2}t\right) \sigma_x\right] |\psi\rangle \; . \tag{2.14}$$

The time-dependent expectation value of the spin vector $\boldsymbol{S}$ can then be calculated from Eqs. (2.7), (2.8) and (2.14):

$$\langle \boldsymbol{S}(t)\rangle = \langle\psi(t)|\, \boldsymbol{S}\, |\psi(t)\rangle = \frac{\hbar}{2} \begin{pmatrix} \cos\phi\sin\theta \\ \sin\phi\sin\theta\cos(\omega_{\mathrm{L}}t) - \cos\theta\sin(\omega_{\mathrm{L}}t) \\ \sin\phi\sin\theta\sin(\omega_{\mathrm{L}}t) + \cos\theta\cos(\omega_{\mathrm{L}}t) \end{pmatrix} \; . \tag{2.15}$$

It describes a precession of the spin vector about the magnetic field axis x with the Larmor frequency ω_{L}. For an arbitrary initial spin orientation with $S_z^0 = \frac{\hbar}{2}\cos\theta$ and $S_y^0 = \frac{\hbar}{2}\sin\phi\sin\theta$ the time evolution of the z component can be simplified to

$$S_z(t) = S_z^0 \cos(\omega_{\mathrm{L}}t) + S_y^0 \sin(\omega_{\mathrm{L}}t) \; . \tag{2.16}$$

This is only valid for spins perfectly isolated from the environment. Damping of the oscillations due to relaxation processes and dephasing are discussed in Sec. 2.2.3.

2.2.2 Hole-spin peculiarities

In contrast to electrons in the conduction band with an s-type wave function, holes in the valence band have a p-type wave function with non-vanishing angular momentum. Therefore, holes cannot be treated as pure spin states in a two-dimensional Hilbert space, but the total angular momentum $\boldsymbol{J}$ has to be considered. Neglecting the split-off states with $j = 1/2$ (see Sec. 2.1.1) the total angular momentum of the hole has to be written in a four-dimensional basis of heavy ($m_j = \pm 3/2$) and light hole ($m_j = \pm 1/2$) states [Dya84]:

$$\begin{aligned} |{}^3\!/\!_2, +{}^3\!/\!_2\rangle &= -\frac{1}{\sqrt{2}}(|X\rangle + \mathrm{i}\,|Y\rangle)\,|{\uparrow}\rangle \\ |{}^3\!/\!_2, +{}^1\!/\!_2\rangle &= -\frac{1}{\sqrt{6}}(|X\rangle + \mathrm{i}\,|Y\rangle)\,|{\downarrow}\rangle + \sqrt{\frac{2}{3}}\,|Z\rangle\,|{\uparrow}\rangle \\ |{}^3\!/\!_2, -{}^1\!/\!_2\rangle &= +\frac{1}{\sqrt{6}}(|X\rangle - \mathrm{i}\,|Y\rangle)\,|{\uparrow}\rangle + \sqrt{\frac{2}{3}}\,|Z\rangle\,|{\downarrow}\rangle \\ |{}^3\!/\!_2, -{}^3\!/\!_2\rangle &= +\frac{1}{\sqrt{2}}(|X\rangle - \mathrm{i}\,|Y\rangle)\,|{\downarrow}\rangle \ . \end{aligned} \tag{2.17}$$

$|X\rangle\,, |Y\rangle\,, |Z\rangle$ are the orbital parts of the hole states. In this basis the three components of $\boldsymbol{J} = (J_x, J_y, J_z)^T$ are [Lég07]:

$$\begin{aligned} J_x &= \frac{\hbar}{2}\begin{pmatrix} 0 & \sqrt{3} & 0 & 0 \\ \sqrt{3} & 0 & 2 & 0 \\ 0 & 2 & 0 & \sqrt{3} \\ 0 & 0 & \sqrt{3} & 0 \end{pmatrix} \\ J_y &= \frac{\hbar}{2}\begin{pmatrix} 0 & -\sqrt{3}\mathrm{i} & 0 & 0 \\ \sqrt{3}\mathrm{i} & 0 & -2\mathrm{i} & 0 \\ 0 & 2\mathrm{i} & 0 & -\sqrt{3}\mathrm{i} \\ 0 & 0 & \sqrt{3}\mathrm{i} & 0 \end{pmatrix} \\ J_z &= \frac{\hbar}{2}\begin{pmatrix} 3 & 0 & 0 & 0 \\ 0 & 1 & 0 & 0 \\ 0 & 0 & -1 & 0 \\ 0 & 0 & 0 & -3 \end{pmatrix} \ . \end{aligned} \tag{2.18}$$

The coupling of holes to a magnetic field is described in bulk or an isotropic environment, where x and y are equivalent ($D_{2\mathrm{d}}$ symmetry), by the following Hamiltonian [Ivc04]:

$$H_B^{\mathrm{h}} = g_0\mu_{\mathrm{B}}\left[K\boldsymbol{J}\boldsymbol{B} + Q(J_x^3 B_x + J_y^3 B_y + J_z^3 B_z)\right] \ . \tag{2.19}$$

Here K and Q are dimensionless parameters. Although the heavy-hole–light-hole splitting ($E_{\text{HH-LH}} > 10\,\mathrm{meV}$, see Sec. 2.1.2) often exceeds the spectral width of the excitation laser[2] in optical experiments, one cannot neglect the light holes and reduce the problem to the two-dimensional heavy hole subspace. If one did, the in-plane components of the new total angular momentum $\tilde{J}_x$ and $\tilde{J}_y$, and hence the coupling to a magnetic field, described by an effective transverse hole g factor g_h, would be zero [Kes90]: for a magnetic field in x direction, e. g., the first term in Eq. (2.19) that is proportional to K would vanish for $\tilde{J}_x = 0$, and, although $\tilde{J}_x^3$ (and $\tilde{J}_y^3$) would not be zero in the heavy hole subspace, it was found that $Q \ll 1$ and the coupling would be too weak to contribute significantly to g_h [Kou04]. However, a vanishing magnetic coupling is in contradiction to experimental findings including the ones presented in Chap. 5.

The explanation for that is a mixing of heavy and light hole states in realistic QDs, which results from a symmetry reduction induced by local deformations, varying chemical compositions, or asymmetric strain. The latter can be described by the Bir-Pikus Hamiltonian [Lég07], whose off-diagonal entries mix heavy and light hole states. In strain-free QDs the Luttinger Hamiltonian mixes the states in case of an asymmetric in-plane confinement potential due to the QD shape [Bel10, Kou04]. Due to this mixing, QD holes cannot be treated as pure heavy hole or pure light hole states, but rather as mixed states [Kri05]

$$|\psi_\mathrm{h}\rangle_\pm \propto |\pm{}^3\!/_2\rangle - \frac{\rho}{E_\text{HH-LH}} \mathrm{e}^{\pm 2\mathrm{i}\vartheta} \, |\mp{}^1\!/_2\rangle \ . \tag{2.20}$$

The degree of mixture is determined by the coefficient ρ and the angle ϑ, which characterizes the mixing mechanism.

In the two-dimensional basis of Eq. (2.20) one can rewrite the Zeeman Hamiltonian for holes in QDs in the presence of an in-plane magnetic field $\boldsymbol{B} = (B_x, B_y, 0)^T$, introducing a hole pseudospin with components $\tilde{S}_x = -\sigma_x \hbar/2$ and $\tilde{S}_y = \sigma_y \hbar/2$, as [Kou04]

$$H_B^\mathrm{h} = \frac{\mu_\mathrm{B}}{\hbar} \tilde{S}_i g_{\mathrm{h},ij} B_j \ . \tag{2.21}$$

The effective g factor tensor is given by

$$g_\mathrm{h} = g_0 \frac{2\sqrt{3} K \rho}{E_\text{HH-LH}} \begin{pmatrix} -\cos 2\vartheta & \sin 2\vartheta \\ \sin 2\vartheta & \cos 2\vartheta \end{pmatrix} \ . \tag{2.22}$$

This allows for an electron-like description of the hole with pseudospin 1/2 and an effective g factor, which is inversely proportional to the heavy-hole–light-hole splitting. The corresponding hole states will in the following be denoted as $|\psi_\mathrm{h}\rangle_+ = |\Uparrow\rangle$ (up) and $|\psi_\mathrm{h}\rangle_- = |\Downarrow\rangle$ (down).

---

[2] This is valid for continuous wave lasers or Fourier limited pulses longer than a picosecond. The pulses used in the experiments of this work have a spectral width of 1.5 meV, see Sec. 3.2.

2.2.3 Spin coherence and dephasing

For quantum computing the coherence time of a carrier spin is crucial. Only within this time, in which amplitude and phase of the spin wave function are completely correlated [Gru02], quantum information processing is possible. Although the confinement serves as a protection against environmental influences, the coherence time of an electron or hole spin in a QD cannot be infinite. The spin is still subject to elastic and inelastic relaxation processes that limit the lifetime of quantum information.

Inelastic processes are mainly governed by scattering events with phonons. Here, energy is transferred to the lattice, which is why the characteristic time T_1 is often called spin-lattice relaxation time. It is also known as longitudinal relaxation time, since it describes the time, in which the spin component parallel to a magnetic field reaches the thermal equilibrium, one of the two energy eigenstates. At low temperatures ($\mathrm{T} < 10\,\mathrm{K}$) the phonon density is reduced and the relaxation time T_1 in QDs can be in the range of milliseconds depending on the temperature and the magnetic field [Kro04].

Elastic processes that do not change the energy of the spin determine the transverse relaxation time T_2. It is the time in which the transverse components of the spin in respect to a magnetic field axis vanish. The phase information of the quantum state is lost due to a randomization of the phase angle between the two energy eigenstates.[3] There are several mechanisms that can cause this randomization of the transverse spin orientation in bulk, see Ref. [Dya08]. They all describe temporal fluctuations of randomly oriented (effective) magnetic fields about which the spin precesses for a short moment of time, e. g., during or between scattering events. For localized electrons in III-V semiconductor QDs the Fermi-contact interaction with the nuclear surrounding, Sec. 2.1.1, is the origin of the dominant transverse relaxation mechanism [Kha02, Mer02]. Fluctuations in strength and orientation of the nuclear magnetic field lead to random irreversible precessions and hence to a loss of phase information in the spin state. In the studied QD structures of this work the transverse electron spin relaxation time T_2^{e} was found to be about a microsecond at temperatures below 10 K [Gre06b]. With increasing temperature the nuclear fluctuations increase as well and T_2^{e} drops to a few nanoseconds at 50 K [Her08]. The underlying relaxation mechanisms for hole spins in QDs are part of the study of this work and are discussed in Sec. 5.2.

In general, both longitudinal and transverse relaxation processes lead to a loss of phase information and hence to a loss of coherence. However, since at low temperatures $T_2 \ll T_1$, the coherence time is limited by the transverse relaxation time. Therefore, in the following the *spin coherence time* is referred to as T_2.

For a spin that is subject to relaxation processes the time evolution in an external magnetic field has to be extended by a damping factor. In the description of the

---

[3] If $|\uparrow\rangle$ and $|\downarrow\rangle$ were the energy eigenstates, this phase angle would correspond to ϕ in Eq. (2.7).

spin dynamics by the *Bloch equations* [Blo46, Gyw10]

$$\frac{d}{dt}\begin{pmatrix} S_x \\ S_y \\ S_z \end{pmatrix} = \frac{g\mu_\mathrm{B}}{\hbar}\begin{pmatrix} S_x \\ S_y \\ S_z \end{pmatrix} \times \begin{pmatrix} B \\ 0 \\ 0 \end{pmatrix} - \begin{pmatrix} \frac{1}{T_1} & & 0 \\ & \frac{1}{T_2} & \\ 0 & & \frac{1}{T_2} \end{pmatrix}\begin{pmatrix} S_x - S_x^\infty \\ S_y \\ S_z \end{pmatrix} \tag{2.23}$$

it results from the second term describing the relaxation to the equilibrium state $\boldsymbol{S}(t \to \infty) = (S_x^\infty, 0, 0)^T$. The first term describes the Larmor precession and provides the same solution as given in Eq. (2.16). To solve the Bloch equations one has to decouple the system of differential equations by introducing $S_\pm = S_z \pm \mathrm{i}S_y$. The result for S_z is then:

$$S_z(t) = \left[S_z^0 \cos(\omega_\mathrm{L} t) + S_y^0 \sin(\omega_\mathrm{L} t)\right] \mathrm{e}^{-t/T_2} \; . \tag{2.24}$$

Although this exponential description of the damping can be inaccurate for some relaxation mechanisms, it is a common assumption that is appropriate in most cases [Kha02].

In addition to the loss of coherence, the overall spin polarization of an ensemble might decrease on an even faster timescale due to *inhomogeneous dephasing*:[4] The Larmor precession frequencies of the carrier spins differ slightly from dot to dot in a QD ensemble. Therefore, an initially aligned spin ensemble runs out of phase while the spins precess about an external magnetic field. The main origin of this inhomogeneous dephasing is the dispersion of g factors in a QD ensemble [Gre06a]. It can arise from varying effective band gap energies (see Eq. (2.10), valid for electrons) or from variations in the mixing of heavy-hole and light-hole states (see Sec. 2.2.2) due to different QD geometries [Kot01, Ivc04]. The characteristic inhomogeneous dephasing time $T_{2,g}^\mathrm{inh}$ is then determined by the width of the Larmor frequency distribution $\Delta\omega_{\mathrm{L},g}$ given by the width of the g factor distribution Δg and the strength of the external magnetic field [Bes05]:

$$\frac{1}{T_{2,g}^\mathrm{inh}} \sim \frac{\Delta g \mu_\mathrm{B} B}{\hbar} \, . \tag{2.25}$$

Another contribution to the inhomogeneous dephasing is the precession about an effective hyperfine field $\boldsymbol{B}_\mathrm{n}$ of fluctuating nuclear spins, which varies from dot to dot and causes an ensemble dephasing even at zero external magnetic field [Mer02]. The zero-field dephasing time $T_{2,\mathrm{n}}^\mathrm{inh}$ is determined by the width of the distribution $\Delta\omega_{\mathrm{L,n}}$ of precession frequencies in the field of (frozen) nuclear spin fluctuations given by its width ΔB_n [Yug12]:

$$\frac{1}{T_{2,\mathrm{n}}^\mathrm{inh}} \sim \frac{g\mu_\mathrm{B}\Delta B_\mathrm{n}}{\hbar} \, . \tag{2.26}$$

---

[4] The term "dephasing" is in many textbooks used to describe the loss of phase in the quantum mechanical spin state during transverse (T_2) relaxation processes, as described above. This could be called *homogeneous dephasing*, in contrast to the dephasing of the overall spin polarization due to inhomogeneities within a QD ensemble, which is described in the following.

The total dephasing time T_2^* of a net spin polarization in a QD ensemble is finally composed by the coherence time and the inhomogeneous dephasing times [Fla02],

$$\frac{1}{T_2^*} = \frac{1}{T_2} + \frac{1}{T_{2,g}^{\mathrm{inh}}} + \frac{1}{T_{2,\mathrm{n}}^{\mathrm{inh}}} \,. \tag{2.27}$$

However, since in a self-assembled QD ensemble the dephasing time is under most experimental conditions much smaller than the coherence time (about two orders of magnitude for electrons at $B = 0.5\,\mathrm{T}$ [Gre06a]), T_2^* is mainly determined by the inhomogeneous contributions. In the studied dot structures of this work, B_n is usually about several ten millitesla for electrons [Oul07, Pet08] so that for external fields in the order of a tesla the nuclear contribution to the dephasing time can be neglected as well. The nuclear contribution to the hole-spin dephasing is studied in Sec. 5.1 of this work and is for now also neglected.

Thus, assuming a Gaussian distribution $f(\omega) \propto \exp\left(-(\omega - \omega_\mathrm{L})^2/2(\Delta\omega_\mathrm{L})^2\right)$ of precession frequencies ω with central frequency ω_L, the time evolution of the z component of the overall spin-ensemble polarization in an external magnetic field is damped with a Gaussian damping factor [Gre07a]:

$$S_z(t) = \left[S_z^0 \cos(\omega_\mathrm{L} t) + S_y^0 \sin(\omega_\mathrm{L} t)\right] \mathrm{e}^{-t^2/2T_2^{*2}} \,. \tag{2.28}$$

It should be noted that the single spin coherence may still be preserved, even though the ensemble has yet dephased, see Sec. 2.3.1.

2.3 Optical spin orientation

The distinct orientation of electron and hole spins in a QD ensemble can be achieved by excitation with polarized light. Although the electric field does not couple directly to the spin, the orientation is possible, because photon induced interband transitions of an electron from the VB to the CB are subject to spin-selective selection rules, which originate from the transition matrix elements in Fermi's golden rule [Sch02].

In bulk crystals the transition matrix elements between the VB states described in Eqs. (2.17) and the CB states in Eqs. (2.3) determine the probability of the absorption (or emission) of a photon [Dya84]. Assuming a left-handed circularly polarized photon (σ^-) with angular momentum $l = -1$ and wave vector $\boldsymbol{k} \parallel \boldsymbol{z}$, only transitions from the $m_j = +3/2$ VB state to the $m_j = +1/2$ CB state or from the $m_j = +1/2$ VB state to the $m_j = -1/2$ CB state are allowed in electric dipole approximation [Sch02]. The relative probabilities of these transitions are determined by the prefactors of the terms $(|X\rangle + \mathrm{i}\,|Y\rangle)$ in the VB states. These transitions correspond to dipoles rotating in the plane perpendicular to $\boldsymbol{k}$ [Dya84]. For a right-handed circularly polarized photon (σ^+) the above considerations are valid with reversed signs for m_j.

In the presence of a heavy-hole–light-hole splitting as described at the end of Sec. 2.1.2 the transitions from the $m_j = +1/2$ VB states (light holes) can be neglected, as long as the linewidth of the exciting photon source does not exceed this splitting. However, due to the heavy-hole–light-hole mixing in (In,Ga)As/GaAs QDs (see Sec. 2.2.2) the VB states cannot be considered as pure heavy or light hole states and the selection rules are more complicated here. For simplicity, the ground state for holes is in the following assumed to have mostly heavy hole character. Thus, a $\sigma^{\mp}$ polarized photon excites an electron from the VB, where it has $m_j = \pm 3/2$, to the CB having $m_j = \pm 1/2$. The residual hole is assigned to $m_j = \mp 3/2$. In the notation of up and down states this excitation process reads

$$|0\rangle \xrightarrow{\sigma^-} |\uparrow\Downarrow\rangle \tag{2.29}$$

$$|0\rangle \xrightarrow{\sigma^+} |\downarrow\Uparrow\rangle \ , \tag{2.30}$$

where $|0\rangle$ is the unexcited QD ground state. The electron-hole pair excited in this way in a neutral QD forms a bound state $|\uparrow\Downarrow\rangle$ ($|\downarrow\Uparrow\rangle$) called *exciton*. In a singly charged QD the excited electron-hole pair and the resident carrier form a charged exciton or *trion* $|\uparrow\downarrow\Uparrow\rangle$ ($|\downarrow\uparrow\Downarrow\rangle$) or $|\Uparrow\Downarrow\downarrow\rangle$ ($|\Downarrow\Uparrow\uparrow\rangle$).

The necessary photon energy for the excitation is the band gap energy E_g reduced by the exciton binding energy. In an external magnetic field along x the addressed up and down states are superpositions of the Zeeman-split energy eigenstates. Therefore, the spectral width of the exciting photon source must additionally cover this Zeeman splitting.[5] In the time domain this condition corresponds to an excitation-pulse duration that is short compared to the spin precession period [Spa11b].

The resonant excitation of a trion can now be exploited to orient the spin of a resident carrier in a singly charged QD by such short laser pulses.[6] This is exemplarily discussed for a negatively charged QD, whose resident electron is initially in an arbitrary spin state given in Eq. (2.6). A resonant, σ^- polarized laser pulse creates a coherent superposition of electron and trion states [Gre06a]

$$|\psi\rangle_{\sigma^-} = \alpha\,|\uparrow\rangle + \beta\cos(\Theta/2)\,|\downarrow\rangle - \mathrm{i}\beta\sin(\Theta/2)\,|\Downarrow\uparrow\downarrow\rangle \ . \tag{2.31}$$

The component initially in the $|\uparrow\rangle$ state (parallel to the injected electron) is not affected by a σ^- pulse due to Pauli blocking. The net electron spin polarization after the pulse is given by $|\alpha|^2 - |\beta|^2\cos^2(\Theta/2)$ and depends on the *pulse area* Θ (see below). The electron component in the trion state does not contribute to the spin polarization, since together with the injected electron it forms a singlet state with vanishing total spin.

---

[5] Assuming, e. g., an electron g factor of 0.5 the Zeeman splitting is $\Delta E_B \approx 30\,\mu\mathrm{eV}$ at $B = 1\,\mathrm{T}$.

[6] The pulses also need to be shorter than the radiative decay times of excitons, and the carrier spin dephasing and coherence times.

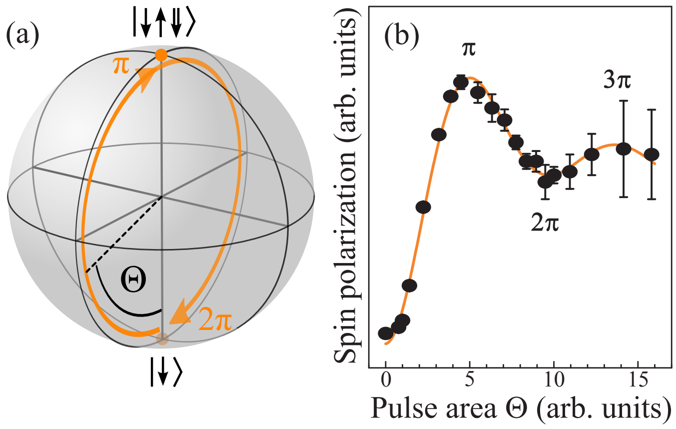

Figure 2.4 **(a)** Pulse area Θ as the polar angle of a Bloch sphere, of which the south pole represents a resident electron and the north pole represents a trion state. A resonant π pulse brings the system from the resident electron state into the trion state, and back when $\Theta = 2\pi$. **(b)** Spin polarization along z as a function of the pulse area. The orange curve is a guide to the eye. From Ref. [Gre06a], modified.

The pulse area $\Theta = 2\int \boldsymbol{d} \cdot \boldsymbol{E}(t)\,dt/\hbar$ is given by the product of the transition matrix element $\boldsymbol{d}$ and the electric field of the light $\boldsymbol{E}$, integrated over the laser pulse duration. It can be interpreted geometrically as the polar angle of a Bloch sphere, of which the south pole represents the resident electron and the north pole represents the trion. This is depicted in Fig. 2.4(a). If the resident electron was initially in the $|\downarrow\rangle$ state ($\alpha = 0$), the probability of occupancy would oscillate between the electron and the trion state with increasing Θ. In two-level atomic systems this is known as *Rabi oscillations* [All87]. For a fixed laser field and continuous excitation this corresponds to an oscillation in time and can be interpreted as alternating excitation and stimulated emission in the two-level system. The same is valid for a fixed pulse duration and increasing electric field or laser power $P \propto \boldsymbol{E}^2$ [Sti01].

An experimental demonstration of the pulse area's influence on the spin polarization is given in panel (b) of Fig. 2.4 taken from Ref. [Gre06a]. It shows the electron spin polarization along the z direction in an ensemble of singly charged QDs as a function of the pulse area, which was calculated from the laser power. The strong damping of the Rabi-like oscillation is assumed to originate from inhomogeneities in the QD ensemble, such as varying dipole moments or effective laser powers [Bor02].

When the pulse parameters are chosen such that $\Theta = \pi$, Eq. (2.31) simplifies to

$$|\psi\rangle^{\pi}_{\sigma^-} = \alpha\,|\uparrow\rangle - \mathrm{i}\beta\,|\Downarrow\uparrow\downarrow\rangle \tag{2.32}$$

and the polarization reaches a maximum. Without external magnetic field this polarization would vanish, after the electron component in the trion has recombined with the hole. However, in an external magnetic field the unexcited electron spin component and the hole spin precess with different Larmor frequencies.[7] When the trion stochastically decays after about 0.5 ns [Gre06a], the additional electron spin component is randomly oriented with respect to the initially unexcited one. Hence,

---

[7] These Larmor frequencies are assumed to be larger than the trion decay rate.

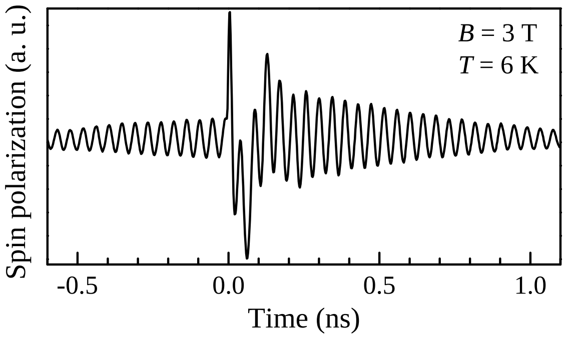

Figure 2.5 Time evolution of the overall spin polarization of a singly negatively charged QD ensemble in an external magnetic field of $B = 3\,\mathrm{T}$. The resident electron spins are oriented periodically every 13.2 ns by circularly polarized excitation pulses. The moment of incidence in the shown time frame defines $t = 0$.

the spin polarization is not completely compensated. By means of periodic excitation the resident electron spin polarization can thus be enhanced. It can become fully polarized after about 10 excitation pulses if the spin precession frequency is a multiple of the laser pulse repetition rate [Sha03]. In an ensemble of spins not all precession frequencies fulfill this condition, but the stochastic trion decay randomizes the positive or negative contributions to the overall spin polarization. Therefore, these contributions average out and a spin polarization of the resident electrons builds up. The mechanism for polarizing resident holes in positively charged QD is analog to the descriptions above.

Figure 2.5 shows a time-resolved measurement of the overall spin polarization in an ensemble of singly negatively charged QDs being periodically excited by circularly polarized laser pulses. In the shown time frame the moment of incidence is defined as time $t = 0\,\mathrm{ns}$. One can clearly see the damped oscillations of resident electron spins precessing and dephasing in an external magnetic field of $B = 3\,\mathrm{T}$. The precession frequency corresponds to an effective g factor of 0.55. During the first 0.5 ns the signal is superimposed by slow hole spin oscillations with a frequency corresponding to an effective g factor of 0.14 that show the trion contribution. After trion recombination these contributions vanish, but the spin polarization of the resident electron ensemble can still be measured. The dephasing time T_2^* is in the order of a nanosecond. However, at a temperature of 6 K the generated electron spin coherence lasts longer than the dephasing time as can be seen from the rising oscillation signal before the excitation pulse incidence, which is 13.2 ns after the previous pulse incidence. This signal rise is due to the *spin mode-locking* effect in an ensemble of spins, which is discussed in the next section.

2.3.1 Spin accumulation by periodic excitation

The spin polarization, which builds up under periodic excitation, depends on certain conditions that are theoretically discussed in this section. In general, the spin polarization of a resident carrier right after an excitation pulse $S_z^{t\to 0^+}$ depends on the spin polarization right before the pulse $S_z^{t\to 0^-}$. For resonant excitation, a pulse

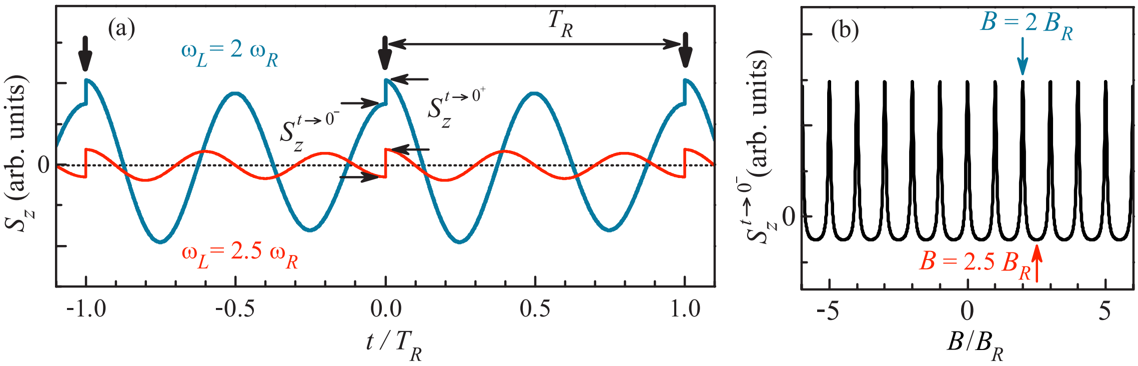

Figure 2.6 **(a)** Time-dependent single spin polarization S_z precessing with $\omega_\mathrm{L} = 2\,\omega_\mathrm{R}$ (blue curve) and $\omega_\mathrm{L} = 2.5\,\omega_\mathrm{R}$ (red curve). The excitation pulses separated by T_R are marked by the thick arrows. **(b)** Spin polarization before an excitation pulse $S_z^{t\to 0^-}$ in dependence of the magnetic field ($B \propto \omega_\mathrm{L}$). The arrows indicate the magnetic fields that correspond to the Larmor frequencies in panel (a). From Ref. [Yug12], modified.

area of $\Theta = \pi$, and assuming instant pulse action, the relation is given by [Yug09]

$$S_z^{t\to 0^+} = \mp\frac{1}{4} + \frac{1}{2} S_z^{t\to 0^-} \,. \tag{2.33}$$

The top (bottom) sign corresponds to σ^+ (σ^-) polarized pulses and resident electrons. For resident holes, the signs need to be inverted. As mentioned above, in an external magnetic field this spin polarization starts to precess about that field. When the spin coherence time T_2 is longer than the repetition period T_R of periodic excitation pulses, the spin polarization, which was induced by a previous pulse, has not vanished yet and determines $S_z^{t\to 0^-}$ before the next pulse. Sign and amplitude of $S_z^{t\to 0^-}$ depend on the precession phase right before the pulse. The phase, in turn, depends on the Larmor frequency, given by the field strength B, and the temporal separation between two pulses T_R. If the precession frequency is a multiple of the pulse repetition rate ω_R, expressed by the phase synchronization condition (PSC) [Gre06b]

$$\omega_\mathrm{L} = N\omega_\mathrm{R} = N\frac{2\pi}{T_\mathrm{R}}\,, \quad N \in \mathbb{N}_0\,, \tag{2.34}$$

then $S_z^{t\to 0^-}$ has the same phase as $S_z^{t\to 0^+}$. Hence, according to Eq. (2.33) the next σ^- (σ^+) pulse enhances the absolute spin polarization, which was in a maximum (minimum) before this pulse. This phenomenon is known as *resonant spin amplification* (RSA). $S_z^{t\to 0^-}$ is then periodic with B and has maxima at multiples of B_R, the field for which $\omega_\mathrm{L} = \omega_\mathrm{R}$. This is illustrated in Fig. 2.6(a). The blue curve shows the calculated time evolution of the spin polarization precessing with $\omega_\mathrm{L} = 2\,\omega_\mathrm{R}$, commensurable with the pulse repetition rate. The phase of precession is in a maximum when the next pulse arrives. In the red curve, ω_L is not commensurable with

ω_R leading to a smaller spin polarization amplitude before and after the excitation pulse. In Fig. 2.6(b) the characteristic RSA peaks in the spin polarization before an excitation pulse $S_z^{t\to 0^-}$ in dependence on the magnetic field ($B \propto \omega_\mathrm{L}$) are exemplarily shown. The actual height and shape of the peaks depend on parameters such as the pulse area or the spin dephasing and coherence time [Yug12].

The above considerations are valid for single spins as well as for an ensemble of spins with a small spread of precession frequencies such that only one (or none, depending on the magnetic field) precession mode can satisfy the PSC [Yug12]. This corresponds to a dephasing time T_2^* that is larger than T_R and can be observed, e. g., in bulk materials [Kik98] or quantum wells [Zhu12]. For QD ensembles, usually another form of resident carrier spin accumulation occurs. Here, the width of the Larmor frequency distribution $\Delta\omega_\mathrm{L}$ is assumed to be so large that the dephasing time T_2^* is smaller than T_R and the ensemble spin polarization vanishes before the next excitation pulse arrives. However, if the single spin coherence is still maintained, the ensemble spin polarization reemerges on a timescale equal to T_2^* before the next pulse (as already shown in Fig. 2.5) [Gre06b]. This signal recovery is due to constructive interference of those precession modes, which satisfy the PSC. Each of these modes accumulate a spin polarization by periodic excitation in the way described above, similar to the RSA. All other modes are pumped less efficiently so that the main contribution to the ensemble spin polarization is only given by the synchronized modes [Yug12]. Referring to synchronized light modes in a laser cavity, this phenomenon is called *spin mode-locking* (SML). Figure 2.7 shows the overall spin polarization of an ensemble containing several modes satisfying the PSC for two different magnetic fields: In the blue curve, the field strength is such that the distribution of Larmor frequencies is centered around $\omega_\mathrm{L} = 10\,\omega_\mathrm{R}$. In the red curve, the central Larmor frequency is $\omega_\mathrm{L} = 7.5\,\omega_\mathrm{R}$, not matching the PSC. However, also in this case enough modes within the frequency distribution satisfy the PSC and interfere constructively before and after the moment of excitation, marked by the arrows, where these modes are in phase.

The spin polarization before the pulse $S_z^{t\to 0^-}$ depends on the pulse area, the radiative trion decay time, the coherence time T_2, and the ratio between the number of modes satisfying the PSC and those, which do not [Yug12]. This ratio can be enhanced, at least for electrons, by nuclear-induced *frequency focusing* [Gre07b]: Although the energy mismatch between the electron and nuclear Zeeman splittings is too large in external magnetic fields to allow spin flip-flop processes between electrons and the QD nuclei, they can occur without energy conservation during the electron-excitation process. Thus, the hyperfine field, which in addition to the external magnetic field determines the Larmor frequency of the electrons, changes. Therefore, also the precession frequency is altered. The nuclear spin flip rate is here proportional to the rate of electron excitation. Hence, the effective magnetic field acting on a resident electron spin changes with every excitation process as long as the PSC is not fulfilled for this electron. This process stops when the sum of the

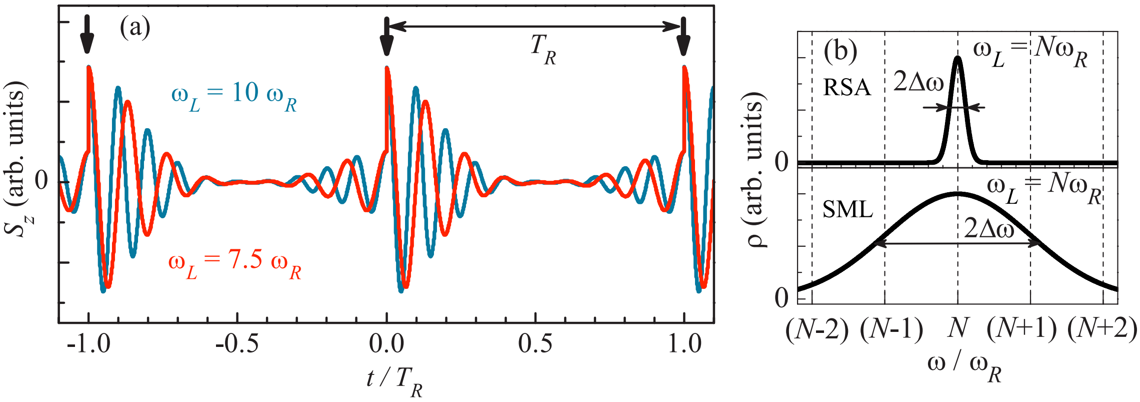

Figure 2.7 **(a)** Time-dependent overall spin polarization of an ensemble containing several modes satisfying the PSC. The magnetic field $B \propto \omega_\mathrm{L}$ is such that the Larmor frequency distribution is centered around $\omega_\mathrm{L} = 10\,\omega_\mathrm{R}$ (blue) or $\omega_\mathrm{L} = 7.5\,\omega_\mathrm{R}$ (red), respectively. **(b)** Precession frequency distribution $\rho(\omega)$ with central frequency $\omega_\mathrm{L} = N\omega_\mathrm{R}$ for $\Delta\omega \equiv \Delta\omega_\mathrm{L} < 0.5\omega_\mathrm{R}$ (RSA) and $\Delta\omega \equiv \Delta\omega_\mathrm{L} > 0.5\omega_\mathrm{R}$ (SML). From Ref. [Yug12], modified.

hyperfine field and the external magnetic field leads to a precession frequency that matches the PSC so that the electron cannot be excited into a trion state anymore due to Pauli blocking. Thereby, the number of electron spins satisfying the PSC and the ensemble spin polarization is enhanced.

Whether the RSA or the SML regime is entered, is determined by the width of the Larmor frequency distribution $\Delta\omega_\mathrm{L}$ in relation to the distance between two neighboring PSC modes ω_R. At least two modes must satisfy the PSC to enter the SML regime. This means that $\Delta\omega_\mathrm{L} > 0.5\omega_\mathrm{R}$ [Yug12]. In Fig. 2.7(b) two precession frequency distributions are depicted, which exemplarily show the conditions for both regimes.

2.3.2 Optically induced spin rotations

Besides the precession about the magnetic field axis x, it is also possible to rotate the QD carrier spin vector about the optical axis z by means of short laser pulses. This is achieved via trion excitation by circularly polarized light, similar to the orientation process described in the beginning of Sec. 2.3. However, the trion state is only virtually excited by a pulse with an area of $\Theta = 2\pi$, which corresponds to a unitary operation that does not leave the spin subspace [Eco10]. In the picture of a Bloch sphere with the electron (or hole) state being the south pole and the trion being the north pole [see Fig. 2.4(a)], the Bloch vector undergoes a full cycle from the electron (or hole) state to the trion state and back to the electron (or hole) state. After that however, it has acquired a phase factor $\mathrm{e}^{-\mathrm{i}\Phi}$, which depends on the

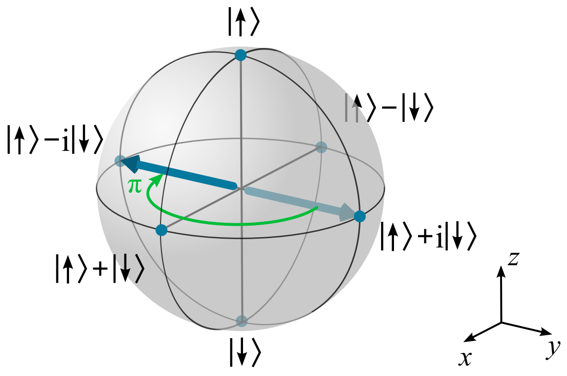

Figure 2.8 Spin rotation by an angle of $\Phi = \pi$ induced by a resonant ($\Delta = 0$) laser pulse with pulse area $\Theta = 2\pi$. The spin vector initially pointing in y direction is rotated towards $-y$.

detuning Δ between the trion resonance and the laser frequency [Eco10]:

$$\Phi = 2\arctan\left(\frac{\sigma}{\Delta}\right) \ . \tag{2.35}$$

Here, σ is the bandwidth of the laser pulse. In case of resonance ($\Delta = 0$), an electron initially in an arbitrary spin state [Eq. (2.6)] will, according to Eq. (2.31), end up in the state

$$|\psi\rangle^{2\pi}_{\sigma^-} = \alpha\,|\uparrow\rangle - \beta\,|\downarrow\rangle \tag{2.36}$$

after application of a σ^- polarized 2π pulse. This is a rotation of the spin vector about the z axis by an angle of π. As an example, the rotation of the spin vector from the $+y$ to the $-y$ direction is depicted in Fig. 2.8. The rotation angle is equivalent to the phase angle Φ in Eq. (2.35). Hence, different rotation angles can be achieved by detuning the rotation pulse from the trion resonance.[8]

In an ensemble of spins with different Larmor frequencies, which is subject to dephasing (see Sec. 2.2.3), a spin rotation by an angle of $\pi/2 < |\Phi| \leq \pi$ leads to a rephasing and an increase of the overall spin polarization. This phenomenon is called *spin echo*. Figure 2.9 shows such echoes in a time-dependent measurement of the overall spin polarization in a singly negatively charged QD ensemble; presented in Ref. [Gre09a]. The spins are oriented at time zero and precess in the yz plane about an external magnetic field, $B = 1\,\mathrm{T}$, along x. At a time τ the spins, which have fanned out due to dephasing, are each rotated by an angle of π about the optical axis z. In the direction of precession the spins with lower Larmor frequency are then ahead. The spins with higher Larmor frequency catch up and at the time 2τ the spins are in phase again increasing the overall spin polarization.

---

[8] The pulse area $\Theta = 2\pi$ is independent of the detuning for laser pulses with a temporal envelope proportional to $\mathrm{sech}(\sigma t)$. Such pulses are assumed here; they allow an analytical calculation of the spin-rotation problem [Eco10].

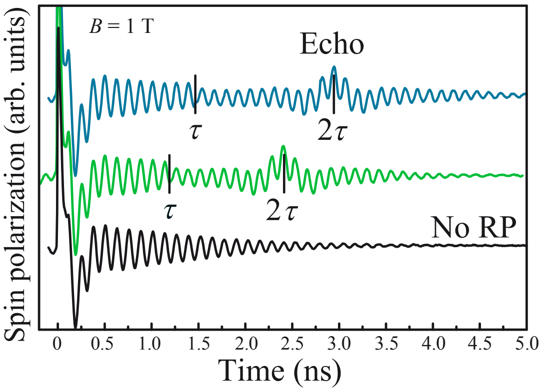

Figure 2.9 Spin echoes in time-dependent measurements of the overall spin polarization in a negatively charged QD ensemble. At a time τ after orientation the precessing and dephasing spins are rotated such that at the time 2τ the spins rephase and form an echo. The lower curve shows the overall spin polarization without any rotation pulse (RP). From Ref. [Gre09a], modified.

2.4 Spin-spin interaction

Recent studies have demonstrated an interaction between two subsets of resident electron spins, each treated as one spin vector $\boldsymbol{S}_1$ and $\boldsymbol{S}_2$, respectively, within one ensemble of QDs [Spa11c]. The two subsets are oriented by two laser-pulse trains of different photon energy so that two subensembles of QDs with different trion resonance energies are addressed. The average spatial QD separation is estimated to be $\sim 100\,\mathrm{nm}$.

The interaction manifests as a continuous shift of the precession phase of one spin subset after orientation of the other subset. Direction and strength of this phase shift depend on the relative orientation of the two spin vectors. An experimental demonstration is given in Fig. 2.10. The figure shows time-resolved measurements of the z component $S_{1,z}$ of one spin subset precessing in an external magnetic field of $B = 1\,\mathrm{T}$. Depending on four selected orientations of the other spin subset $\boldsymbol{S}_2$ relative to $\boldsymbol{S}_1$, depicted by the arrow arrangements, the precession phase is shifted either leftwards for parallel orientation (lower, blue trace), rightwards for antiparallel orientation (lower, red trace), or it is not shifted for orthogonal orientations (upper traces).[9] The absolute phase shifts in the lower traces reach $\pi/2$ with respect to the black reference trace in the middle at $\sim 2.2\,\mathrm{ns}$, emphasized by the vertical line.

Model calculations assuming two single spins interacting with a Heisenberg form $H_{SS} = J\boldsymbol{S}_1 \cdot \boldsymbol{S}_2$, based on the formalism presented in Ref. [Bar11], provide results that are in good agreement with the measured data [Spa11c]. By comparing model and experiment the interaction strength is estimated to be $J \approx 1\,\mu\mathrm{eV}$. The microscopic interaction mechanism is supposed to be the optical RKKY interaction proposed in Ref. [Pie02]. Another consequence of the spin-spin interaction that is predicted by this model is the rise of an x component of the spin vector. However, this x component has not yet been measured in an optical experiment. This

---

[9] The relative orientations are determined at $\sim$4 ns by choosing the time delay and circular polarization of the laser pulses orienting $\boldsymbol{S}_2$ with respect to the ones orienting $\boldsymbol{S}_1$. For details see Ref. [Spa11c].

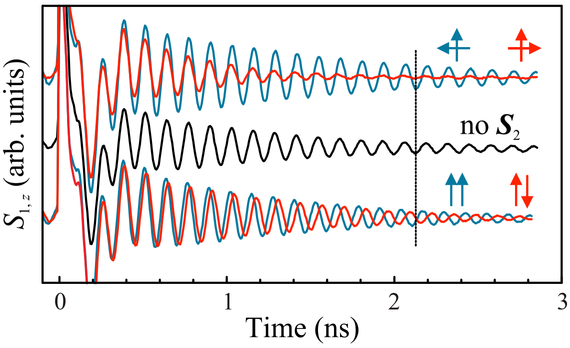

Figure 2.10 Precession phase shifts due to an interaction between two spin subsets within one ensemble of QDs. The z component $S_{1,z}$ of one subset is monitored for four selected orientations of the other subset $\boldsymbol{S}_2$ relative to $\boldsymbol{S}_1$, depicted by the arrow arrangements. The black trace in the middle is a reference without $\boldsymbol{S}_2$ oriented. The magnetic field has $B = 1\,\mathrm{T}$. From Ref. [Spa11c], modified.

measurement is subject of the experiments presented in Sec. 4.2 of this work.

2.5 Faraday rotation and ellipticity

Useful tools to measure the spin polarization are magneto-optical effects that change the polarization of light, transmitted through magnetized or spin polarized matter. In particular by means of short laser pulses such effects can offer time resolved measurements of the fast spin dynamics in semiconductor QDs. The two effects used in this work are the *magnetic circular birefringence*, also known as *Faraday effect* or *Faraday rotation*, and the *magnetic circular dichroism*, henceforth denoted as *ellipticity*. Both effects result from the fact that the complex refractive index $\tilde{n}(\omega) = n(\omega) + i\kappa(\omega)$ and thus the real refractive index n and the extinction coefficient κ of a medium can differ for right-handed and left-handed circularly polarized light of frequency ω, when the medium is magnetized or spin polarized.

Faraday rotation means that the polarization plane of linearly polarized light is rotated by an angle θ_F proportional to the difference of these refractive indices [Buc66]:

$$\theta_\mathrm{F}(\omega) = \frac{\omega d}{2c}\left[n^+(\omega) - n^-(\omega)\right] \; . \tag{2.37}$$

Here d is the travel distance through the medium, c the speed of light, and $n^\pm$ the refractive index of right-handed (σ^+) or left-handed (σ^-) circularly polarized light, respectively. Since linearly polarized light can be described as a superposition of σ^+ and σ^- polarized light of equal electric field amplitudes and fixed phase, the Faraday rotation can be explained by a phase shift of the two circular polarization components due to the different refractive indices or rather the related phase velocities $v^\pm = \frac{c}{n^\pm}$.

Apart from the rotation of the polarization plane, the linearly polarized light gets elliptic, because the two circular polarization components are unequally absorbed due to the different extinction coefficients (or absorption coefficients $\alpha^\pm = \frac{2\omega}{c}\kappa^\pm$) for σ^+ and σ^- polarized light. The ellipticity $\varepsilon = \frac{E^+ - E^-}{E^+ + E^-}$ is defined as the ratio of minor axis to major axis of the polarization ellipse, given by the electric field amplitudes $E^{\pm}$ of $\sigma^{\pm}$ polarized light [Bar04]. For small values it is directly proportional to the difference of the extinction coefficients [Buc66]:[10]

$$\varepsilon(\omega) = \frac{\omega d}{2c} \left[\kappa^{+}(\omega) - \kappa^{-}(\omega)\right] \ . \tag{2.38}$$

The main distinction between Faraday rotation and ellipticity, concerning this work, is the spectral dependence of both quantities. The origin of this dependence can be found in the dielectric function $\epsilon = \tilde{n}^2$, which determines the refractive index and the extinction coefficient. In the Lorentz oscillator model [Kop07] the light-electron interaction in solid media can be described as a harmonic oscillator, driven by the electric field of light. Near the resonance of an electronic transition the complex refractive index can then be written in a simple form as [Gaj10]

$$\tilde{n}(\omega) = 1 + \frac{A}{\omega_0 - \omega - \mathrm{i}\Gamma} \ , \tag{2.39}$$

where A is an amplitude, ω_0 the resonance frequency and Γ the half width at half maximum. Refractive index and extinction coefficient result from this expression as real and imaginary parts, respectively:

$$n(\omega) = \mathrm{Re}\left(\tilde{n}(\omega)\right) = 1 + \frac{A(\omega_0 - \omega)}{(\omega_0 - \omega)^2 + \Gamma^2} \ , \tag{2.40}$$

$$\kappa(\omega) = \mathrm{Im}\left(\tilde{n}(\omega)\right) = \frac{A\Gamma}{(\omega_0 - \omega)^2 + \Gamma^2} \ . \tag{2.41}$$

Like the amplitude of any driven harmonic oscillator, the extinction coefficient describing the absorption of the system has its maximum at the resonance. It is an axis-symmetric function of the light frequency. The refractive index behaves like the phase between driving force and oscillator and is point-symmetric.

The frequency dependence and the absolute value of Faraday rotation and ellipticity is determined by the difference of n^{+} and n^{-}, and κ^{+} and κ^{-}, respectively. The differences can in principle arise from different amplitudes, widths, or spectral positions of the resonance lines for the different circular polarizations of light. In most textbooks the magnetic contribution to the Faraday rotation is discussed, which is due to the difference in the spectral positions of σ^{+} and σ^{-} polarized transitions (see section 2.3) induced by the Zeeman effect in presence of an external magnetic field or an intrinsic magnetization. In this case the difference between n^{+} and n^{-}

---

[10] The ellipticity can also be defined via the angle ψ between the major axis of the polarization ellipse and the diagonal of its circumscribing rectangle [Zve97]. Then $\tan\psi = \varepsilon = \tanh\left(\frac{\omega d}{2c}\left[\kappa^{+} - \kappa^{-}\right]\right)$. For small ellipticities this also reduces to $\psi \approx \varepsilon \approx \frac{\omega d}{2c}\left[\kappa^{+} - \kappa^{-}\right]$ [Bar04].

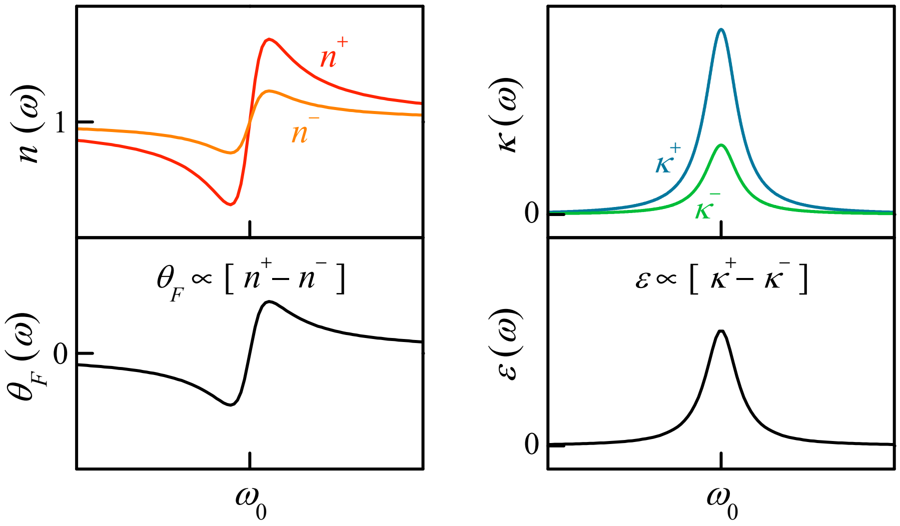

Figure 2.11 Idealized spectral dependences of refractive index n and Faraday rotation θ_{F} (left panel), and extinction coefficient κ and ellipticity ε (right panel). The refractive indices and extinction coefficients for left- and right-handed circularly polarized light $n^{\pm}$ and $\kappa^{\pm}$ are exemplarily calculated from Eqs. (2.40) and (2.41), respectively, for different transition amplitudes A. In this case θ_{F} is an odd and ε is an even function of the detuning between the resonance ω_0 and the light frequency ω.

makes the Faraday rotation an axis-symmetric function of the light frequency with a maximum between the two resonances.

However, for measuring the electron or hole spin polarization in QDs an electronic contribution plays the important role: in spin polarized QDs the degenerate spin levels are unequally occupied, and hence one of the circularly polarized transitions is suppressed due to phase space filling [Cro10]. Therefore the absorption-line amplitude of the corresponding circularly polarization is reduced. Considering the Kramers-Kronig relations it is obvious that also the corresponding refractive index is smaller. This is exemplarily depicted in Fig. 2.11 for the case of a spin polarization in $+z$ direction. As a result, the ellipticity follows the shape of an absorption line and is an even function of the detuning between the resonance and the light frequency, while the Faraday rotation follows the shape of a refractive index and is an odd function of that detuning.

For a given frequency near a resonance both quantities are proportional to the spin polarization along the light wave vector [Gla12]. In an ensemble of QDs the number of resonances contributing to the Faraday rotation or ellipticity is increased and the interpretation of the measured variable can become more complicated in particular cases. Details concerning the experiments in this work are discussed in the corresponding Sec. 5.1. A general discussion of the spectral sensitivity of Faraday rotation and ellipticity measurements on QD ensemble can be found in Ref. [Gla10].

3 Experimental methods

The experimental method to study the carrier spin dynamics in semiconductor QDs used in this work is the well-established pump-probe technique. This technique, which was used and extended, e. g., by A. Greilich and S. Spatzek [Gre07a, Spa11a], is introduced in the following Sec. 3.1. In Sec. 3.2, the optical setups are described including specifications of the used components. The QD samples under study are characterized in Sec. 3.3.

3.1 Time-resolved pump-probe technique

The spin dynamics studied in this work demand a time-resolved measurement technique that can monitor a time frame of about 10 ns at a resolution of about 1 ps. These requirements can be fulfilled by the pump-probe technique, whose concept is the following.

The system under study is periodically excited by a train of laser pulses called *pump*. The state of the system is monitored by measuring specific properties of a second train of laser pulses called *probe*. Given that the pump and probe pulse repetition rates are equal, the measured properties of the probe provide information about the system at a certain time after or before any pump excitation, depending on the delay between the temporal incidences of the pump and probe pulses. This delay can successively be changed and thus the time evolution of the measured property can be recorded step by step. The time-resolved pump-probe technique is not a real-time measurement. Every measurement step, corresponding to a fixed delay between pump and probe pulses, is the average over more than 10^4 pump excitations (see Sec. 3.2.2). The lowest limit of the time resolution is given by either the smallest possible delay increment or the pulse durations.

In this work, the measured property of the probe beam is its polarization, since it can provide information about the spin polarization in the sample under study, as described in Sec. 2.5. The rotation of the polarization plane (Faraday rotation) or the ellipticity of an initially linearly polarized laser beam is changed proportionally to the spin polarization after transmission through the sample. This is schematically depicted in Fig. 3.1. Here, a circularly polarized pump pulse induces a spin polarization (see Sec. 2.3) perpendicular to an external magnetic field B. The Faraday rotation angle and the ellipticity of the transmitted probe light change in dependence of the delay $\Delta t = t_{\mathrm{Probe}} - t_{\mathrm{Pump}}$ between pump and probe pulse incidences,

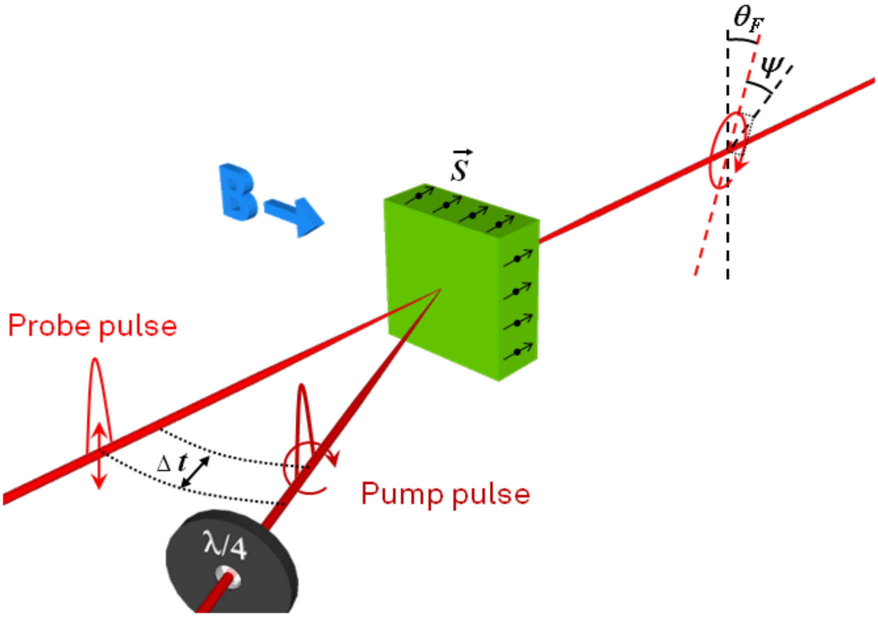

Figure 3.1 Schematic illustration of the pump-probe technique for time-resolved measurements of the spin polarization, e. g., in an external magnetic field B. The Faraday rotation θ_F or ellipticity $\varepsilon = \tan\psi$ can be measured in dependence of the time delay Δt between pump and probe pulses.

since the spins precess and the projection of the spin polarization along the optical axis varies with time. By successively changing the delay, the temporal evolution of the spin polarization before and after orientation by pump pulses can be monitored.

When measuring the resonant spin amplification (RSA), not the delay between pump and probe is varied, but the external magnetic field. The delay is fixed such that the probe pulses arrive shortly before the pump pulses and the spin polarization is determined in dependence of B. It is then not a time-resolved but a frequency-resolved measurement.

3.2 Optical setup

The optical setups used for the experiments in this work are all minor or major extensions of the basic pump-probe setup presented in Ref. [Gre07a]. S. Spatzek extended this setup to implement either rotation pulses or additional pump pulses [Spa11a]. The experiments regarding electron-spin rotations in Sec. 4.1 require similar beam configurations as in Ref. [Spa11a] so that the setup presented there is used with minor changes.

In the tomography experiment, presented in Sec. 4.2, both additional pump and rotation pulses are required simultaneously. To establish the necessary pulse patterns with variable pulse delays, pulse areas, and photon energies, three pulsed laser systems are implemented in the pump-probe setup, which in the largest extend is schematically shown in Fig. 3.2. This setup is explained in the following, exemplarily for all experiments of this work.

The core is a degenerate pump-probe setup (red beams, “Pump 1” and “Probe”); pump and probe beam have the same photon energy, as they are emitted from the same laser system. In the experiments of this work, the lasers are mode-locked Ti:Sapphire lasers (COHERENT MIRA) pumped in turn by Nd:YVO_4 lasers at 532 nm. The Ti:Sapphire laser systems emit pulses with a duration of 2 ps at a repetition rate of 75.75 MHz (repetition period $T_\mathrm{R} = 13.2\,\mathrm{ns}$) exploiting the electro-optical Kerr effect. The output wavelength can be tuned between 700 and 980 nm. The linewidth is about 0.7 nm, which corresponds to $\sim 1\,\mathrm{meV}$ in the range of 880 to 900 nm ($\sim$1.39 eV), as used in the experiments.

In the tomography experiment two additional beams denoted by “Pump 2” (blue) and “Rotation” (green) are used, which demand different photon energies and hence an own laser source. Pump 2 is used to orient a different subensemble of QDs than pump 1 (see Sec. 2.4). The task of the rotation pulses (RP) is to rotate spins as described in Sec. 2.3.2.

Since the pump-probe technique requires the same periodicity for all participating pulse trains, the repetition rates of the different lasers are synchronized by means of electronic synchronization units (COHERENT SYNCHROLOCK-AP). For this purpose, a small part of the pulsed light of the lasers that are to be synchronized is tapped and transmitted to the synchronization units via optical fibers. After comparing the pulse repetition rates with the one of a defined “master” laser, a voltage is applied to piezo actuators changing the position of one mirror in the cavity of the other “slave” lasers such that the repetition rates match. The synchronization is done with an accuracy $< 1\,\mathrm{kHz}$ corresponding to a jitter time of $< 100\,\mathrm{fs}$.

The optical paths of both pumps and the rotation beam are detoured each by passing a retroreflector mounted on an adjustable delay line (OWIS LIMES 170-1000-HSM). In this way the pulse arrival times can be adjusted among each other and with respect to the probe pulses. The accuracy of positioning these retroreflectors is 3 µm so that the minimal delay step is 20 fs. The maximal delay range, limited by the total travel range of 1 m, is enhanced by installing a second retroreflector in front of the delay line (not shown in Fig. 3.2) such that the beam passes the movable retroreflector twice. The maximal time delay is then 13.3 ns. The minimal time delay is also increased to 40 fs, but the time resolution is limited by the pulse duration of 2 ps anyway.

The power of each beam is adjusted by gradient filters. The powers of pump 1 and pump 2 are set to match a pulse area of $\Theta = \pi$ by optimizing the signal amplitude. The probe power is about ten times weaker. The power of the RP is set to match $\Theta = 2\pi$ by optimizing the amplitude of an echo (see Sec. 2.3.2).

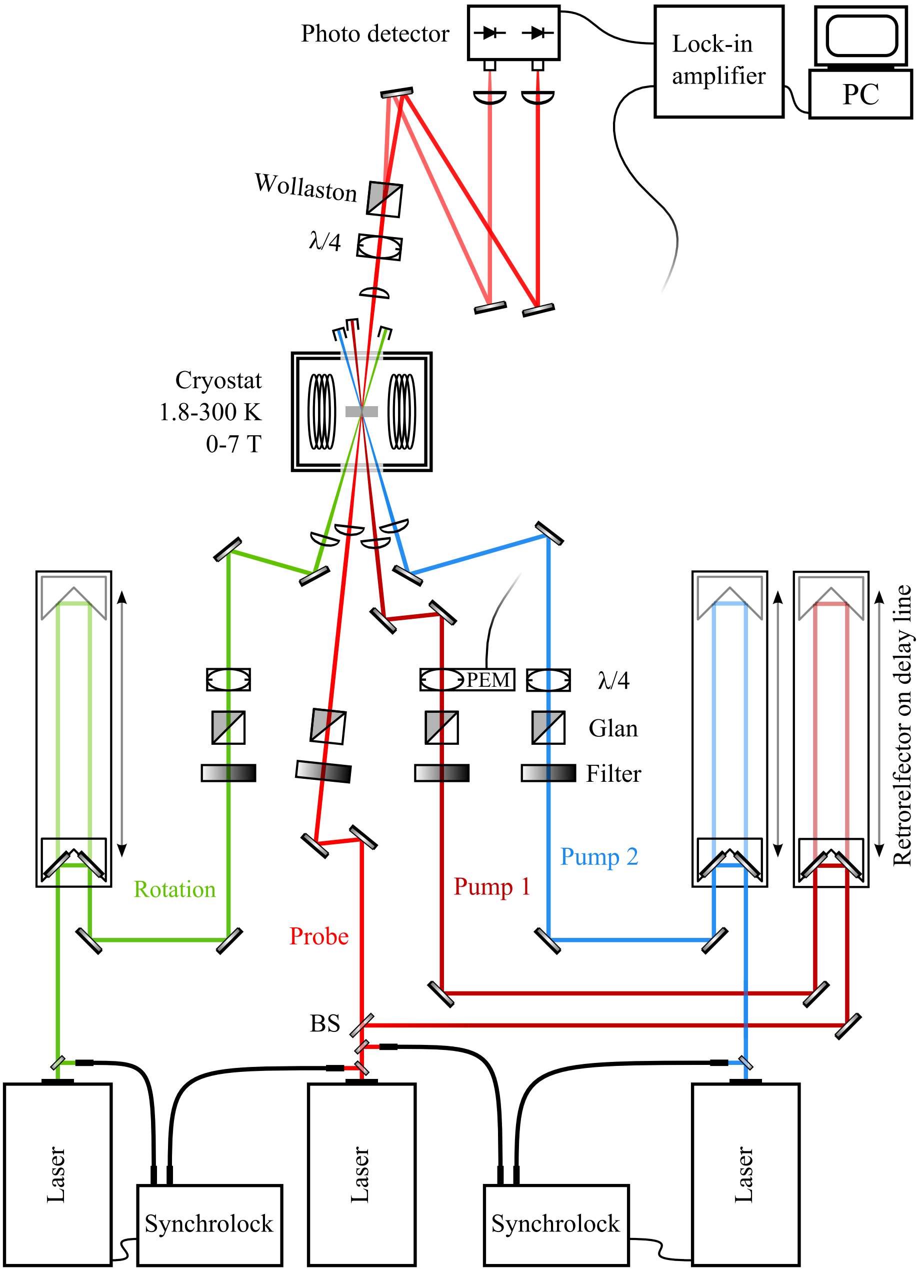

Figure 3.2 Schematic illustration of the pump-probe setup used for the tomography experiments in Chap. 4. It is a degenerate pump-probe setup (red beams, "Pump 1" and "Probe") extended by a second pump beam (blue beam, "Pump 2") to orient a different subensemble of QDs, and a beam that is used to rotate spins (green, "Rotation"). The optical components are abbreviated "BS" (beam splitter), "Glan" (Glan-Taylor prism), "λ/4" (quarter-wave plate), "PEM" (photoelastic modulator), and "Wollaston" (Wollaston prism).

Figure 3.3 Part of the optical setup used for measuring the photoluminescence (PL) and the laser photon energies. Scattered laser light and the PL emission are collected by lenses and guided into a spectrometer with a charge-coupled device (CCD). A video camera allows a look into the cryostat.

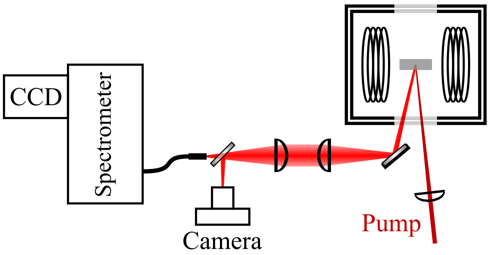

Before the beams are focused on the sample they pass polarization optics, such as a Glan-Taylor prism to ensure a linear polarization. After this prism all beams except the probe get circularly polarized by a quarter-wave plate (QWP). However, in most experiments the QWP of pump 1 is exchanged by a photoelastic modulator (PEM) as shown in Fig. 3.2. The PEM (Hinds Instruments PEM100 II/FS84) periodically switches the polarization of the transmitted beam from left-handed to right-handed circular at a frequency of 84 kHz. This inverts the induced spin polarization and allows the amplification of the measured signal by a lock-in amplifier (Signal Recovery 7265 DSP). The lock-in technique is describe in Sec. 3.2.2. If the polarization of pump 1 shall be fixed (or if another beam shall be modulated), the QWP is not replaced and an optical chopper is implemented in the beam path before the corresponding delay line, where the beam position is most stable. The chopper modulates the beam intensity at a frequency of about 3 kHz.

Plano-convex lenses focus the beams to spots with a diameter of about 100 µm on the sample. The probe spot, which defines the area on the sample and the dots that contribute to the measured signal, is set to be the smallest. This ensures that these dots are addressed by the other spots, if the other spot's position slightly changes induced by the mechanical delay lines. The RP spot in turn is set to be largest, because then, the Gaussian beam's intensity is more homogeneously distributed over the spot area of the smaller pump spots and the rotation parameters (see Sec. 2.3.2) are better fulfilled for all spins of interest. Spot positions and sizes are checked with a video camera directed into the sample chamber as depicted in Fig. 3.3.

The sample is mounted in a magnet cryostat, which allows to apply an external magnetic field of up to $B = 7\,\mathrm{T}$. The field is oriented along x, perpendicular to the optical axis z. The sample inside the variable temperature inset (VTI) of the cryostat is cooled down to $T = 6\,\mathrm{K}$ by evaporating liquid helium. Behind the cryostat all beams except the probe are blocked.

A photoluminescence (PL) spectrum of the sample can be acquired by a spectrometer as drawn in Fig. 3.3. The sample is therefor excited above the band gap by, e. g., the pump beam. The light emission from the sample is collected with lenses and focused on a fiber that guides it to the spectrometer, where the photon energies are spatially separated by a diffraction grating and acquired by a charge-coupled device. The wavelength of scattered laser light can be determined in this way as well.

After the probe beam is transmitted through the sample, changes in its initially linear polarization are measured. For this, a Wollaston prism is used to separate the probe into two beams of orthogonal linear polarization. These two beams are focused onto the diodes of a balanced photo detector (New Focus Nirvana Detector), which measures the difference of both beam intensities. The temporal resolution of the detector is 8 µs. It can resolve the signal modulation, but not the laser pulses. To measure the Faraday rotation, a half-wave plate is installed before the prism. It is adjusted such that the uninfluenced probe-beam polarization is rotated by 45 ° with respect to a crystal axis of the prism. Thus, the beam is divided into two beams of equal intensity and the photo detector output is zero. Any rotation of the polarization plane then results in an imbalance of the intensities and a detector output proportional to the rotation angle θ_{F}.[1]

The ellipticity ε is measured in a similar way, but with a QWP instead of the half-wave plate. It is adjusted such that the uninfluenced linearly polarized probe beam gets circularly polarized after passage. This is the case when the fast axis of the QWP and the polarization plane make an angle of 45 °. It is also important that a crystal axis of the Wollaston prism is parallel to the uninfluenced linear polarization plane of the probe beam. Rotations of the polarization plane then result in elliptically polarized light, but with its major axis parallel to the fast axis of the QWP (45 ° with respect to the crystal axis of the Wollaston prism). Deviations from the linear polarization ($\varepsilon = 0$) before the QWP, however, result in deviations from the circular polarization after the QWP with its major axis parallel to the crystal axis of the prism so that the beam is unequally divided. The output signal of the balanced photo detector is amplified by a lock-in amplifier (see Sec. 3.2.2) and recorded with a computer.

3.2.1 Setup specifics for the experiments on hole spins

For the experiments on hole-spin coherence (Chap. 5), several setup configurations with the components introduced above are used. One configuration not yet discussed is depicted in Fig. 3.4. It is used for the experiments with pump doublets (Sec. 5.1) and is an extension of the basic pump-probe setup by an additional pump. The difference to the second pump in the tomography experiments is that it is split-off from the first pump, recombined with it, and thus modulated by the same PEM. In this way, the second pump changes the repetition pattern of the spin-orienting pulse train instead of orienting different spins as in the tomography experiments. Such a setup was already used by A. Greilich in Ref. [Gre07a]. In this work however, a vector magnet cryostat is used, which allows to apply a magnetic field vector that

---

[1] In fact, it is only proportional to the intensity difference, but for small values of θ_{F} the intensity difference is proportional to that angle. In the experiments of this work the absolute rotation angle, which can be determined, if the absolute intensities are known, is in the order of 10^{-5}rad. See the appendix in Ref. [Gre07a] for more information.

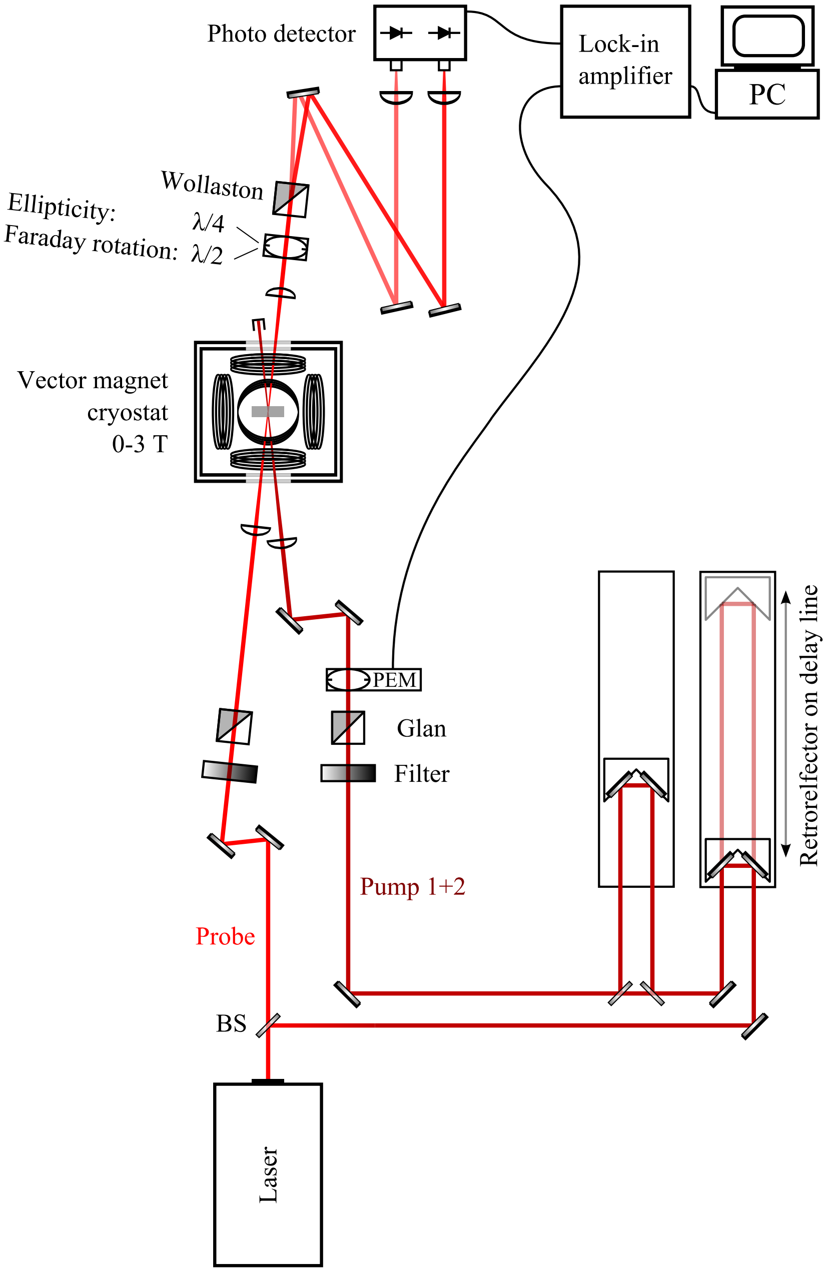

Figure 3.4 Schematic illustration of the setup for excitation with pump doublets. The pump beam is split into two pump-pulse trains pump 1 and pump 2, which are recombined after one of them is detoured by a fixed delay. The optical components are abbreviated "BS" (beam splitter), "Glan" (Glan-Taylor prism), "$\lambda/2$" (half-wave plate), "$\lambda/4$" (quarter-wave plate), "PEM" (photoelastic modulator), and "Wollaston" (Wollaston prism).

can be rotated in all three dimensions with a strength of up to $B = 3\,\mathrm{T}$. It is used for measuring the hole-spin g factor anisotropy by rotating the field vector in the xy plane perpendicular to the optical z axis. Except for the temperature dependent measurements in Sec. 5.2.1 the VTI is set to $T = 6\,\mathrm{K}$.

Furthermore, the repetition pattern of the pump (and probe) is altered in some experiments by implementing a pulse picker right after the laser. The pulse picker (APE pulseSelect) picks every nth pulse and blocks all the others such that the effective pulse repetition period is a multiple of the intrinsic laser repetition period of 13.2 ns. The laser beam is therefor focused on a crystal on a piezo transducer, which temporarily generates an acoustic standing wave inside the crystal, whenever a pulse shall be picked. The acoustic wave serves as a grating by which the beam is diffracted. A spatially adjustable shield blocks the zero-order beam while the first-order diffracted beam can pass. The moment of picking is synchronized with a desired division ratio $1/n$ of the laser repetition rate by means of a fast photo diode placed in a split-off part of the laser beam. The division ratio is varied from $1/n = 1/10$ to $1/35$, reaching effective repetition periods of up to 462 ns.

3.2.2 Lock-in amplification

A lock-in amplifier is generally used to improve the signal-to-noise ratio of periodically modulated signals. At first, the measured signal $V_{\mathrm{In}}(t)$ with periodicity $2\pi/\omega_{\mathrm{Mod}}$ and phase ϕ_{In} is preamplified and prefiltered to get rid of the power line frequency and aliasing. After that, $V_{\mathrm{In}}(t)$ is electronically multiplied with an internal reference signal $V_{\mathrm{Ref}}(t)$ with an adjustable phase ϕ_{Ref} and the same periodicity as $V_{\mathrm{In}}(t)$, provided by the external modulation frequency of the PEM or chopper controller, for instance. The product $V_{\mathrm{In}}(t) \times V_{\mathrm{Ref}}(t)$ is then integrated over several periods by a low-pass filter so that noise and signal contributions which are not periodic with $2\pi/\omega_{\mathrm{Mod}}$ average out. The output of the lock-in amplifier $V_{\mathrm{Out}} \propto V_{\mathrm{In}}^0 \cos(\phi_{\mathrm{Ref}} - \phi_{\mathrm{In}})$ is a DC voltage, which is proportional to the input amplitude V_{In}^0 and maximal for $\phi_{\mathrm{Ref}} = \phi_{\mathrm{In}}$ [Kun86]. In this work, $V_{\mathrm{In}}(t)$ is the voltage provided by the balanced photo detector. One integration period (> 100ms) coincides with the resting time of the delay line so that V_{Out} is one data point of the recorded pump-probe curve.

In a more simplified view, the lock-in amplifier measures the difference of those two values of V_{In}, which appear at the extreme states of one modulation period. In case of intensity modulation with a chopper, V_{Out} is proportional to the difference between V_{In} when the pump beam can pass and V_{In} when the pump is blocked by a chopper blade. The polarization of the pump is constant (σ^+ or σ^-) here. In case of PEM modulation, the polarization of the pump beam is switched periodically between σ^+ and σ^-. V_{Out} is then proportional to the difference between V_{In} during σ^+ pumping and V_{In} during σ^- pumping.

In the experiments of this work the pump beam is modulated while the other beams, including the probe, are not. Thus, only influences on the probe polarization (Faraday rotation and ellipticity) that are caused by the pump-induced spin coherence are measured. Direct influences of spin coherence induced by other beams are not observed. Solely their effects on the pump-induced spin coherence can be detected. This has important consequences for the two ways of modulation: The chopper periodically blocks the pump so that all effects of other beams on the spin coherence induced by the pump are modulated as well and contribute to the output signal. The PEM, instead, periodically switches the polarization of the pump. Hence, effects that do not depend on the pump polarization are not modulated and average out in the lock-in amplification.[2] This can be beneficial to suppress unwanted effects, but it can also be obstructive if these effects shall be studied. Especially in pump-probe experiments with several (non-modulated) beams, whose effects depend on their polarization relative to the (modulated) pump, as described in Sec. 4.2, these considerations can play an important role.

3.3 Samples

Two (In,Ga)As/GaAs QD samples are studied in this work. They were both grown at the Ruhr University Bochum[3] by molecular beam epitaxy (see Sec. 2.1.2). The substrate is (001)-oriented GaAs, on which several QD layers, each with a dot density of $10^{10}\,\mathrm{cm}^{-2}$ were grown.

The sample used for the electron-spin tomography (Chap. 4) is labeled # 11955. It contains 20 QD layers separated by 80-nm wide GaAs barriers. A Si-δ-doping sheet beneath each layer provides in average one resident electron per dot. However, previous studies indicate that only 50 % of the dots are singly charged while the others are neutral or doubly charged [Spa11c]. The detailed growth sheet is given in Table. 3.1. After annealing at 945 °C the ground state emission of the PL spectrum is at 1.393 eV with a full width at half maximum (FWHM) of 13 meV, measured at $T = 6\,\mathrm{K}$ (see Fig. 3.5).

Sample # 11376 used for the studies on hole-spin coherence (Chap. 5) contains 10 layers of QDs separated by 100-nm GaAs barriers. Although nominally undoped, positively and negatively charged QDs are found in the experiments. The majority is p-doped due to carbon impurities. The PL ground state emission at $T = 6\,\mathrm{K}$ has a maximum at 1.381 eV and a FWHM of 19 meV after annealing at 960 °C (see Fig. 3.6). The growth sheet is given in Table 3.2.

---

[2] The word “effect” refers to changes in the signal amplitude V_{In} at one specific pump-probe delay.

[3] Prof. Dr. A. D. Wieck and Dr. D. Reuter, chair for applied solid state physics.

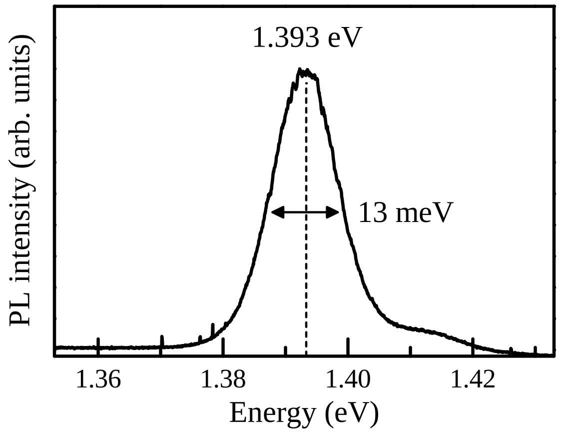

Figure 3.5 Ground state photoluminescence spectrum of the n-doped QD ensemble (sample # 11955) annealed at 945 °C, measured at $T = 6\,\text{K}$.

Table 3.1 Growth sheet of sample # 11955. Layer material, duration t, temperature T, thickness d, and number of loops are listed in growth order from top to bottom.

Layer	t (s)	T (°C)	d (nm)	Loops	
GaAs	531.9	660	100.0	1x	
AlAs	20.0	660	2.0	20x	
GaAs	5.3	660	1.0		
AlAs	20.0	660	2.0	1x	
GaAs	425.5	660	80.0	1x	
InAs	4.0	590	0.3	16x	20x
GaAs	42.6	580	8.0		
GaAs	42.6	660	8.0		
Si-Delta	4.0	660	0.0		
GaAs	340.4	660	64.0		
AlAs	20.0	660	2.0	20x	
GaAs	5.3	660	1.0		
GaAs	531.9	660	100.0	1x	
GaAs:Si	79.8	660	15.0	1x	

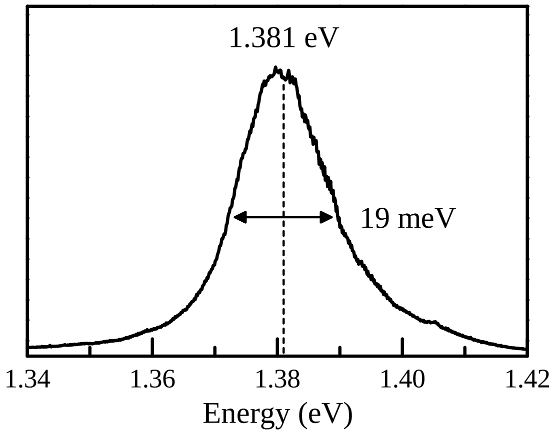

Figure 3.6 Ground state photoluminescence spectrum of the undoped QD ensemble (sample # 11376) annealed at 960 °C, measured at $T = 6\,\mathrm{K}$.

Table 3.2 Growth sheet of sample # 11376. Layer material, duration t, temperature T, thickness d, and number of loops are listed in growth order from top to bottom.

Layer	t (s)	T (°C)	d (nm)	Loops	
GaAs	515.5	635	100.0	1x	
AlAs	9.7	635	1.0	20x	
GaAs	5.2	635	1.0		
AlAs	9.7	635	1.0	1x	
GaAs	20.6	635	4.0	1x	
GaAs	515.5	635	100.0	1x	
InAs	4.0	555	0.45 ML	16x	20x
GaAs	41.2	545	8.0		
GaAs	474.2	635	92.0		
AlAs	9.7	635	1.0	20x	
GaAs	5.2	635	1.0		
GaAs	51.5	635	10.0	1x	

4 Optical electron-spin tomography

For quantum information processing it is necessary to have precise information about the state of the qubit system. In general, a series of measurements reconstructing the complete state of a quantum mechanical object is called *quantum state tomography* [Alt04]. Regarding spins as a qubit candidate, such tomography experiments have already been performed on nuclear spins [Van05], electron spins of diamond defects [Dol13], and spins in electrically controlled QDs [Fol09, Shu12, Med13] using microwave techniques. While the microwave approach has the advantage of precisely controllable pulse parameters such as pulse area, phase, and polarization, the approach is limited in the time domain: microwave pulses in the frequency range of megahertz are longer than nanoseconds so that they cannot be used for tomography measurements on spin dynamics that occur on a shorter timescale.

Optical pump-probe experiments using picosecond laser pulses allow the study of QD carrier spin dynamics in external magnetic fields in the order of a tesla. Here, the spin precession and dephasing occurs on a timescale below one nanosecond. However, up to now only the spin components along the optical axis and, by interpolating the precession, the orthogonal axis within the precession plane can be monitored. The spin component along the magnetic field axis could not be measured yet.

Gaining access to the x component of the spin vector is of particular interest concerning the spin-spin interactions in a QD ensemble (see Sec. 2.4 and Ref. [Spa11c]). Due to this interaction, a nonzero x component emerges, which can be detected by the tomography measurements presented in this chapter.

The idea is to apply a short optical rotation pulse (RP) to rotate the spin vector, which represents one of the two interacting spin subsets, in such a way that the component in the precession plane becomes oriented along the x axis, while the former x component precesses in the yz plane after rotation. This sequence is schematically shown in Fig. 4.1. The spin vector with nonvanishing x component precesses about a magnetic field along the x axis. When the y component is in the maximum during a precessional cycle, a RP much shorter than the precession period rotates the spin vector almost instantaneously by $\pi/2$ about the optical axis (z axis). Thus, the initially precessing component is rotated into the x axis, where it does not precess and therefore does not contribute to the measured spin polarization. The former x component, instead, is rotated into the $-y$ direction, from where it starts

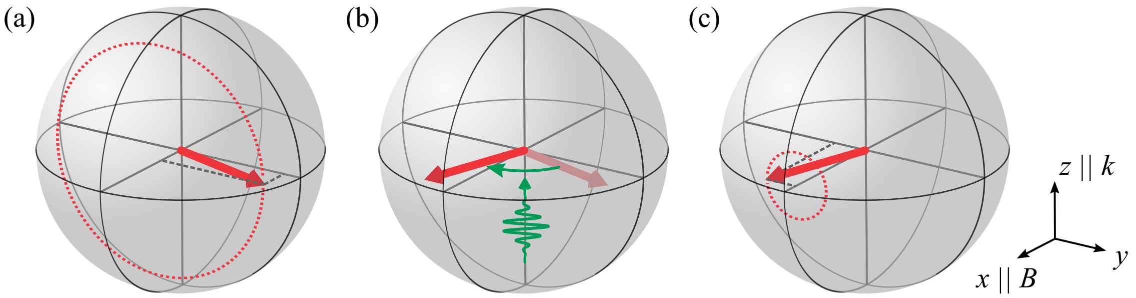

Figure 4.1 Scheme of the optical spin tomography to measure the spin component along the magnetic field axis x. **(a)** The ensemble spin vector precesses about the magnetic field (x axis). **(b)** When the y component is in the maximum during a precessional cycle, an optical pulse rotates the spin vector quasi-instantaneously by $\pi/2$ about the z axis. **(c)** The spin component initially along the x axis becomes oriented perpendicular to the magnetic field so that it starts to precess in the yz plane and can be monitored.

to precess in the yz plane and can be monitored.

To learn more about the optical spin rotation, which is a key requirement for the optical spin tomography in this work, a preliminary experiment regarding the spin rotation in dependence on the magnetic field was carried out and is presented in Sec. 4.1. In Sec. 4.2 the results of the spin-tomography experiment and theoretical calculations modeling the tomography in presence of the spin-spin interaction are presented. In an additional Experiment in Sec. 4.3, an adjusted excitation-pulse protocol is used to reveal the relative orientations of mode-locked electron spins within an ensemble.

4.1 Spin rotations at different magnetic fields

Finding the parameters, for which a precise spin rotation by a desired angle is achieved, is crucial for the optical electron-spin tomography. Experimental studies on the pulse area and the detuning between the rotation pulse and the trion transition energy of the pumped spins were performed in Ref. [Gre09a]. One of the parameters that has not been investigated yet is the external magnetic field, which determines the timescale of the spin dynamics. In this section, studies on the rotation angle depending on the RP detuning at different magnetic fields are presented.

The studies are carried out on the sample # 11955 described in Sec. 3.3. It contains an ensemble of n-doped (In,Ga)As/GaAs QDs. The spin dynamics of the resident electrons are addressed by a degenerate pump-probe setup extended by a synchronized laser providing a train of rotation pulses (RP) tunable in energy (see Sec. 3.2). The pump and probe photon energy E_{Pu} is in resonance with the trion transitions in the PL maximum. The spin evolution is monitored by measuring the ellipticity of the probe beam after transmission through the sample. A PEM is used to modulate the circular polarization of the pump beam between σ^+ and σ^-. The delay τ between pump and RP incidence is chosen such that the rotation is performed when the spin polarization induced by the pump is oriented along the y axis and its z component is zero. To find the RP pulse area of $\Theta_{\mathrm{RP}} = 2\pi$ the RP photon energy E_{RP} is tuned to be in resonance with the pump-probe photon energy ($\Delta = E_{\mathrm{Pu}} - E_{\mathrm{RP}} = 0$). Then, the power is adjusted until the amplitude of the emerging echo at 2τ is maximal. Under these conditions a rotation by an angle of $\Phi = \pi$ is performed (see Sec. 2.3.2). In order to reduce this rotation angle, the RP photon energy is detuned to lower values so that the detuning Δ is increased incrementally. This was done for several magnetic fields B between 0.3 and 1.0 T at a temperature of $T = 6\,\mathrm{K}$.

The results for $B = 0.3\,\mathrm{T}$, $B = 0.5\,\mathrm{T}$, $B = 0.8\,\mathrm{T}$, and $B = 1.0\,\mathrm{T}$ are exemplarily shown in Fig. 4.2. The RP incidence is denoted by the vertical dashed line at delay τ. The detuning between the pump-probe and RP photon energies is varied incrementally from $\Delta = 0$ to $\Delta = 1.93\,\mathrm{meV}$. As a reference, the lowest trace in each panel shows a measurement without RP applied. The second dashed line at 2τ marks the delay at which a spin echo occurs for rotations by an angle of $\Phi = \pi$ corresponding to $\Delta = 0$. By increasing the detuning $\Delta > 0$ the signal amplitude at 2τ $A_{2\tau}$ gets smaller until it is close to zero indicating a rotation angle of $\Phi = \pi/2$. In this case, the spin vector is rotated into the x axis, where it does not precess. This can be observed for magnetic fields $B \leq 0.5\,\mathrm{T}$ as shown in the panels (a) and (b) of Fig. 4.2. At $B = 0.3\,\mathrm{T}$, the smallest signal amplitude around 2τ $A_{2\tau}^{\mathrm{min}}$ is found for $\Delta = 0.77\,\mathrm{meV}$; at $B = 0.5\,\mathrm{T}$ it is 0.58 meV. For larger detunings the signal amplitude around 2τ increases again. The phase is shifted by π, indicating that the rotation angle is reduced below $\pi/2$. For the largest measured detunings the signals with and without RP applied are nearly identical as the spins are barely rotated.

The rotation angle can be extracted from the data by comparing the amplitudes before and after the rotation. Without other influences on the signal amplitude and neglecting ensemble dephasing the rotation angle would be $\Phi = \arccos(A_{2\tau}/A_\tau)$, with A_τ being the signal amplitude just before rotation. It is obtained from the data by a sinusoidal fit of one precession period. $A_{2\tau}$ is obtained in the same way for one precession period at 2τ. The sign of $A_{2\tau}$ is defined positive for signal oscillations in phase with the reference curve (without RP applied). Hence, it is negative for signals in antiphase ($\Delta = 0$, e. g.). The relation between these amplitudes and Φ is illustrated for a single spin in the inset in Fig. 4.3(a). However, in the experiment some spin-coherence signal is lost after the RP action as can be seen from the fact that the maximal echo amplitude for $\Delta = 0$ does not reach the value of the signal amplitude before rotation. Therefore, the amplitudes $A_{2\tau}^{\Delta}$ at 2τ for a detuning Δ are corrected by the absolute factor $|A_\tau^0/A_{2\tau}^0|$ assuming that the rotation angle for zero detuning is $\Phi(0) = \pi$. In addition, a factor A_τ^0/A_τ^Δ is implemented to account

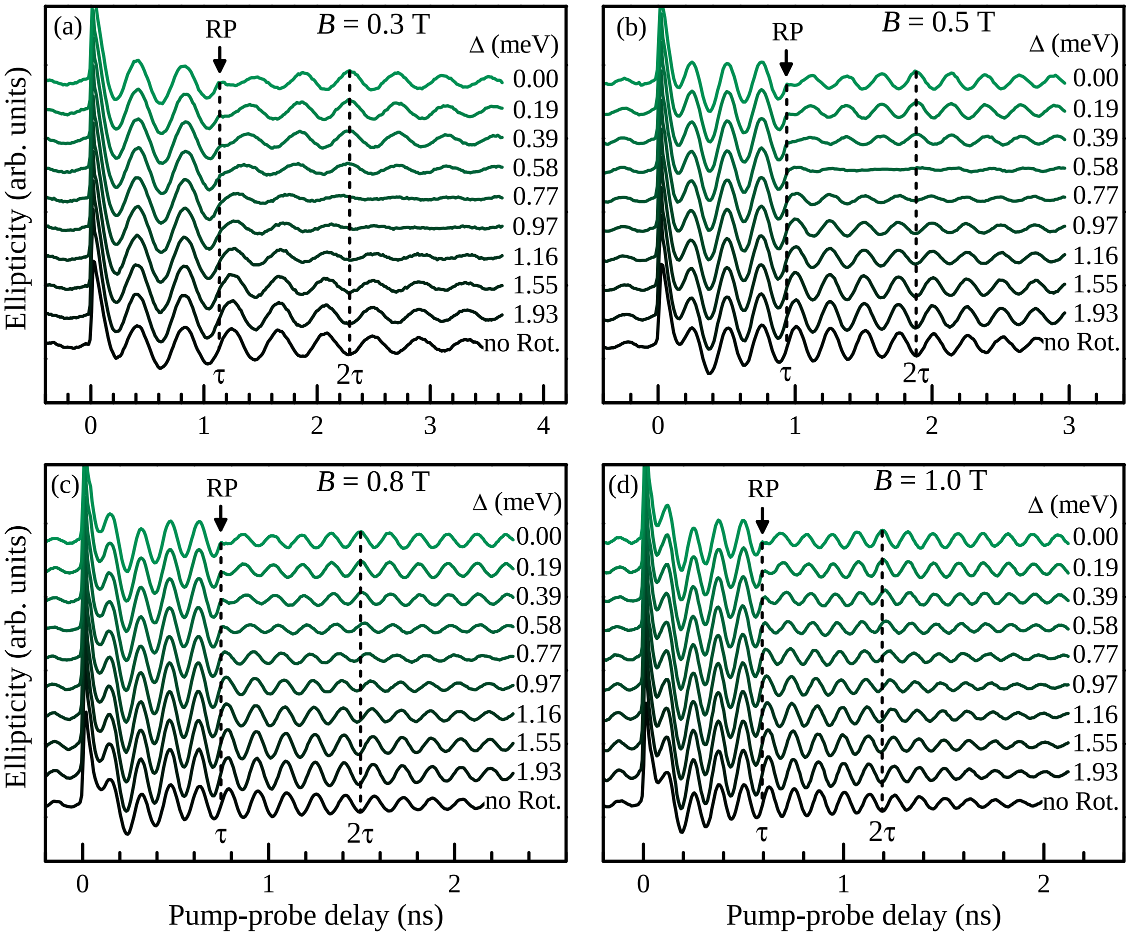

Figure 4.2 Time-resolved pump-probe ellipticity measurements with additional rotation pulses (RP) applied at a delay τ for different magnetic fields of $B = 0.3\,\mathrm{T}$ **(a)**, $B = 0.5\,\mathrm{T}$ **(b)**, $B = 0.8\,\mathrm{T}$ **(c)**, and $B = 1.0\,\mathrm{T}$ **(d)**. $T = 6\,\mathrm{K}$ in each panel. τ is chosen such that the rotation occurs when the z component of the ensemble spin vector is zero. The detuning $\Delta = E_{\mathrm{Pu}} - E_{\mathrm{RP}}$ between the pump-probe and RP photon energies is varied incrementally from 0 to 1.93 meV. As a reference the lowest trace in each panel shows a measurement without RP applied. All other traces are shifted vertically for reasons of clarity.

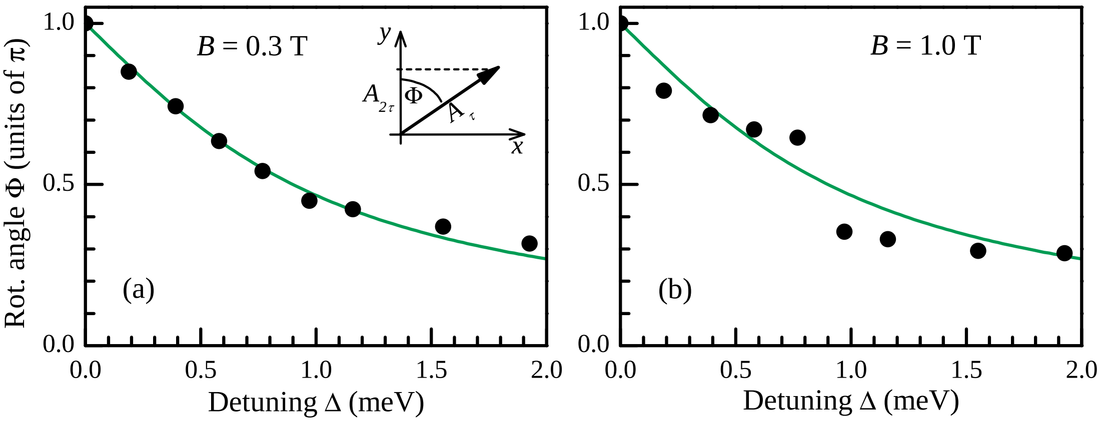

Figure 4.3 **(a)** Rotation angle Φ in dependence of the detuning Δ at $B = 0.3\,\mathrm{T}$. The green line is calculated according to Eq. (2.35) for a pulsewidth of $\sigma = 1\,\mathrm{meV}$. The inset shows the relation between the rotation angle Φ and the spin vector component in the precession plane (represented by its y component) before (A_τ) and after ($A_{2\tau}$) rotation about the optical z axis. **(b)** Rotation angle dependence at $B = 1.0\,\mathrm{T}$. The data points calculated with Eq. (4.1) show a discontinuity around the detuning which corresponds to a $\pi/2$ rotation, because the model assumes a phase of either 0 or π with respect to the reference trace, which is not fulfilled for $B > 0.5\,\mathrm{T}$. The green line is again a calculation according to Eq. (2.35) with $\sigma = 1\,\mathrm{meV}$.

for fluctuations in the total signal strength. The rotation angle is then

$$\Phi(\Delta) = \arccos\left(\frac{A^\Delta_{2\tau}}{A^\Delta_\tau} \left| \frac{A^0_\tau}{A^0_{2\tau}} \right| \frac{A^0_\tau}{A^\Delta_\tau} \right) \; . \tag{4.1}$$

These angles are plotted in Fig. 4.3(a) in dependence of the detuning Δ for the series at $B = 0.3\,\mathrm{T}$. The green line shows the calculated dependence according to Eq. (2.35) with a spectral pulsewidth of $\sigma = 1\,\mathrm{meV}$. The model is in good accordance with the measured data points. For $B = 0.5\,\mathrm{T}$ the detuning dependence of the rotation angle shows a similar behavior except that the $\pi/2$ rotation and all the other angles are achieved for slightly smaller detunings compared to the case of $B = 0.3\,\mathrm{T}$. This deviation is probably due to an inaccurate RP laser detuning or rather an unnoticed detuning of the pump energy, which determines $\Delta = E_{\mathrm{Pu}} - E_{\mathrm{RP}}$.

For $B > 0.5\,\mathrm{T}$ (see panels (c) and (d) of Fig. 4.2) the evolution of the signal around 2τ is different than for $B \leq 0.5$. Although the amplitude $A_{2\tau}$ is in a minimum for a detuning of $\sim 0.77\,\mathrm{meV}$, it does not drop to zero and the phase is not flipped here. It is rather shifted continuously over a range of about $0.5\,\mathrm{meV}$. For $B = 1.0\,\mathrm{T}$ the phase shift at the minimum amplitude $A^{\mathrm{min}}_{2\tau} = A^{0.77}_{2\tau}$ is $\pi/2$. The amplitude $A^{\mathrm{min}}_{2\tau}$ is still about two thirds of the amplitude $A^0_{2\tau}$. Most probably, ensemble inhomogeneities, which are more pronounced at higher fields, prevent a clean spin rotation and account for the nonvanishing amplitude. The phase shift can be

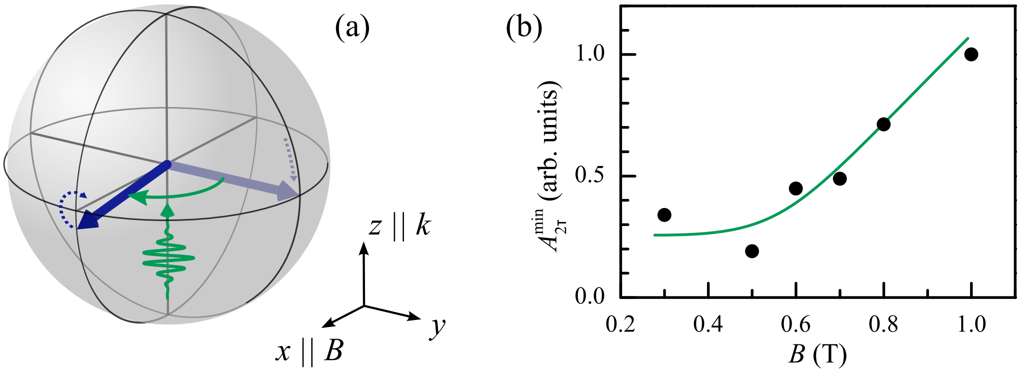

Figure 4.4 **(a)** Schematic illustration of a spin rotation by an angle of $\Phi = \pi/2$ about the optical axis z when the initial spin orientation is along y. The precession about the field axis x during the RP action leads to a finite z component of the central spin after rotation which can subsequently precess. **(b)** Minimum amplitude $A_{2\tau}^{\min}$ at delay 2τ for the detuning at which the rotation by $\Phi = \pi/2$ is expected in dependence of the magnetic field B. The green line is a guide to the eye.

explained when the faster spin precession compared to the finite duration of the RP action at higher magnetic fields is considered. Precessions about the field axis x during the RP action lead to a spin component along z after rotation. This component can subsequently precess even in the case of a nominal $\pi/2$ rotation where the y component is zero after RP action. The phase of the remaining precession depends on the rotation angle or rather the remaining y component and is $\pi/2$ with respect to the reference trace in the case of a $\pi/2$ rotation [see Fig. 4.4(a)]. For higher magnetic fields this effect is stronger as the precession frequency is larger. Although carefully adjusted in the experiment, an imperfect timing of the RP incidence (so that $S_z \neq 0$ at this moment) is more probable at higher fields and would also explain both the nonvanishing amplitude and the continuous phase shift.

Consequently, the rotation angles for $B > 0.5\,\mathrm{T}$, calculated with Eq. (4.1), show a discontinuity at that particular detuning which corresponds to a $\pi/2$ rotation. This is shown for $B = 1.0\,\mathrm{T}$ in Fig. 4.3(b). The reason for the discontinuity is that the model does not account for a continuous phase shift at 2τ, but only for a phase flip of π which results in a sign change in $A_{2\tau}$. Neglecting the detuning range around this discontinuity, the outer data points resemble the calculated detuning dependence according to Eq. (2.35) depicted by the green line. For $B = 0.6$, 0.7, and $0.8\,\mathrm{T}$ the detuning dependences of the rotation angle are similar to the case of $B = 1.0\,\mathrm{T}$. The minimum amplitude is $A_{2\tau}^{\min} = 0.77\,\mathrm{meV}$ for all fields $B > 0.5\,\mathrm{T}$. Thus, the detuning dependence of the rotation angle does in principle not vary for different magnetic fields in the studied range of 0.3 to 1.0 T.

However, the value of $A_{2\tau}^{\min}$ of the spin-ensemble polarization increases with the magnetic field for fields $B > 0.5\,\mathrm{T}$ as shown in Fig. 4.4(b). This is obstructive for

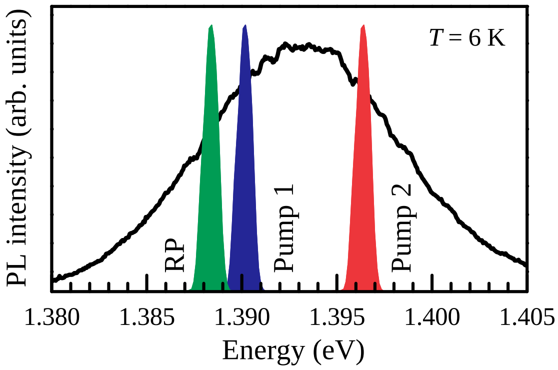

Figure 4.5 Spectral positions of the laser lines with respect to the photoluminescence spectrum of the n-doped QD ensemble (sample # 11955) measured at $T = 6\,\mathrm{K}$ (black trace). The colored lines show the laser spectra, each with a FWHM of 1 meV. The photon energies are 1.388 eV (RP), 1.390 eV (pump 1), and 1.396 eV (pump 2).

the tomography experiment as the amplitudes of the precession signal after rotation are expected to provide the values of the x component. Therefore, the tomography experiments need to be carried out at magnetic fields $B \leq 0.5\,\mathrm{T}$.

4.2 Tomography of electron-spin ensemble

In this section the experimental results of an electron-spin tomography measurement are presented and compared with a theoretical model. The experiment demonstrates the key ingredients of an all-optical technique based on picosecond laser pulses to map all three components of a spin vector. These results have also been published in Ref. [Var14b].

The tomography technique is applied to a subset of spins, which is interacting with another subset of spins within the same QD ensemble in the way that is described in Sec. 2.4. In Ref. [Spa11c] this Heisenberg-like interaction between two electron-spin ensembles was studied in detail at a magnetic field of $B = 1\,\mathrm{T}$. The buildup of an x component of the spin vector representing one spin subset was predicted by theory but not yet measured. Due to the findings in the previous Sec. 4.1, the external magnetic field is reduced to $B = 0.3\,\mathrm{T}$ in the tomography experiments described in the following.

The two spin subsets are addressed by two pump-pulse trains called pump 1 and pump 2. Their photon energies are shown in Fig. 4.5 together with the PL spectrum of the QD sample. The photon energy of pump 1 is $E_{\mathrm{Pu1}} = 1.390\,\mathrm{eV}$; 3 meV below the maximum of the PL spectrum, whose FWHM is about 13 meV. The photon energy of pump 2 is $E_{\mathrm{Pu2}} = 1.396\,\mathrm{eV}$; 3 meV above the PL maximum. At a pulsewidth of 1 meV the detuning of 6 meV between pump 1 and pump 2 ensures that two separate QD subsets (subset 1 and subset 2, respectively) are addressed. The pulse areas of pump 1 and pump 2 are set to be $\Theta_{\mathrm{Pu1}} = \Theta_{\mathrm{Pu2}} = \pi$.

The initial relative orientation between the two spin vectors representing subset 1 and subset 2 was chosen to be antiparallel since in this case the coupling was found to be maximal [Spa11c]. As it is shown in Fig. 4.6(a), pump 2 pulses hit the

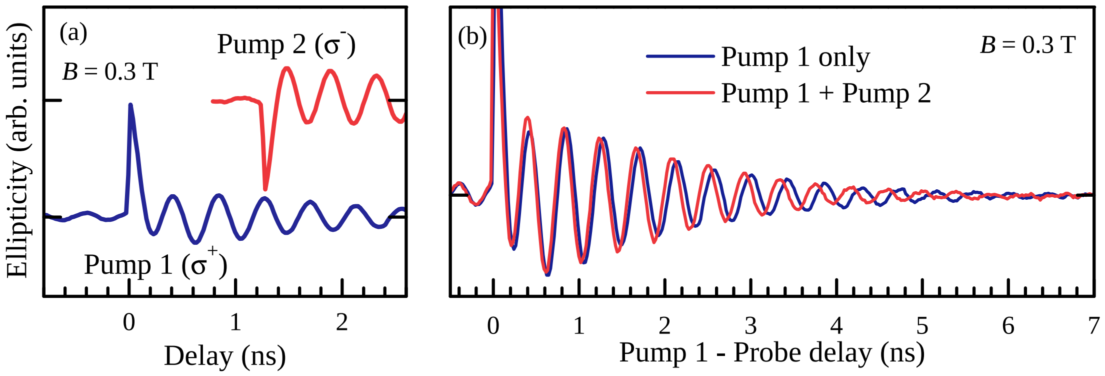

Figure 4.6 **(a)** Time-resolved ellipticity measurements of spin subset 1 addressed by pump 1 (σ^+ polarized, blue) and of spin subset 2 addressed by pump 2 (σ^- polarized, red). In both cases the probe was degenerate with the corresponding pump and the other pump was not applied. **(b)** Ellipticity measurement of the spins probed in resonance with the QD subset excited by pump 1 (subset 1) without pump 2 (blue) and with pump 2 additionally applied (red). When interacting with the second subset a phase shift in the spin precession of up to π (at ~5 ns) builds up relative to the case without pump 2.

sample 1.3 ns after pump 1 pulses in a maximum of the subsequent spin precession of subset 1. The lower (blue) trace in the graph shows a pump 1-probe ellipticity measurement without pump 2 applied. The upper (red) trace, instead, shows a pump 2-probe measurement without pump 1 applied. In both cases, the probe was degenerate with the corresponding pump, which was intensity modulated by a chopper. The polarization of pump 1 was right-handed circular (σ^+), while it was left-handed circular (σ^-) for pump 2. Therefore, the spins in subset 2 were oriented antiparallel to the spins in subset 1 as one can see from the sign inversion of the ellipticity signal in Fig. 4.6(a).

The interaction between subset 1 and subset 2 as an effect of the antiparallel spin alignment can be seen in Fig. 4.6(b). The phase of the oscillating ellipticity signal of subset 1 is shifted, when pump 2 is applied in the way described above. The blue trace shows the spin precession of subset 1 when only pump 1 is applied. The red curve also shows the ellipticity signal of subset 1 (the probe is degenerate with pump 1 in both cases), but with pump 2 applied orienting subset 2 at a delay of 1.3 ns. The phase shift increases continuously reaching π 5 ns after pump 2 incidence. Note that the ellipticity contribution induced by subset 2 is negligibly small for the pump 2-probe detuning of 6 meV (see Sec. 2.5 and Ref. [Gla10]). In addition, only pump 1 is intensity modulated by a chopper.

To also monitor the x component of subset 1, which is expected to arise from the interaction with subset 2, the RP pulse train is implemented in the setup so that it reaches its final extension illustrated in Fig. 3.2. The RP pulse area is set to be $\Theta_{\mathrm{RP}} = 2\pi$ as described in Sec. 4.1. To obtain a rotation angle of $\Phi = \pi/2$ the RP photon energy E_{RP} is detuned from E_{Pu1} to lower values. The direction to lower values is advantageous here, since it avoids rotation effects on the spins of subset 2. The detuning at which the $\pi/2$ rotation is reached was $\Delta = E_{\mathrm{Pu1}} - E_{\mathrm{RP}} \approx 2\,\mathrm{meV}$ so that $E_{\mathrm{RP}} = 1.388\,\mathrm{eV}$ (see Fig. 4.5).

Such $\pi/2$ rotations are applied to rotate the component precessing in the yz plane into the x direction so that it does not contribute to the signal anymore. The former x component instead is rotated into the precession plane to be monitored. This is summarized once more in the Bloch sphere representations in Fig. 4.7 for the case without interaction with a second spin subset [panel (a)] and with the interaction with subset 2 [panel (b)] potentially leading to a spin component along the magnetic field. Panel (c) of Fig. 4.7 shows the result of ellipticity measurements, in which rotation pulses were applied under these two conditions. In these experiments pump 1 is polarization modulated between σ^+ and σ^-. This cancels out all potential direct influences of the RP on the ellipticity signal such as the generation of new spin coherence (see Sec. 3.2.2 and Ref. [Gre09a]). The phase shift due to the spin-spin interaction, which is shown in Fig. 4.6(b), is also not measurable anymore. However, the amplitude and the sign of the x component along the magnetic field are not altered and can be measured reliably. The moment of RP incidence in Fig. 4.7(c) is 6.2 ns after pump 1 incidence, when the spin signals in the precession plane have completely dephased. The x component along the magnetic field does not suffer from precession inhomogeneities, so it does not decay. Therefore, if present, the x component should stand out in a particularly clean and prominent way after application of the RP at these long delay times.

The result of the pump 2 application on the ellipticity signal after RP incidence is obvious in Fig. 4.7(c): while there is no change in the measured signal without pump 2, the $\pi/2$ rotation induced by RP leads to a strong signal oscillation when pump 2 is applied. The oscillation cannot be an echo of the pump 1-induced spin coherence, since in this case the signal would increase with a rise time equal to the dephasing time leading to a signal maximum at ~12 ns. Furthermore, such an echo resulting from an imperfect $\pi/2$ rotation would also appear, when no pump 2 is applied. Hence, the signal oscillation must result from an x component of spin subset 1 induced by the spin-spin interaction with subset 2.

In order to obtain the time evolution of the x component, the moment of RP incidence was varied from about 2 ns to 8 ns delay with respect to pump 1 incidence at zero delay. The resulting ellipticity measurements are shown in Fig. 4.8(a). Longer delays could not be achieved due to limitations in the experimental setup, namely the length of the delay stages. The RP delays were set to coincide with the rising flank of the ellipticity signal, when the ellipticity is zero and the spin vector of subset 1 is pointing along y (marked by the green arrows). For all RP delays > 4 ns, when the spin signal has dephased, notable signal oscillations appear when, and only when, pump 2 is applied. For RP delays < 4 ns, when the signal dephasing has not yet occurred, the situation is more complex. The ellipticity signal without

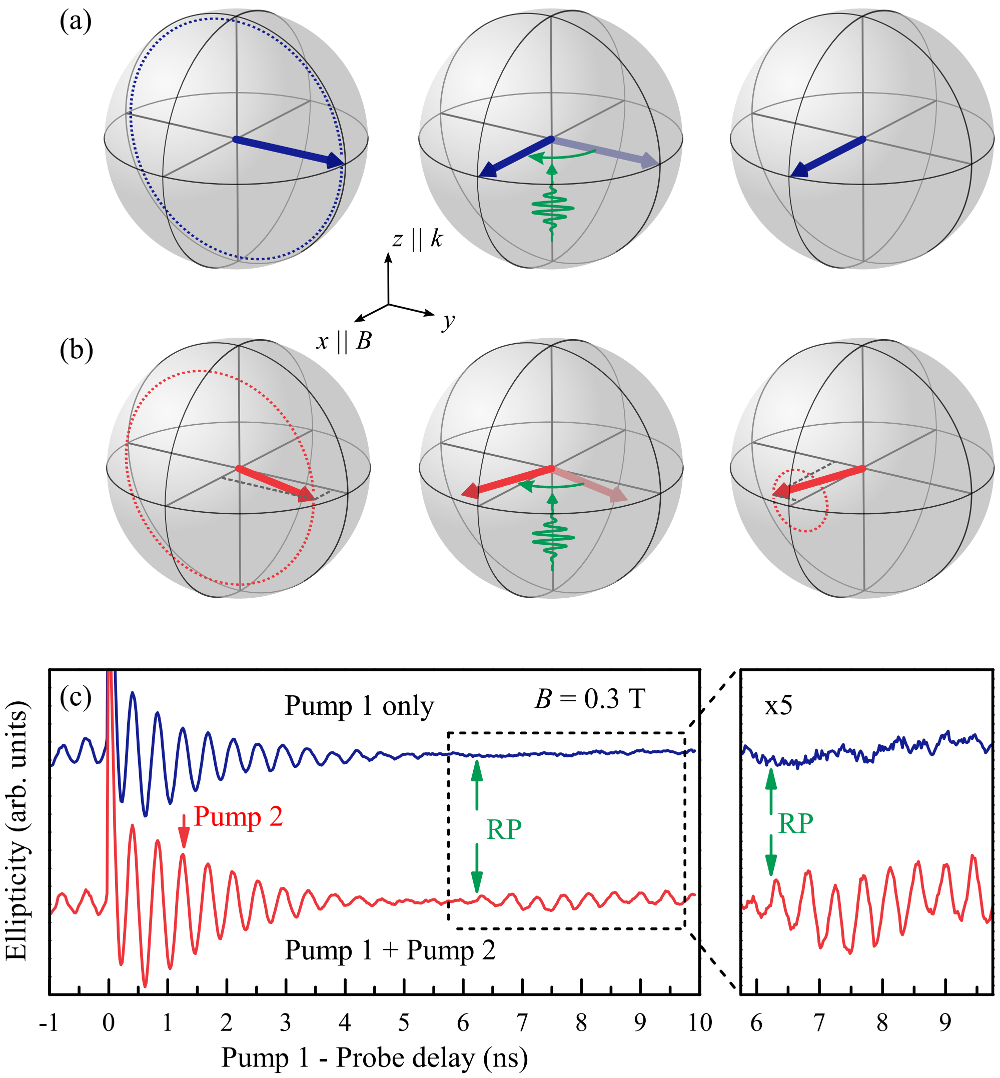

Figure 4.7 **(a)** Scheme of spin tomography without pump 2: the spin vector of the ensemble addressed by pump 1 (represented by the blue arrow), initially oriented along the z direction, precesses in the yz plane about the magnetic field along x. When the vector is pointing along the y axis the RP rotates it quasi-instantaneously by $\pi/2$ about the optical z axis. Now pointing along the x axis it no longer precesses so that there is no spin component along the probe-sensitive z axis. **(b)** With pump 2: the interaction of the two spin ensembles excited by the two pumps potentially leads to the emergence of a spin component along the magnetic field. If the RP is applied when the spin-vector component in the precession plane points along y, the emerged x component becomes oriented perpendicular to $\boldsymbol{B}$ so that it can be measured from its subsequent precessional motion. **(c)** Ellipticity traces without (top), and with pump 2 applied (bottom). The RP incidence is in both cases 6.2 ns after pump 1. In the lower trace an oscillation emerges after the $\pi/2$ rotation, indicating an x component of the spin vector. The graph on the right shows an excerpt of time delays after RP incidence, zoomed by a factor of 5.

pump 2 does not drop to zero after RP incidence, as it is expected for a $\pi/2$ rotation. However, the signal without pump 2 gets weaker promptly after the rotation while such a behavior is not as apparent in the signal with pump 2 [see the red and blue traces after RP incidence in the two lowest curves in Fig. 4.8(a)]. Furthermore, the signals without pump 2 show echolike features as they increase after RP incidence to a maximum at a delay two times larger than the RP delay. This shows that under these conditions the targeted $\pi/2$ rotation does not work perfectly, due to variations of the dipole matrix elements in the ensemble, especially at the flank of the PL spectrum (see Fig. 4.5). In combination with a variation of the energy detuning of the RP laser, this leads to a spread of rotation angles, and the spins rotated by angles $\Phi > \pi/2$ induce an echo signal.

However, the signal without pump 2 serves as a reference by which the data recorded with pump 2 can be corrected. The differences in amplitude with and without pump 2 after RP incidence, normalized with respect to the amplitudes before RP incidence, provide the x component of spin subset 1:

$$S_{1,x} = \frac{A_1}{A_2} B_2 - B_1 \ . \tag{4.2}$$

Here, A_i are the amplitudes right after pump 2 and B_i are those $\sim 1.5\,\text{ns}$ after RP incidence. The indices $i = 1, 2$ refer to the blue and the red traces, without and with pump 2 applied, respectively. The traces are normalized to avoid any artificial differences due to different efficiencies of spin orientation in the measurements. In this way, $S_{1,x}$ was determined for the different applied RP delays. These data are shown in Figure 4.8(b). With increasing delay after pump 2, $S_{1,x}$ increases during about 3 ns and then tends to saturate, at least until 9 ns RP delay.

This behavior is expected from the model calculations by S. E. Economou, which are based on the formalism presented in Ref. [Bar11]. Here, two single spins are considered interacting with a Heisenberg-like form $H_{SS} = J\boldsymbol{S}_1 \cdot \boldsymbol{S}_2$ (see Sec. 2.4). The steady state of one regarded spin is extracted from the steady state of the two-spin system modeled by a 15-dimensional spin vector. A nonunitary map is used to describe the action of the pulses ($\Theta = \pi$ for each of the pump pulses and a perfect $\pi/2$ rotation for RP) and spontaneous photon emission. The representation of a spin subset by a single spin vector is a valid description of the experimental conditions, since the spins in each excited QD subset are mostly mode-locked to a single precession frequency at the external magnetic field of $B = 0.3\,\text{T}$ [Gre09b].

Figure 4.9 shows the calculated time evolution of one spin vector with and without interaction with another one. According to the model, the x component of an interacting spin increases, saturates, and decreases again on a timescale of nanoseconds [Spa11c], much larger than the Larmor precession of the spin. The time evolution of $S_{1,x}$ can be seen from the black dashed line in Fig. 4.9 before RP arrival. After RP incidence the former x component is rotated in the precession plane so that $S_{1,z}$ promptly increases, depending on the value of $S_{1,x}$ at this time, and os-

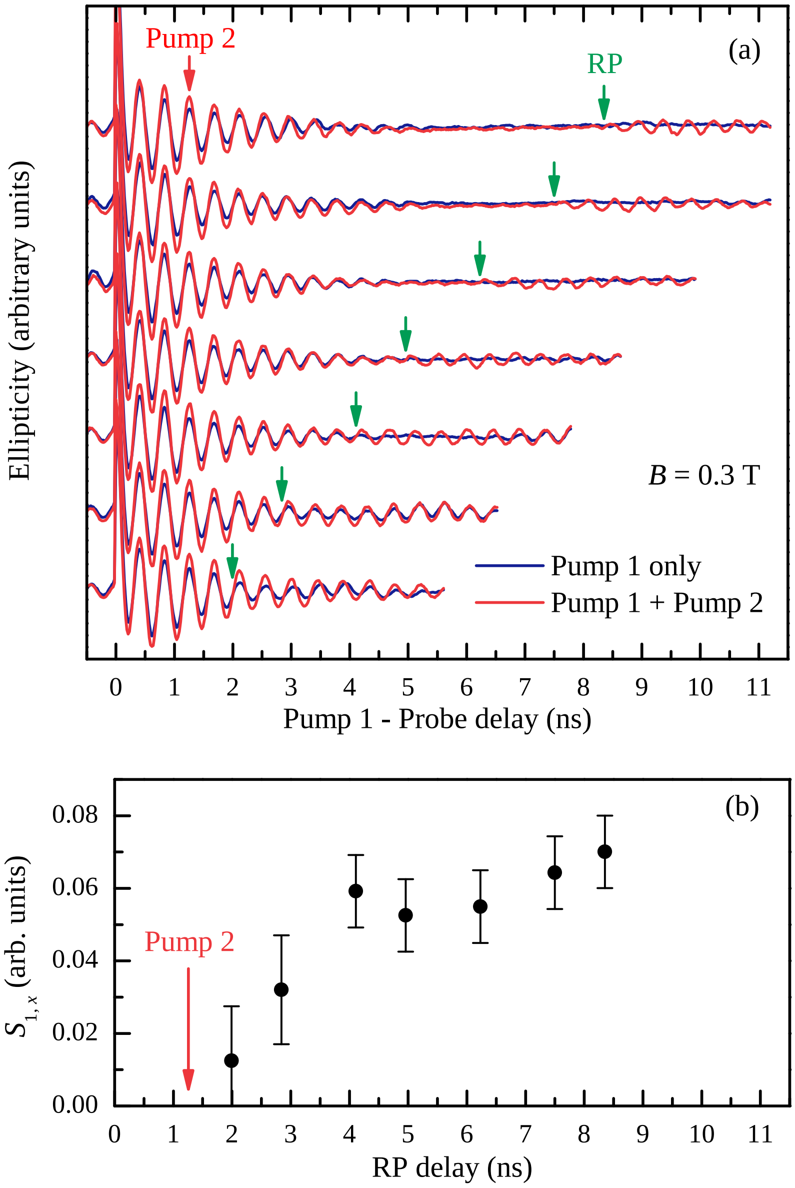

Figure 4.8 **(a)** Ellipticity traces with and without pump 2 (red and blue , respectively) for different delays of RP (green arrows) relative to the arrivals of pump 1 and pump 2 (red arrow). The delay is chosen such that RP hits in a rising edge of an oscillation (spins pointing along y). The red traces (with pump 2) show oscillations after the spin rotation induced by the RP, while the blue ones do not, except in the two lowest curves where echo contributions are still visible. **(b)** x component of the spin ensemble addressed by pump 1, $S_{1,x}$, in dependence of the RP delay.

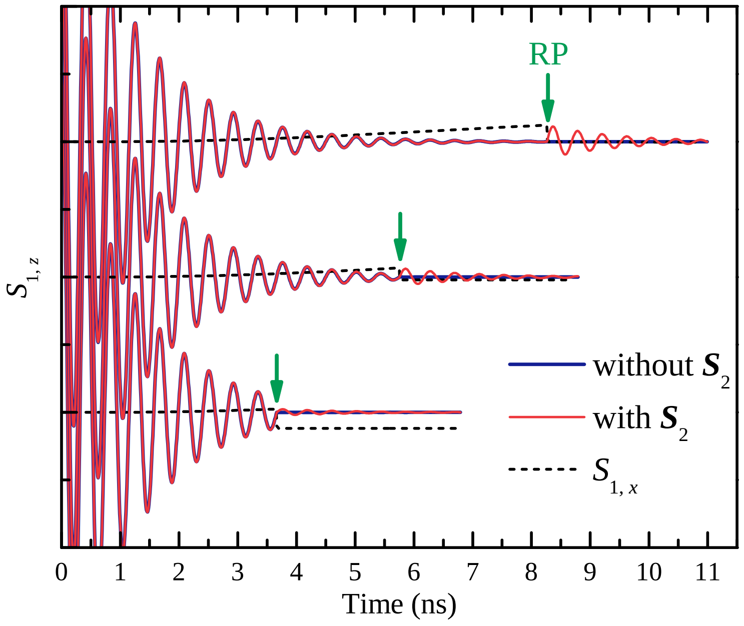

Figure 4.9 Model calculations of $\boldsymbol{S}_1(t)$ with and without interaction with $\boldsymbol{S}_2$ (red and blue traces, respectively) before and after $\pi/2$ rotations at different RP delays. The evolution of $S_{1,x}$ is shown by the dashed black line. The calculations were performed by S. E. Economou.

cillations become apparent. The actual rise time of $S_{1,x}$ depends on the magnetic field and the coupling constant J. The evolution of the data in Fig. 4(b) reflects only a quarter of an oscillation period of $S_{1,x}$. Disregarding the echo contributions in the measured data for RP delays < 4 ns, the model is in good agreement with the experiment.

The coupling constant J, as a free parameter in the model, was varied until the calculations mimicked the data most closely. Accordingly, its strength was found to be $J = 0.05$ μeV. This is about an order of magnitude smaller than the estimations in Ref. [Spa11c] of $J \approx 1$ μeV, which were based only on the phase shift of the spin precession due to the spin-spin interaction. On the other hand, the results from the tomography experiments presented above confirm the qualitative predictions and still exclude classical dipole-dipole and nuclei-mediated interaction mechanisms, which were estimated to be on the order of 10^{-9} to 10^{-5} μeV [Spa11c]. The optical RKKY mechanism [Pie02] is still most likely responsible for the observed spin-spin interaction.

Moreover, the experiments provide the first all-optical tomography of a spin ensemble. A complete tomography for the system of both interacting spin ensembles would also require a measurement of all three spin-vector components of the ensemble oriented by pump 2 to determine the 15 independent components of the density matrix. For that purpose another probe resonant with pump 2 and another detuned rotation pulse would have to be introduced. Based on the experimental results presented above one can say that there is no fundamental obstacle to do this. The basic features and the feasibility of an all-optical spin tomography are demonstrated.

4.3 Revealing mode-locked spin patterns

In this section an additional experiment is presented that shall provide information about the mode-locked electron spins within an ensemble. This is of particular interest concerning the spin-spin interaction, see Sec. 2.4 and Sec. 4.2, which was studied as an interaction between two subsets of spins that were treated as one spin vector each. However, this interaction is most likely also relevant between single spins within an ensemble. Therefore, it is necessary to know the relative orientations between the single spins as they fundamentally influence the interaction.

In usual pump-probe measurements of a spin-ensemble polarization, the monitored signal is formed by simple cosine oscillations, damped due to inhomogeneous dephasing. In the experiment presented in this section, the excitation protocol is adjusted such that higher harmonics of the fundamental oscillation frequency are generated in the observed signal. These oscillations reveal the orientation patterns of the mode-locked ensemble spins. The results have also been published in Ref. [Var14c].

The resident QD electron spins in sample # 11955 (see Sec. 3.3) are initially oriented by pump pulses whose photon energy (as all other photon energies in this experiment) is tuned to the PL maximum. The spin polarization is determined by measuring the probe-beam ellipticity as in the experiments presented in the previous sections. The pump beam is intensity modulated by a chopper. For reference purposes, a simple pump-probe measurement is shown by the top, black curve in Fig. 4.10(a). After orientation at zero delay the spin polarization precesses about the external magnetic field of $B = 1\,\mathrm{T}$. Due to the g factor inhomogeneities within the QD ensemble and the resulting precession frequency distribution the spins dephase on a nanosecond timescale. However, the spins with precession modes locked to the pump-repetition rate rephase before the next pump-pulse incidence at 13.2 ns delay (see Sec. 2.3.1). This is apparent in the signal oscillations at delays $\gtrsim 10\,\mathrm{ns}$ and also at negative delays.

The lower green and orange curves in Fig. 4.10(a) show the effect of an extension to the laser protocol by an additional pulse train called “rectifier”. Like the pump pulses the rectifier pulses are circularly polarized and their pulse area is set to be $\Theta_\mathrm{R} = \pi$. However, the rectifier beam is not modulated so that the spin coherence induced by it is not detected after lock-in amplification, but only the rectifier’s effect on the pump-induced coherence can be observed. Furthermore, the rectifier pulses hit the sample not with a fixed delay relative to the pump incidences, but they

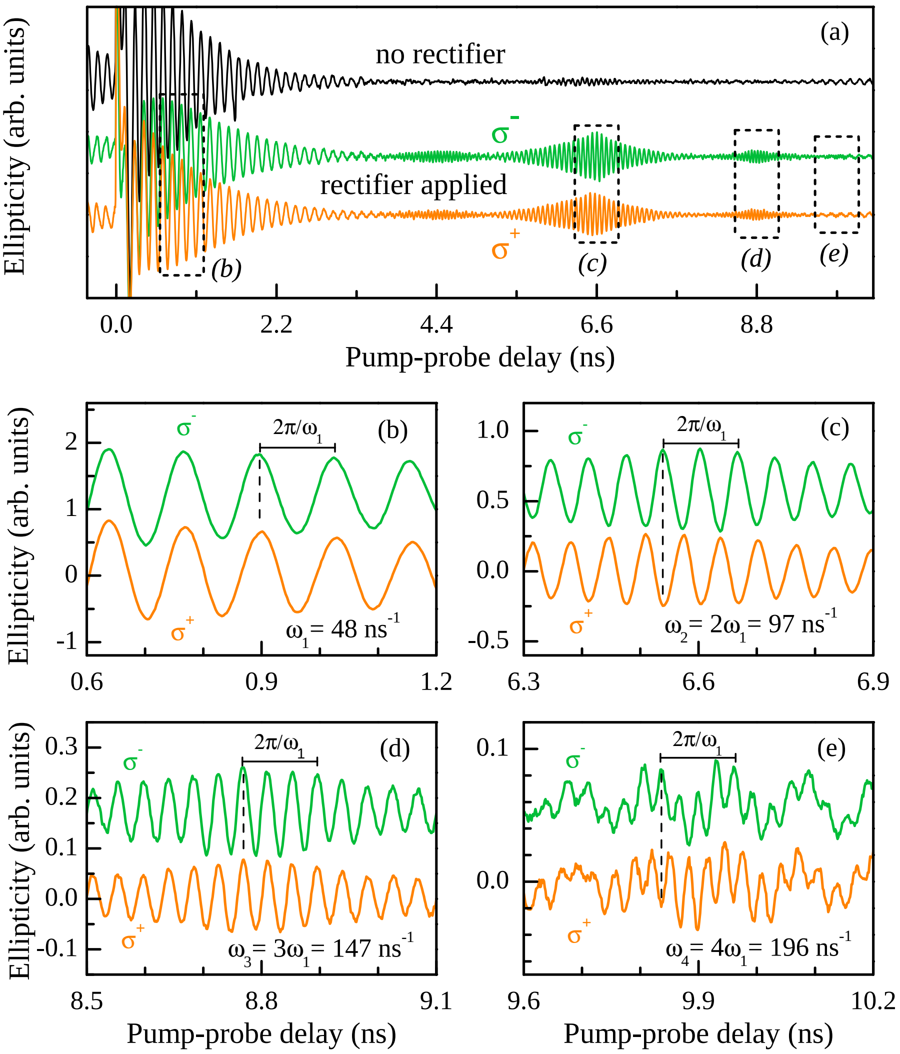

Figure 4.10 (a) Upper black curve: pump-probe ellipticity measurement as a reference. $B = 1\,\mathrm{T}$, $T = 6\,\mathrm{K}$. Lower blue and red curves: measurements when an additional, circularly polarized (σ^- or σ^+, respectively) rectification pulse is applied, arriving at the sample simultaneously with the probe. **(b)–(e)** Closeups of the 0.6-ns delay ranges indicated by the boxes in (a). The observed oscillation frequencies are given in each panel. The superimposed slow oscillation in (e) originates from rephasing mode-locked spins approaching the next pump pulse at 13.2 ns.

arrive at the same moment as the probe pulses. The effect of applying these pulses is the occurrence of signal bursts with differing oscillation frequencies, pronounced at $\frac{1}{3}T_\mathrm{R} = 4.4\,\mathrm{ns}$, $\frac{1}{2}T_\mathrm{R} = 6.6\,\mathrm{ns}$, and $\frac{2}{3}T_\mathrm{R} = 8.8\,\mathrm{ns}$, but also detectable at $\frac{1}{4}T_\mathrm{R} = 3.3\,\mathrm{ns}$, and $\frac{3}{4}T_\mathrm{R} = 9.9\,\mathrm{ns}$ delay. A closer look into these bursts is given in panels (b)–(e) of Fig. 4.10. They show extracts of the lower curves in panel (a) at four distinct delay ranges. Panel (b) magnifies the early precession before 2 ns. The precession frequency here is determined to $\omega_1 = 48\,\mathrm{ns}^{-1}$. The corresponding period $2\pi/\omega_1$ is also marked for comparison with the other panels. The phase of precession is not influenced by the polarization of the rectifier as indicated by the vertical dashed line. This is different for the region around 6.6 ns, depicted in panel (c). Here, the frequency is doubled and the signals are in counter-phase for the two different rectifier polarizations. In panel (d) the ellipticity around $\frac{2}{3}T_\mathrm{R} = 8.8\,\mathrm{ns}$ oscillates with a frequency three times higher than the original precession frequency ω_1 in panel (a) and without a phase change between σ^+ and σ^- rectifier polarization. The signal is similar to that around $\frac{1}{3}T_\mathrm{R} = 4.4\,\mathrm{ns}$. In the range around $\frac{3}{4}T_\mathrm{R} = 9.9\,\mathrm{ns}$ delay shown in panel (e) a frequency component four times higher than the one in panel (a) is observed, whose phase switches with the rectifier polarization. It is superimposed by the signal oscillating with ω_1 from rephasing mode-locked spins approaching the next pump pulse. The fourfold frequency also occurs around $\frac{1}{4}T_\mathrm{R} = 3.3\,\mathrm{ns}$ delay.

To understand the oscillations with multifold frequencies, the distribution of mode-locked electron spins has to be considered. These spins precess with Larmor frequencies ω fulfilling the PSC $\omega = 2\pi N/T_\mathrm{R}$, see Eq. (2.34). As an example, the six lowest precession modes fulfilling the PSC are schematically shown in Fig. 4.11(a). These modes are chosen for demonstration purposes. In the experiment, around 10 modes are excited by the finite pump-pulse width of about 1 meV and the central frequency of $\omega_1 = 48\,\mathrm{ns}^{-1}$ corresponds to slightly more than 100 precessions between two pump pulses. This mode spectrum is also depicted below in Fig. 4.12(a). Nevertheless it is clear that, although the net spin polarization vanishes apart from the range around pump incidences due to dephasing, the mode-locked spins form well-ordered patterns at certain fractions of the pump-pulse separation, illustrated by the arrow arrangements in Fig. 4.11(a): At $\frac{1}{2}T_\mathrm{R} = 6.6\,\mathrm{ns}$ half of the mode-locked spins point in z while the other half points in $-z$ direction. At $\frac{1}{4}T_\mathrm{R} = 3.3\,\mathrm{ns}$ and $\frac{3}{4}T_\mathrm{R} = 9.9\,\mathrm{ns}$, one quarter of the spins each point along z, $-z$, y, and $-y$. Furthermore, at $\frac{1}{3}T_\mathrm{R} = 4.4\,\mathrm{ns}$ and $\frac{2}{3}T_\mathrm{R} = 8.8\,\mathrm{ns}$ the spin ensemble splits like a three-bladed wind turbine with an angle of 120° between each third of the spins.

Without further intervention the mode-locked spins compensate to a net spin polarization of zero at these certain times as seen in the upper, black curve in Fig. 4.10(a). But the experiment shows that the recorded spin polarization can reflect those spin patterns, if together with every linearly polarized probe pulse the circularly polarized rectifier pulse hits the sample. The rectifier introduces an imbalance in the spin-orientation pattern by exploiting the Pauli blocking, which prevents the excitation of an electron with spin parallel to the one of the resident

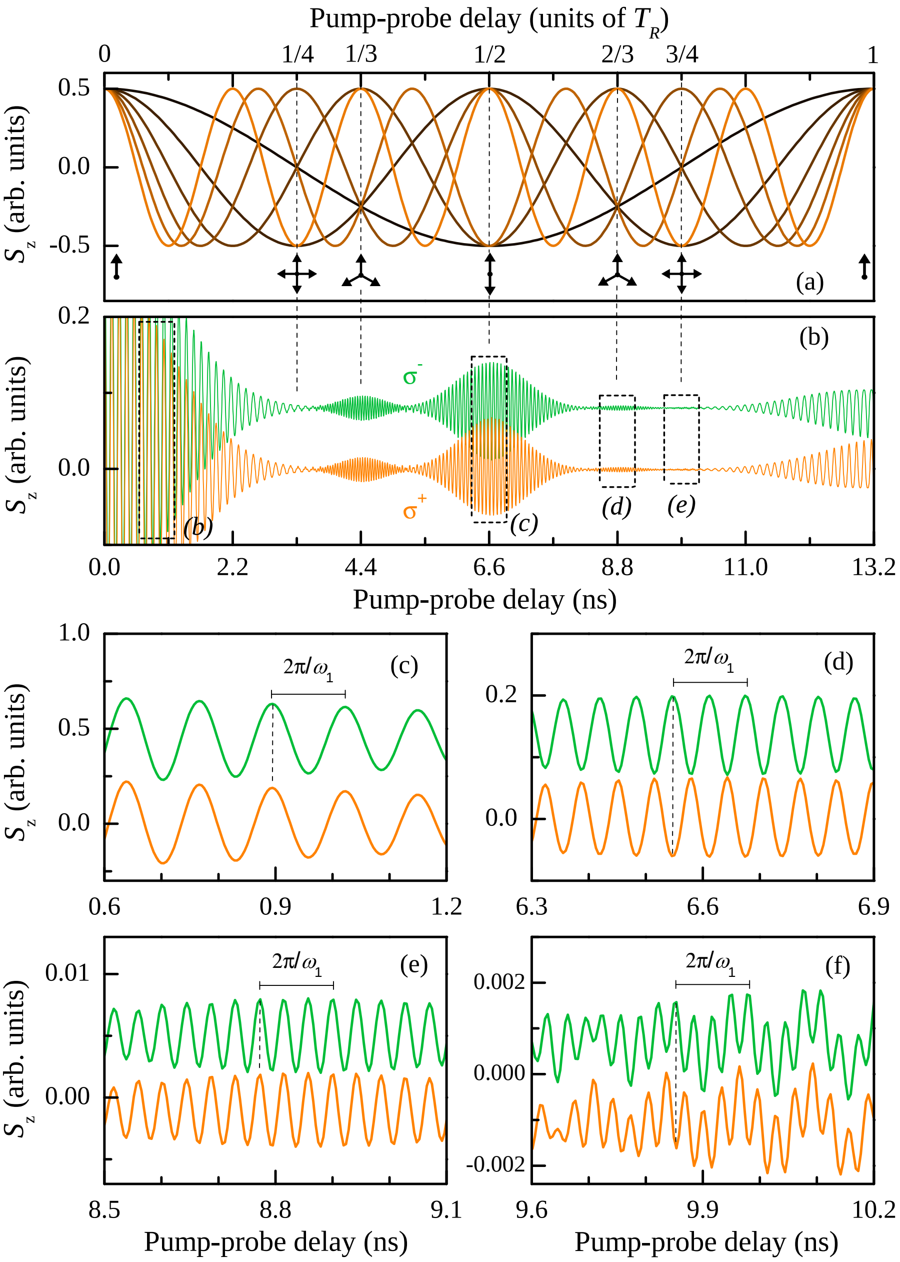

Figure 4.11 **(a)** Model of the six lowest precession modes fulfilling the PSC, Eq. (2.34), between two pump pulses. At zero delay all spins point along z. At $\frac{1}{4}T_\mathrm{R} = 3.3\,\mathrm{ns}$ and $\frac{3}{4}T_\mathrm{R} = 9.9\,\mathrm{ns}$ one quarter of the spins each point along z, $-z$, y, and $-y$. At $\frac{1}{3}T_\mathrm{R} = 4.4\,\mathrm{ns}$ and $\frac{2}{3}T_\mathrm{R} = 8.8\,\mathrm{ns}$ the spins point, equally distributed, in one of three directions, separated by 120°. At $\frac{1}{2}T_\mathrm{R} = 6.6\,\mathrm{ns}$ half of the spins point along z, the other half along $-z$. These spin patterns are illustrated by the arrow arrangements at the bottom. **(b)–(f)** Calculated net electron-spin polarization under the influence of σ^- or σ^+ polarized rectification pulses. Calculations performed by I. A. Yugova assuming $|g_\mathrm{e}| = 0.56$ and $\Delta g_\mathrm{e} = 0.01$.

electron. Since the spin states are superpositions of the up and down states $|\uparrow\rangle$ and $|\downarrow\rangle$ along z, see Sec. 2.2, a σ^- polarized rectifier creates an electron-hole pair (with electron spin up, along $+z$), but only if the superposition state of the resident electron contains a spin-down component, along $-z$. The spin-up component remains unexcited while the spin down component is excited to a trion complex with two electrons in a singlet state, which do not contribute to the spin polarization. Thus, the contribution of a spin-down component to the net spin polarization is disabled. As a consequence of this "rectification" the spectrum of mode-locked electron spins is modified.

The effect of the rectifier on the spin polarization can be described quantitatively by the same formulas as the pump action given in Eq. (2.33) for circularly polarized π pulses (see also Ref. [Yug09] and the supplemental material of Ref. [Var14c]). In the following theoretical discussion based on model calculations by I. A. Yugova, contributions to the resident electron-spin polarization by trion recombination as well as transverse spin relaxation are neglected, since at the magnetic field of $B = 1\,\mathrm{T}$ the hole-spin precession annihilates any trion contribution and the coherence time T_2 is two orders of magnitude longer than the pump-pulse separation T_R [Gre06b]. Extending the theoretical model for a π-pulse excitation of a single spin by additional rectifier pulses leads to the following expression for the z component of the spin polarization right before the rectifier incidence (after an infinite train of pump-rectifier excitations):

$$\begin{aligned} S_z^{t\to T_\mathrm{D}^-} &= \mp\frac{\eta}{16}\{4\cos(\omega T_\mathrm{D}) + \cos[2\omega(T_\mathrm{D} - T_R/2)] + \cos(\omega T_R)\} \qquad (4.3)\\ \eta &= \frac{1}{1-\frac{1}{8}\{\cos[2\omega(T_\mathrm{D}-T_R/2)] + \cos(\omega T_R)\}}\\ &\approx 1 + \frac{1}{8}\{\cos[2\omega(T_\mathrm{D}-T_R/2)] + \cos(\omega T_R)\}\,. \end{aligned}$$

The top (bottom) sign - (+) in Eq. (4.3) corresponds to σ^+ (σ^-) polarized pulses. ω is the precession frequency of the regarded spin mode, $T_\mathrm{R} = 13.2\,\mathrm{ns}$, and T_D is the delay between pump and rectifier pulses, which varies jointly with the pump-probe delay. The dependence of the spin polarization on that delay is shown in Fig. 4.12(b). The black cosine curve depicts the precession of the spin belonging to the central precession mode in panel (a) without rectifier action. The orange curve, instead, shows the impact of the rectifier pulses (shifted jointly with the probe pulses) on the pump-induced spin coherence. The spin polarization is "rectified" in the sense that the negative polarization cycles are cut off. Consequently, the signal contains also higher harmonics of the fundamental precession frequency as shown by the Fourier transformation in Fig. 4.12(c). Mathematically these higher harmonic terms originate from the multiplication of the cosine functions in Eq. (4.3).

After averaging the spin polarization over the precession frequency spread, these terms finally result in the signal bursts in Fig. 4.11(b)–(f) at $\frac{1}{4}T_R$, $\frac{1}{3}T_R$, $\frac{1}{2}T_R$, $\frac{2}{3}T_R$, and

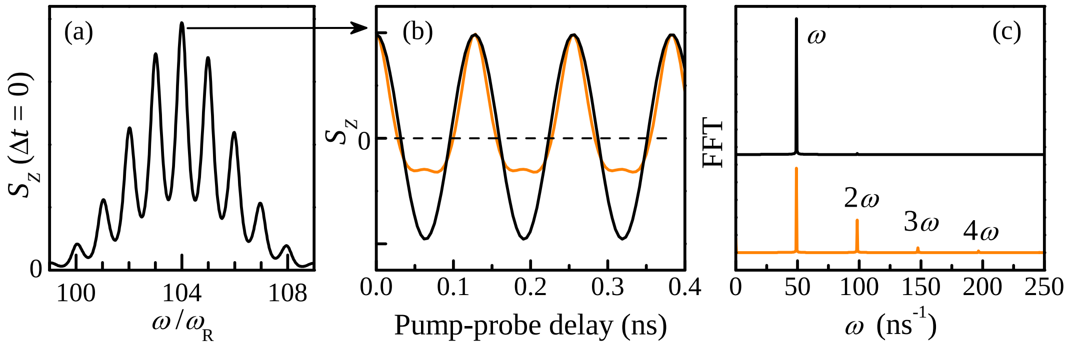

Figure 4.12 **(a)** Precession frequency mode spectrum simulated for zero pump-probe delay at $B = 1\,\mathrm{T}$ without the rectifier. **(b)** Spin polarization of the most pronounced precession mode with $\omega = 104\,\omega_\mathrm{R} = 104 \cdot 2\pi/T_\mathrm{R}$ in dependence of the pump-probe delay, without the rectifier (black) and with the rectifier (orange). **(c)** Fourier transformation of both curves shown in panel (b). Calculations performed by I. A. Yugova.

$\frac{3}{4}T_R$ delays. Around these delays generally determined by $T_\mathrm{D} = T_\mathrm{R}/M$, $M \in \mathbb{Z}^*$, the different harmonic terms interfere constructively and lead to a signal oscillating with a frequency, which is M-times the central single-spin Larmor precession frequency. Considering the spin patterns represented by the arrow arrangements in Fig. 4.11(a), M corresponds to the number of arrows in the arrangement and determines the fraction $1/M$ of spins that are parallel to the z direction.

The calculated signals for co- and counter-polarized rectifiers in Fig. 4.11(b)–(f) are in good agreement with the experimental results presented in Fig. 4.10. The smaller amplitudes of bursts at $\frac{2}{3}T_R$ and $\frac{3}{4}T_R$ in Fig. 4.11(b)–(f) may be due to the fact that nuclear effects, which lead to frequency focusing (see Sec. 2.3.1), were not considered in the calculations. However, the complex spin polarization signals induced by the additional rectifier pulses reveal the orientation patterns of mode-locked spins within an inhomogeneous ensemble, which cannot be accessed by standard pump-probe techniques due to the inherent ensemble dephasing. Thus, components of a tomography of these single spin modes are provided. Furthermore, the experiment grants new insights that might be necessary or help to understand a possible spin-spin interaction within an ensemble of spins, in contrast to the studied interaction between two well-separated subsets (see Sec. 2.4 and Sec. 4.2).

5 Hole-spin coherence

Besides the spin of electrons, the spin of holes might serve as a qubit candidate in semiconductor materials. While there have been several studies on single hole spins [DeG11, Gre11, God12], the research on hole-spin ensembles has up to now not come to an extent as large as on electron-spin ensembles. A reason for that is, e. g., the faster inhomogeneous dephasing alongside with slower spin precessions, determined by smaller g factor values, as compared to electron spins in similar QD ensembles. On the other hand, due to the shape of the valence band p-orbitals, much weaker interaction with nuclei is expected (see Sec. 2.1.1). Therefore, longer coherence times than for electrons, whose decoherence processes are dominated by electron-nuclear interactions [Mer02], are expected. The electron advantage of nuclear-supported mode-locking (see Sec. 2.3.1) is also expected to be nonexistent.

However, experimental results of optical pump-probe studies which show hole-spin mode-locking in a QD ensemble are presented in Sec. 5.1. This spin mode-locking (SML) allows to overcome the dephasing problem and to gain access to hole-spin coherence studies. The experiments are similar to those performed on electron-spin ensembles [Gre06b] using pump doublets. They show the transition between the RSA and the SML regime (see Sec. 2.3.1) within one hole-spin ensemble and reveal new insight in the role of nuclear-spin contributions to ensemble spin precessions. In Sec. 5.2 the hole-spin coherence time is studied with a focus on its temperature dependence to learn more about possible decoherence mechanisms. The measurements exploit the hole SML and optically induced spin echoes. A pulse sequence leading to multiple of such echoes, comparable to the Carr-Purcell-Meiboom-Gill protocol used in nuclear magnetic resonance experiments, is implemented optically in experiments described in Sec. 5.3. By doubling the number of these pulses, the hole-spin coherence time is shown to be elongated.

The results presented in Sec. 5.1 and Sec. 5.2 have been published in Refs. [Var12, Var13, Var14a]; the results of Sec. 5.3 in Ref. [Var14d].

5.1 Hole-spin mode-locking

The experiments on hole-spin mode-locking are mainly conducted with the setup described in Sec. 3.2.1 using a single-color pump-probe scheme with pump doublets. The pump beam is split, one part is delayed by a fixed delay line, and then both parts are recombined. As a result, the pump beam hits the sample with two pulses within the laser repetition period of $T_{\mathrm{R}} = 13.2\,\mathrm{ns}$. These pulses are in the following also called pump 1 and pump 2, just as the two pump-pulse trains in Sec. 4.2. In the experiments described in this section, however, the two pulse trains are both modulated and degenerate in energy so that they excite the same QD ensemble, solely delayed by a certain time $T_{\mathrm{D}} < T_{\mathrm{R}}$. The pump and probe photon energy is tuned to the maximum of the PL ground state emission plotted in Fig. 3.6 for the used sample # 11376 annealed at 960 °C (see Sec. 3.3).

Figure 5.1(a) shows time-resolved ellipticity measurements for single- and double-pump excitation. The upper, black curve shows the ellipticity signal recorded when only pump 1 is applied. Signal oscillations can be seen shortly before and after pump incidence at zero pump-probe delay. The middle curve shows the ellipticity signal when only pump 2 is applied. The resulting curve is very similar to the upper one except that it is temporally shifted by $T_{\mathrm{D}} = T_{\mathrm{R}}/6 = 2.2\,\mathrm{ns}$, which is the fixed delay between pump 1 and pump 2. The lower, red curve shows the signal, which is recorded when both pump 1 and pump 2 are applied. Here, not only the oscillations around the two pump incidences, but also additional signal bursts appear at multiples of the pump separation T_{D}. These bursts and the signal oscillations before the pump incidences are the result of mode-locked carrier spins (see below).

Within the first nanosecond after a pump incidence, the signal consists of contributions from photocreated and resident carriers. The photocreated neutral and charged excitons radiatively decay on a 0.5-ns timescale [Gre06a], while the resident carrier contribution decays on the scale of the dephasing time T_2^*, which depends on the spread of precession frequencies within the ensemble. The latter signal contribution recovers on the same timescale T_2^* shortly before the next pump incidence, indicating the mode-locking effect on resident carriers, whose coherence time is larger than the pump-pulse separation (see Sec. 2.3.1). In the ellipticity measurements, the signal at negative delays before pump-pulse arrival is mainly consisting of one slow oscillation corresponding to a hole-spin g factor of 0.14, determined from the precession frequency dependence on the magnetic field in Fig. 5.2(a). The precession frequency, dephasing time, and signal amplitude ε_0 are, according to Eq. (2.28), obtained by fits to the ellipticity signal $\varepsilon(\Delta t)$ with

$$\varepsilon(\Delta t) = \varepsilon_0 \cos(\omega_{\mathrm{L}} \Delta t + \phi_\varepsilon) \mathrm{e}^{-(\Delta t - t_0)^2/(2T_2^{*2})} + c\,. \tag{5.1}$$

ϕ_ε, t_0, and c are a phase, time delay offset, and ellipticity offset, respectively. Such a slow oscillating contribution can also be recognized in the signal at positive delays, even though it is superimposed by a strong signal with faster oscillation frequency, which is assigned to the electron g factor of ~ 0.55 [Sch11]. This is the contribution of photocreated excitons in neutral QDs radiatively decaying after pump excitation.

The small number of hole-spin oscillations before pump incidence or within a burst is due to the large g factor inhomogeneity of $\Delta g_{\mathrm{h}}/g_{\mathrm{h}} \approx 35\%$. In comparable n-doped QD ensembles the electron g factor inhomogeneity is only $\Delta g_{\mathrm{e}}/g_{\mathrm{e}} \approx 0.7\%$ [Gre06a].

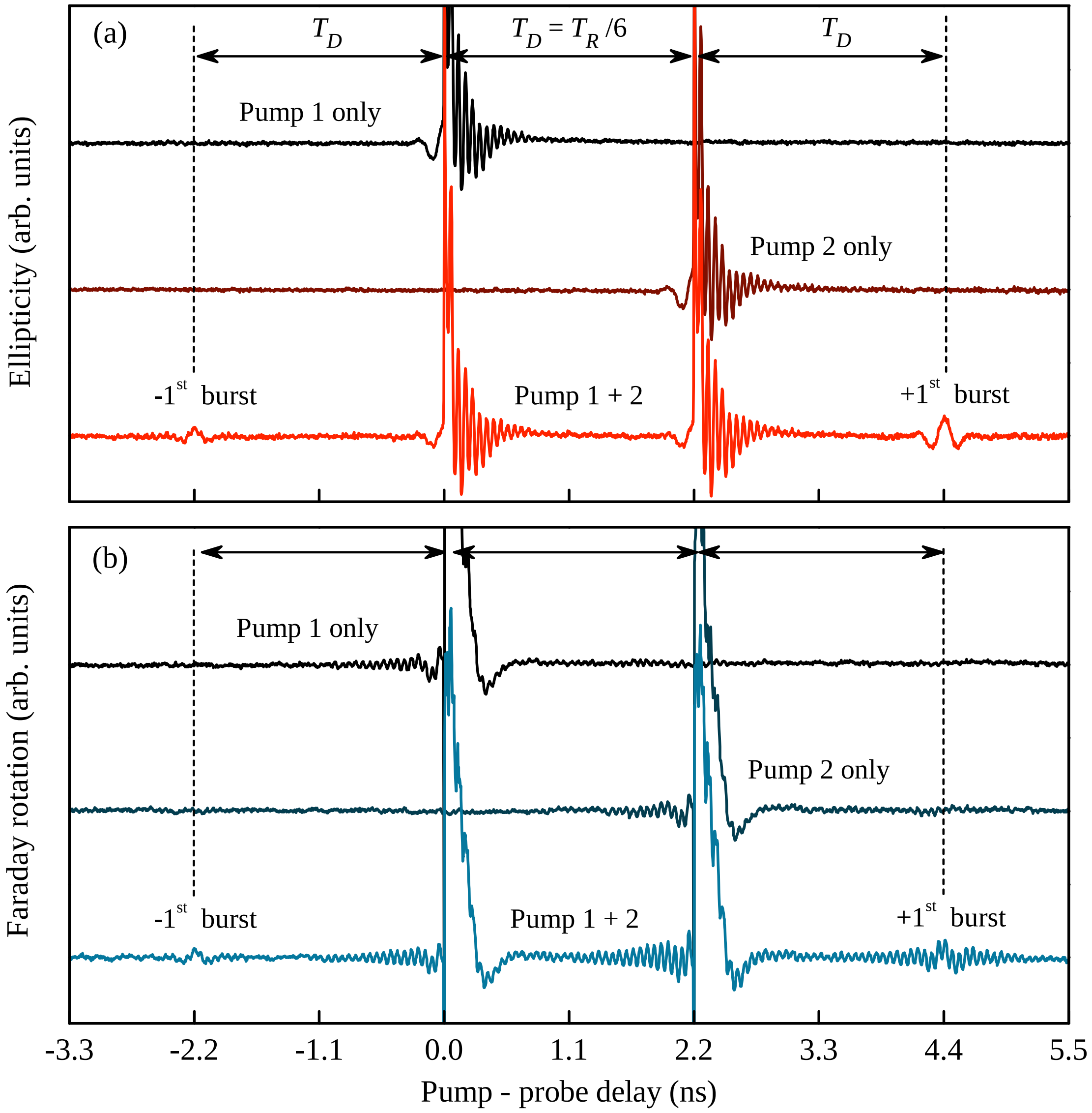

Figure 5.1 Ellipticity **(a)** and Faraday rotation **(b)** measurements showing hole- and electron-spin mode-locking, respectively, under equal experimental conditions. The two upper curves in each panel show the signals for single-pump excitation with $T_\mathrm{R} = 13.2\,\mathrm{ns}$. The lower curve in each panel shows the signal for double-pump excitation with $T_\mathrm{D} = T_\mathrm{R}/6 = 2.2\,\mathrm{ns}$. Both pumps are co-polarized. $T = 6\,\mathrm{K}$, $B = 2\,\mathrm{T}$.

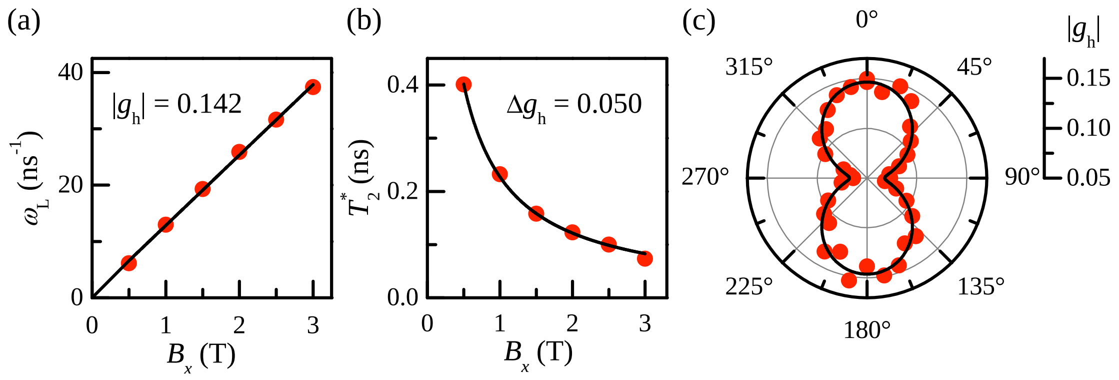

Figure 5.2 Hole-spin g factor properties determined from the ellipticity signal burst around 4.4 ns delay, shown in Fig. 5.1(c). **(a)** Larmor precession frequency ω_L in dependence on the magnetic field B_x. A fit with Eq. (2.13) provides an absolute g factor of $|g_\mathrm{h}| = 0.142 \pm 0.002$. **(b)** Dephasing time T_2^* in dependence on the magnetic field along the x axis B_x. A fit with $T_2^*(B) = [(\Delta g_\mathrm{h}\mu_\mathrm{B}B)/(\sqrt{2}\hbar) + 1/T_{2,\mathrm{n}}^{\mathrm{inh}}]^{-1}$ provides a width of the g factor distribution of $\Delta g_\mathrm{h} = 0.050 \pm 0.001$. The zero field dephasing is $T_{2,\mathrm{n}}^{\mathrm{inh}} = (0.58 \pm 0.08)$ ns. **(c)** In-plane g factor depending on the magnetic field orientation α relative to the x axis. The data are fitted according to $g_\mathrm{h}^2 = g_{\mathrm{h},x}^2 \cos^2\alpha + g_{\mathrm{h},y}^2 \sin^2\alpha$, providing $|g_{\mathrm{h},x}| = 0.146 \pm 0.003$ and $|g_{\mathrm{h},y}| = 0.068 \pm 0.004$.

The width of the g factor spread Δg_h is determined from a fit to the magnetic field dependence of the dephasing time $T_2^*(B) = [(\Delta g_\mathrm{h}\mu_\mathrm{B}B)/(\sqrt{2}\hbar) + 1/T_{2,\mathrm{n}}^{\mathrm{inh}}]^{-1}$, which is shown in Fig. 5.2(b). Due to the strength of the signal amplitude of mode-locked hole spins, it is assumed that the hole-spin coherence time T_2 is large enough to be neglected with respect to the dephasing time. The main contribution to the dephasing time is the broad distribution of g factors. The zero field dephasing time is determined to be $T_{2,\mathrm{n}}^{\mathrm{inh}} = 0.58$ ns for holes, which is ten times smaller than for electrons in similar QD structures [Gre06a]. Figure 5.2(c) shows the in-plane g factor of hole spins for different orientations of the magnetic field vector. The data demonstrate a strong anisotropy resulting from the shape of the QDs and their anisotropic strain in combination with the p-type wave function of holes (see Sec. 2.2.2). During all other measurements discussed in this chapter, the magnetic field vector was fixed pointing along x so that $|g_\mathrm{h}| = |g_{\mathrm{h},x}|$.

The signal oscillations at the burst positions -2.2 ns and 4.4 ns show the same frequency as the slow oscillating contributions before and after pump incidence and prove the mode-locking of resident hole spins in the studied QD ensemble. The bursts are a result of the application of both pump 1 and pump 2. The additional excitation pulses change the phase synchronization condition (PSC) for mode-locked spins, since now the spins being in phase every T_D are efficiently pumped. This leads to constructive interference of the spin polarization and to signal bursts at these specific times. T_D is chosen to be a sixth of the laser repetition period here,

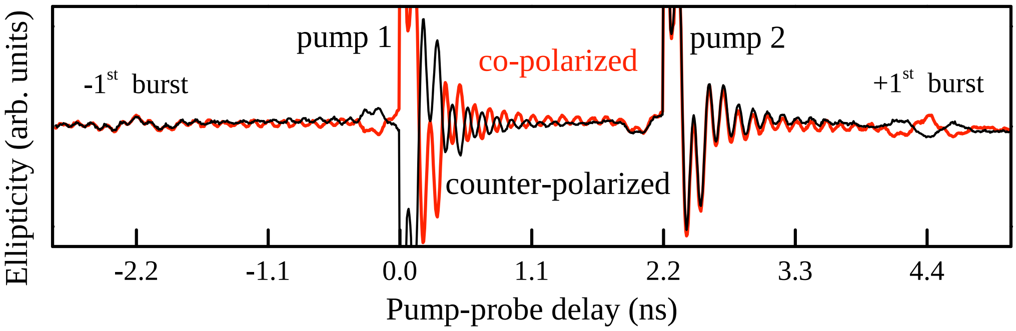

Figure 5.3 Ellipticity measurements with co-polarized (red) and counter-polarized (black) pump-doublet excitation. The altered PSC, due to the opposing spin orientation by pump 1, causes a phase jump of π in the +1st burst signal. $B = 1\,\mathrm{T}$.

because in case of commensurability ($T_\mathrm{D} = T_\mathrm{R}/n,\ n \in \mathbb{N}$) the new PSC induced by the additional pump,

$$\omega_\mathrm{L} = \frac{2\pi}{T_\mathrm{D}} M\,,\ \ M \in \mathbb{N}\,, \tag{5.2}$$

just substitutes the old one given in Eq. (2.34). If T_D was not commensurable with T_R, Eqs. (2.34), (5.2), and $\omega_\mathrm{L} = \frac{2\pi}{T_\mathrm{R}-T_\mathrm{D}} M'$, $M' \in \mathbb{N}$ would have to be fulfilled, which would lead to more complex interference patterns (see Ref. [Gre07c]).

The validity of the PSC induced by a pump doublet can be demonstrated by inverting the optical polarization of one pump beam. Figure 5.3 shows ellipticity measurements with both pump beams applied. The red curve is similar to the already discussed case shown by the lower curve in Fig. 5.1(a), where both pump beams are co-polarized. Signal bursts appear every $T_\mathrm{D} = 2.2\,\mathrm{ns}$. In the measurement providing the black curve, the polarization of pump 1 was switched with respect to pump 2. The Glan-Taylor prism in the pump beam is for this purpose moved in front of the first beam splitter splitting the two pump beams and a half-wave plate is inserted in the detoured beam part, so that its linear polarization can be rotated by 90 °. After passing the PEM, pump 1 and pump 2 are then counter-polarized and the spins are oriented in opposite directions by pump 1 and pump 2. The corresponding PSC reads

$$\omega_\mathrm{L} = \frac{2\pi}{T_\mathrm{D}} \left(\tilde{M} + \frac{1}{2}\right)\,,\ \ \tilde{M} \in \mathbb{N}\,. \tag{5.3}$$

Additionally, $T_\mathrm{R}/T_\mathrm{D}$ must be an even integer here. The mode-locked spins, which fulfill this PSC, perform a half-integer number of precessions between both pumps and are in phase every T_D, but with $2T_\mathrm{D}$-periodically alternating orientation. As a consequence, the signals around pump 1 and the +1st burst show a phase jump of π compared to the case of co-polarized excitation, while the signals around pump 2 and the -1st burst are in phase.

The measured signal changes substantially when switching the measured variable from ellipticity to Faraday rotation. In Fig. 5.1(b) Faraday rotation measurements are presented that were recorded under the same conditions as the ellipticity measurements in panel (a) discussed above. The comparison between both measurements reveals two important differences: first, the signal of photocreated carriers after a pump incidence is strongly suppressed. Second, the signals of mode-locked spins before a pump incidence and within a signal burst are no longer dominated by hole spin but rather by electron spin contributions, distinguishable through the faster signal oscillation assigned to the larger electron g factor. Apparently, positively and negatively charged QDs (containing resident holes and electrons, respectively) can be found in the nominally undoped sample. The differences in the measured signals can be explained by the spectral sensitivity of the measured variables, Faraday rotation and ellipticity, and the interaction between carrier and nuclear spins.

Since the Faraday rotation is an odd function of the detuning between the probe light frequency and the trion resonance at which the spins are orientated (see Sec. 2.5), the signal amplitude should vanish in case of a degenerate pump-probe scheme as used in these experiments, where the detuning between excitation and probing is zero. This is true as long as no spectral shift or asymmetry in the oriented spin distribution is present and explains the weak signal of photocreated carriers after pump incidence in Fig. 5.1(b). Due to the inhomogeneous broadening in a QD ensemble and asymmetries in the PL spectrum together with the finite laser linewidth, the Faraday rotation signal does not vanish completely.

The appearance of strong electron signals before pump incidence and within a burst demands a closer look into the nuclear involvement in the mode-locking of carrier spins. It was shown that spin flip-flop processes with the QD nuclei lead to the precession-frequency focusing of optically oriented resident electron spins such that the number of spins fulfilling the PSC within the ensemble is enhanced (see Sec. 2.3.1). The local nuclear spin polarization within a QD, which thereby builds up, and its induced effective magnetic field may persist for hours if the sample is held in darkness. This nuclear field can, e. g., maintain the PSC modified by a second pump, see Eq. (5.2), for a certain amount of time even when one of the pump beams is switched off [Gre07b]. This is demonstrated by the Faraday rotation measurement in Fig. 5.4(a). After treatment of the system by the double-pump protocol for at least 20 min the pump-probe delay was set to 2.06 ns, shortly before pump 2 incidence, see Fig. 5.1(b), where the signal of mode-locked electrons shows up. Then, the beam path of pump 2 was blocked (time zero) and the Faraday rotation signal was recorded in real time. Besides a sharp drop to half of the initial signal amplitude, which is due to the reduction of stray light on the photo detector, an exponential decay with a time constant of $\tau = 30\,\mathrm{s}$ to the same signal level as in the case without pump 2 can be observed.

In contrast to that, the mode-locked hole-spin signal in Fig. 5.4(b) disappears instantaneously after blocking pump 2. Here, the ellipticity amplitude was recorded

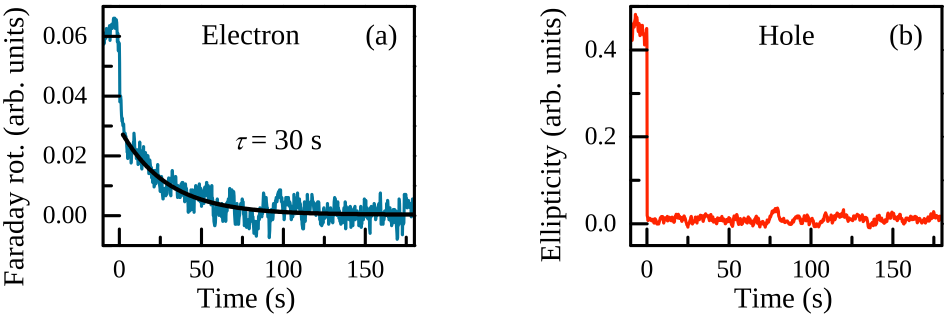

Figure 5.4 **(a)** Real time relaxation of the Faraday rotation amplitude at a fixed delay of 2.06 ns (mode-locked electron-spin signal shortly before pump 2 incidence) after switching off pump 2 at time zero. Beforehand, the system was exposed to the pump-doublet protocol for 20 min. The black line is an exponential decay fitted to the blue data. The decay time is determined to be $\tau = 30$ s. **(b)** Relaxation kinetics of the ellipticity amplitude at a fixed delay of 4.12 ns (mode-locked hole-spin signal in the +1st burst). $B = 2$ T.

in the maximum of the +1st signal burst, at a pump-probe delay of 4.12 ns, where no electron signal is observed, see Fig. 5.1(a). The instantaneous disappearance shows that no measurable nuclei-induced frequency focusing of precession modes occurs for hole spins. This is a clear hint that the hyperfine interaction of hole spins is much weaker than that of electron spins, which is in agreement with the experimental findings in Refs. [Fal10, Che11].

The nuclei-induced frequency focusing, however, is the reason for the strong Faraday rotation signal of mode-locked electron spins in Fig. 5.1(b), because the nuclear spin flip-flop processes cause an asymmetry in the spectral distribution of the electron-spin polarization [Car09]. Electron spins that do not fulfill the PSC have a nonzero y component when a pump pulse arrives and can thus be rotated about the optical z axis by this pulse, if, e. g. the pulse area is not exactly $\Theta = \pi$ (see Sec. 2.3.2). Hence, the spins acquire a component along x, which influences the nuclear spin-flip rates [Dya73]. Spins in QDs, whose trion resonance is slightly detuned from the central pump frequency acquire a different sign of S_x, depending on the sign of detuning, and with that sign the nuclear spin-flip rates get more or less probable. Therefore, the spin-precession frequency is moved towards the PSC for spins in QDs detuned in one direction, and moved away from the PSC in QDs detuned in the other direction [Car09]. As a consequence, the spin polarization gets stronger in the former QDs and the spectral spin distribution of the probed ensemble becomes asymmetric. This asymmetry leads to the strong Faraday rotation signal of mode-locked electron spins.

As a parenthesis, another Faraday-rotation experiment is presented in the following, in which this effect manifests as well. The experiment was performed on the n-doped sample # 11955 used in Chap. 4. The spin precessions of the resident QD electrons in an external magnetic field of $B = 2$ T were monitored using a nonde-

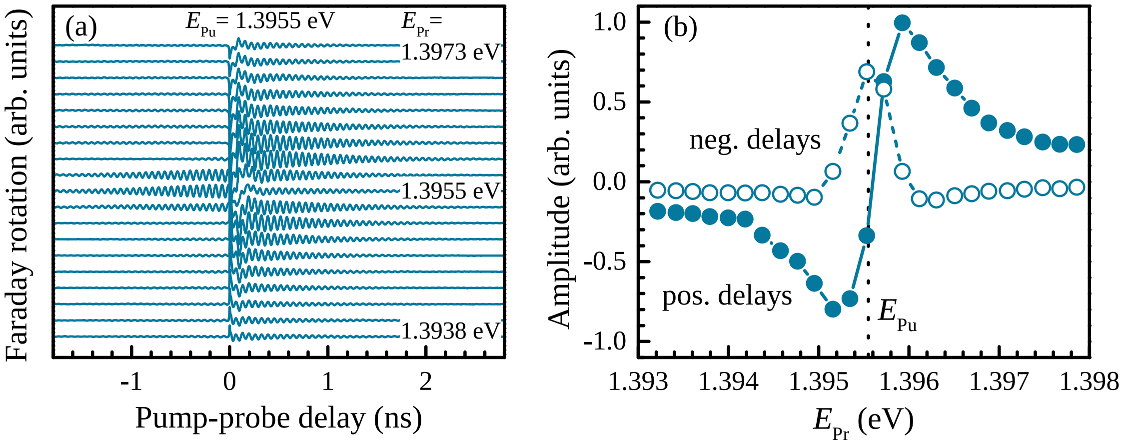

Figure 5.5 (a) Time-resolved Faraday rotation measurements on the n-doped QD sample # 11955 for different probe photon energies E_{Pr} around the pump photon energy $E_{\mathrm{Pu}} = 1.3955\,\mathrm{eV}$ at $B = 2\,\mathrm{T}$. **(b)** Faraday-rotation amplitudes depending on E_{Pr}, determined by Gaussian-damped cosine fits at positive (solid circles) and negative (open circles) pump-probe delays. The signs of these amplitudes are defined by the phase of the corresponding signal oscillation.

generate pump-probe setup. Figure 5.5(a) shows the probe beam's Faraday rotation in dependence on the pump-probe delay for different detunings between the pump photon energy $E_{\mathrm{Pu}} = 1.3955\,\mathrm{eV}$ and the probe photon energy E_{Pr}. Near the resonance condition $E_{\mathrm{Pu}} = E_{\mathrm{Pr}}$ the SML signal at negative delays is stronger than the signal at positive delays, similar to the findings in Fig. 5.1(b). This situation changes, when E_{Pr} is detuned from E_{Pu} in either direction. The SML signal amplitude drops quickly, while the amplitude for positive delays increases at first, as can also be seen in Fig. 5.5(b). This panel shows the Faraday rotation amplitudes for positive and negative delays determined from Gaussian-damped cosine fitting functions. As the spin distribution after pump excitation is symmetric around E_{Pu}, the detuning dependence of the signal amplitude at positive delays properly reflects the asymmetric spectral dependence of the Faraday rotation (compare Fig. 2.11). At negative delays the nuclei-induced asymmetry in the distribution of mode-locked electron spins mentioned in the previous paragraph leads to the strong signal around zero detuning.[1]

The spectral distribution of a mode-locked hole spin polarization, on the other hand, is not influenced by nuclei and stays symmetric around the trion resonance. Therefore, the mode-locked hole spins in the undoped sample # 11376 (see again Fig. 5.1) can well be observed by measuring the probe's ellipticity, which is as an even function of the detuning between the probe light frequency and the trion resonance.

---

[1] This behavior is only pronounced at $B = 2\,\mathrm{T}$. At $B = 4\,\mathrm{T}$, e. g., such a strong Faraday rotation amplitude at negative delays cannot be observed [Gla10]. The reason for that is still unclear.

These differences in the mode-locking mechanism and the spectral sensitivities of Faraday rotation and ellipticity open the opportunity to switch the type of carrier observed in the measured spin dynamics signal and to study mode-locking of electron and hole spins on the same sample.

The difference in the interaction strengths of electron and hole spins with the nuclei manifests particularly in weak magnetic fields. Here, the reduced interaction with nuclei allows hole-spin ensembles to leave the regime of spin mode-locking (SML) and enter the regime of resonant spin amplification (RSA), while this transition is not possible for electron-spin ensembles. Figure 5.6(a) shows time-resolved ellipticity measurements of hole-spin ensemble precessions at different magnetic fields below 200 mT. The field strengths are given in multiples of $B_\mathrm{R} = (\hbar\omega_\mathrm{R})/(g_\mathrm{h}\mu_\mathrm{B}) = 72\,\mathrm{mT}$, with $\omega_\mathrm{R} = 2\pi/T_\mathrm{R}$. At this field, hole spins with the average ensemble g factor of 0.14 perform one precessional evolution between two pump pulses. In this experiment, the pump-pulse repetition period is set to be $T_\mathrm{R} = 6.6\,\mathrm{ns}$ to reduce the number of spin precession modes (see below). This is achieved by adjusting the delay of the second pump such that it is half the initial laser pulse separation of 13.2 ns. As both pump-pulse trains are prepared equally (polarization, pulse area), they can be treated as one with reduced pulse repetition period.

For magnetic fields $B \gtrsim 100\,\mathrm{mT}$ represented by the three curves in the upper graph (SML) in Fig. 5.6(a), the phase and the amplitude of the ellipticity signal shortly before and after a pump incidence do not depend on the magnetic field. The ensemble spin polarization tends to be in an oscillation maximum both for fields whose corresponding average precession frequency match the PSC ($B = 2.0\,B_\mathrm{R}$) and for those whose frequency does not match ($B = 1.5\,B_\mathrm{R}$, $B = 2.5\,B_\mathrm{R}$). This is expected for mode-locked spins. For weaker magnetic fields $B \lesssim 100\,\mathrm{mT}$ represented by the three curves in the lower graph (RSA) in Fig. 5.6(a), on the contrary, the signal amplitude and phase around a pump incidence vary strongly for different magnetic fields. A resonant amplification of the spin signal can be observed for $B = B_\mathrm{R}$ and $B = 0$, while the signal amplitude is almost an order of magnitude smaller for $B = 0.5\,B_\mathrm{R}$.

The choice of the two regimes (SML or RSA) is determined by the ratio $\Delta\omega_\mathrm{L}/\omega_\mathrm{R}$, which is the width of the Larmor frequency distribution in relation to the distance between neighboring precession modes satisfying the PSC, see Fig. 2.7(b). The boundary condition is $\Delta\omega_\mathrm{L} = 0.5\,\omega_\mathrm{R}$, marked by the black, dashed line in Fig. 5.7(a). Above this line, $\Delta\omega_\mathrm{L}$ is sufficiently large to fulfill the PSC [Eq. (2.34)] for several modes in the ensemble, corresponding to the SML regime. The range below the dotted line belongs to the RSA regime, where either one or even no precession mode fulfills the PSC and can be amplified. The mode distance ω_R is fixed by the pump-pulse period T_R, but $\Delta\omega_\mathrm{L}$ can be tuned by the magnetic field. Because of the weak interaction with the nuclei, the hole-spin precession frequency spread is solely

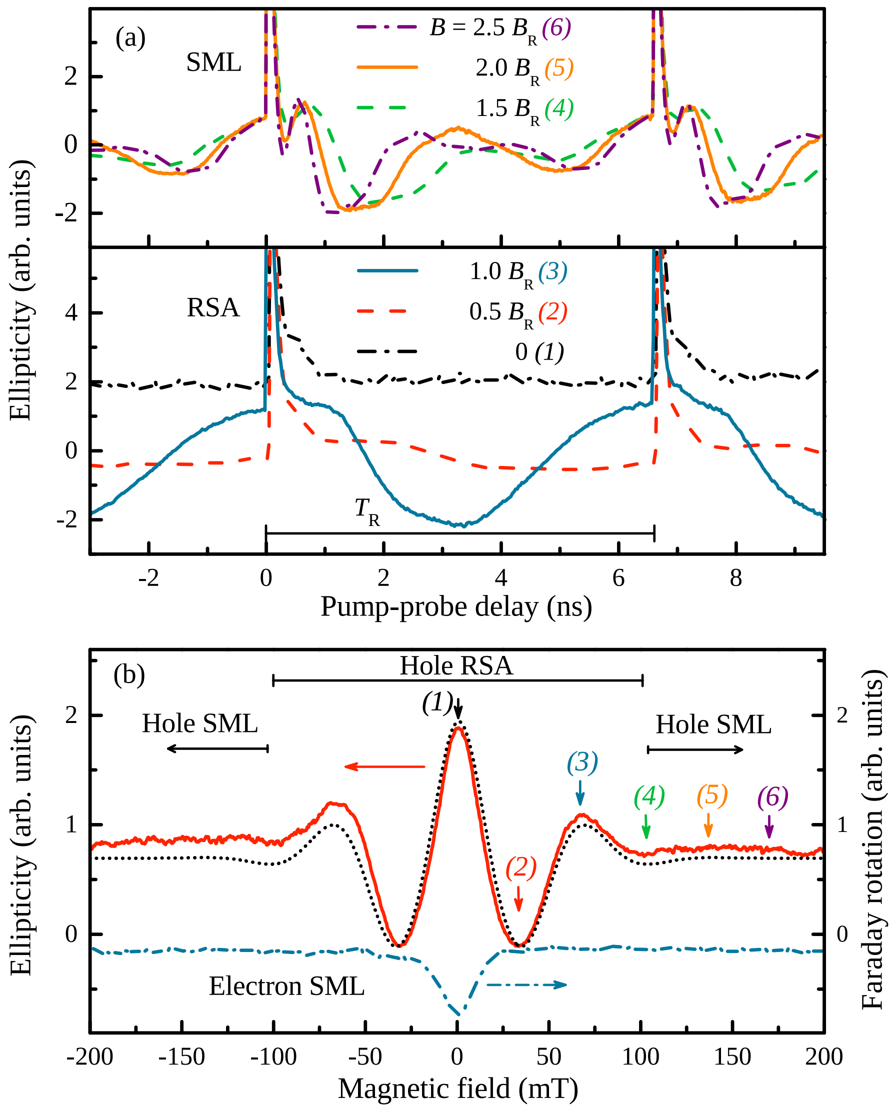

Figure 5.6 **(a)** Hole-spin ensemble precessions at different magnetic fields below 200 mT. The field strengths are given in multiples of the characteristic field $B_\mathrm{R} = (2\pi\hbar)/(g_\mathrm{h}\mu_\mathrm{B}T_\mathrm{R}) = 72\,\mathrm{mT}$, at which the hole spins perform one precessional evolution during the pump-pulse repetition period of $T_\mathrm{R} = 6.6\,\mathrm{ns}$. The numbers in parentheses refer to the arrow positions in panel (b). The three lower curves correspond to the RSA regime, where the ellipticity amplitude around pump incidence depends on the magnetic field. The three upper curves correspond to the SML regime, where this amplitude is equal for all fields. **(b)** Magnetic field dependence of the ellipticity (red solid curve) and Faraday rotation (blue dash-dotted curve) measured at a fixed pump-probe delay shortly before pump incidence. The hole-spin polarization shows a field region of RSA ($|B| < 100\,\mathrm{mT}$) and a region of SML ($|B| > 100\,\mathrm{mT}$), while for the electron-spin polarization only the SML regime is observed. The black dotted curve is a calculation with $|g_\mathrm{h}| = 0.14$, $\Delta g_\mathrm{h} = 0.04$, and $\Theta = 1.4\pi$, performed by I. A. Yugova on the basis of the model presented in [Yug12].

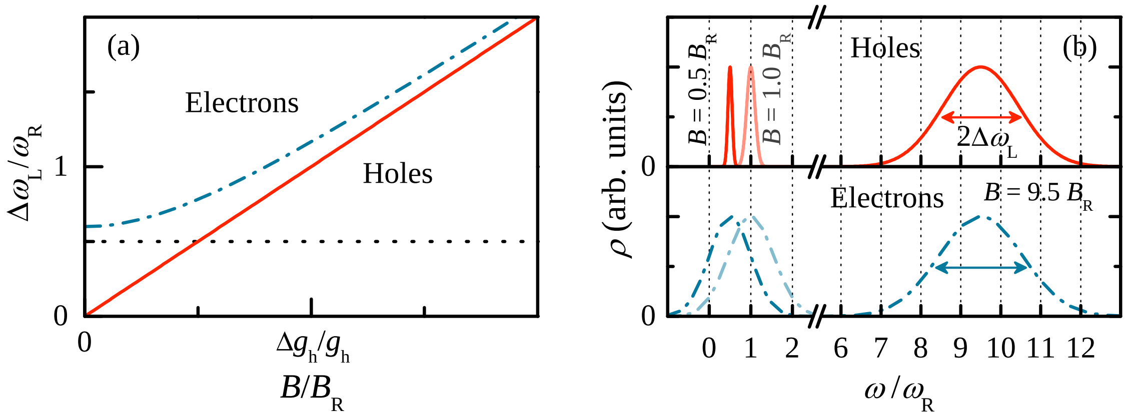

Figure 5.7 (a) Calculated Larmor frequency spread $\Delta\omega_\mathrm{L}$ in dependence on the magnetic field B. The red solid line is $\Delta\omega_\mathrm{L}/\omega_\mathrm{R} = (\Delta g_\mathrm{h}/g_\mathrm{h})(B/B_\mathrm{R})$ in accordance with Eq. (5.4), valid for hole spins. The blue dash-dotted line shows the electron-spin situation with an additional field independent spread $\Delta\omega_\mathrm{n}$, see Eq. (5.5). The black dotted line indicates $\Delta\omega_\mathrm{L} = 0.5\,\omega_\mathrm{R}$. Calculations performed by I. A. Yugova, according to Ref. [Gre09b]. **(b)** Schematic illustration of the precession frequency distribution $\rho(\omega)$ for electrons and holes at different magnetic fields. For holes the distribution width $\Delta\omega_\mathrm{L}$ is so small at low magnetic fields that only at certain field strength ($B \propto \omega_\mathrm{L}$) the PSC can be fulfilled (RSA regime). For electrons the reduction of the width at low magnetic fields is prevented by the nuclei-induced contribution to $\Delta\omega_\mathrm{L}$ so that at least two PSC modes are always covered by the distribution (SML regime).

determined by the g factor spread and decreases linearly with the magnetic field:

$$\Delta\omega_\mathrm{L}^\mathrm{h} = \frac{\Delta g_\mathrm{h}\mu_\mathrm{B}}{\hbar}B\,. \tag{5.4}$$

This is shown by the red, solid line in Fig. 5.7(a). The magnetic field dependence of the ellipticity signal at a small negative pump-probe delay of $\sim 0.1\,\mathrm{ns}$ [shown in the upper red curve in Fig. 5.6(b)] confirms the transition from the RSA to the SML regime with increasing field. In the range of $|B| < 100\,\mathrm{mT}$, the RSA regime can be identified by the signal peaks at $B = \pm B_\mathrm{R} = \pm 72\,\mathrm{mT}$. At these magnetic fields, all hole-spins in the excited ensemble of positively charged QDs are in a single-mode precession. At $B = \pm 0.5\,B_\mathrm{R}$ no hole spin in the ensemble can satisfy the PSC and the signal is in a minimum close to zero. In the higher field range of $|B| > 100\,\mathrm{mT}$, the ellipticity signal is constant and does not depend on the field strength, a consequence of the SML. In the SML regime, for every field strength some modes, but not all, satisfy the PSC. Therefore, the time-resolved ensemble precession signal is in a maximum shortly before pump-incidence [see the upper curves in Fig. 5.6(a)], but not as high as in the case of single-mode precession at $B = \pm B_\mathrm{R}$ [blue, solid curve in Fig. 5.6(a) and blue arrow (3) in Fig. 5.6(b)].

In contrast, the transition to the RSA regime (and a pure single-mode precession [Gre09b]) is not possible for electrons, as demonstrated by the blue, dash-dotted curve in Fig. 5.6(b). No typical RSA peaks can be seen here.[2] The reason for that is the additional, nuclei-induced contribution $\Delta\omega_{\mathrm{L,n}} = g_{\mathrm{e}}\mu_{\mathrm{B}}\Delta B_{\mathrm{n}}/\hbar \gtrsim 0.5\omega_{\mathrm{R}}$ to the spread of Larmor precession frequencies [Gre09b, Yug12]

$$\Delta\omega_{\mathrm{L}}^{\mathrm{e}} = \sqrt{\left(\frac{\Delta g_{\mathrm{e}}\mu_{\mathrm{B}}}{\hbar}B\right)^2 + (\Delta\omega_{\mathrm{L,n}})^2}\,, \tag{5.5}$$

which prevents a reduction of the frequency spread below the RSA threshold, even at low external magnetic fields. The frequency spread for electrons is depicted by the blue, dash-dotted line in Fig. 5.7(a). Panel (b) of Fig. 5.7 schematically illustrates the precession frequency distributions both for electrons and holes at different magnetic fields.

5.2 Hole-spin coherence time

The detection of hole-spin mode-locking offers a possibility to determine the coherence time T_2 by measuring the spin polarization shortly before a pump pulse in dependence on the pump-pulse repetition period T_{R}. According to Eq. (2.24), it is supposed to decay exponentially with T_2 as time constant when T_{R} is increased. In the SML regime, the spin polarization before a pump pulse $S_z^{t\to 0^-}$ and the measured decay time also depend on the pulse area Θ. The maximum coherence time is obtained for $\Theta = \pi$ [Gre06b]. The maximum polarization, however, is obtained for $\pi < \Theta < 2\pi$ [Yug12]. This is because π pulses can synchronize a broader distribution of precession modes, also those which negatively contribute to $S_z^{t\to 0^-}$, e. g., those with $\omega = (N+1/2)\omega_{\mathrm{R}}$ [Gre06b]. Therefore, it is nontrivial to find the corresponding laser power for a π pulse, which needs to be done first.

It can be obtained by measuring the ellipticity amplitude before pump incidence $\varepsilon_0^{\Delta t\to 0^-}$ for different pump-beam powers P_{Pu}. The following equation describes the dependence of the mode-locked spin-ensemble polarization before pump incidence on the pulse area and the pump-pulse separation at a given coherence time [Yug12]:

$$S_z^{t\to 0^-}(\Theta, T_{\mathrm{R}}) = \frac{1-\cos(\frac{\Theta}{2})}{1+\cos(\frac{\Theta}{2})}\left(1 - \sqrt{\frac{\cos^2(\frac{\Theta}{2})\,\mathrm{e}^{-2\frac{T_{\mathrm{R}}}{T_2}} - 1}{0.25[1+\cos^2(\frac{\Theta}{2})]^2\,\mathrm{e}^{-2\frac{T_{\mathrm{R}}}{T_2}} - 1}}\right). \tag{5.6}$$

---

[2] The peak at zero magnetic field (note that the Faraday rotation is negative in this plot) is due to the fact that all spins can be efficiently pumped here, not only those satisfying the PSC at finite fields. Although the spin polarization is subject to dephasing due to precessions about randomly oriented nuclear fields, the measured spin polarization S_z does not vanish completely, because these fields have a finite z component about which the z components of the electron spins do not precess.

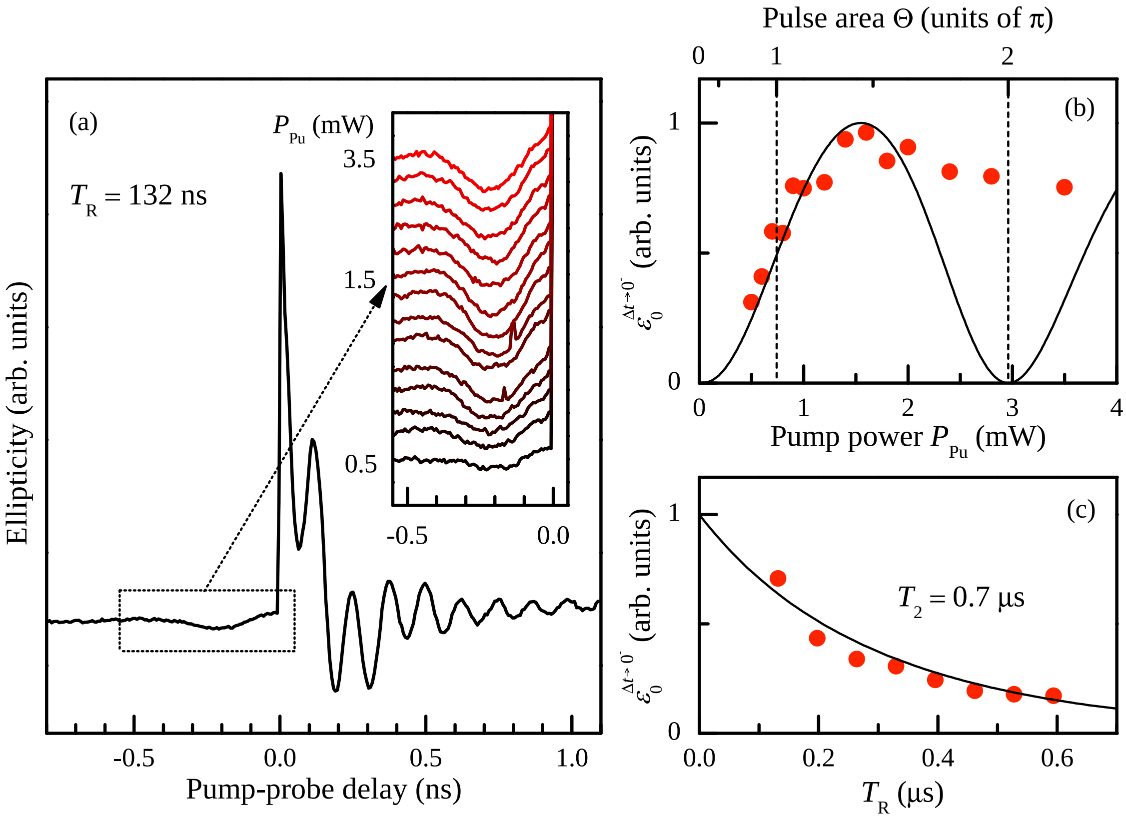

Figure 5.8 **(a)** Time-resolved ellipticity measurements at $B = 1\,\mathrm{T}$ and $T_\mathrm{R} = 132\,\mathrm{ns}$. The inset shows the signal of the last 0.5 ns before pump incidence for different pump-beam powers P_Pu between 0.5 and 3.5 mW. **(b)** Normalized ellipticity amplitude $\varepsilon_0^{\Delta t\to 0^-}$, determined from the data in panel (a), in dependence of P_Pu. A fit to the data with Eq. (5.6) provides the power $P_\mathrm{Pu}^\pi = 0.74\,\mathrm{mW}$ corresponding to $\Theta = \pi$. **(c)** Normalized ellipticity amplitude $\varepsilon_0^{\Delta t\to 0^-}$ in dependence on T_R. The fit with Eq. (5.6) provides a hole-spin coherence time of $T_2 = 0.7\,\mu\mathrm{s}$ at $B = 2\,\mathrm{T}$ and $T \approx 6\,\mathrm{K}$.

The relation between pulse area and pump-beam power P_Pu can be expressed as $\Theta = \sqrt{rP_\mathrm{Pu}}$ so that a fit to the data provides the desired value for the fitting parameter r.[3]

The experiments were performed with a degenerate single-pump-probe setup, extended by the pulse picker as described in Sec. 3.2.1. The minimum pump-pulse (and probe-pulse) separation was thereby limited to 132 ns. At this pulse separation, time-resolved ellipticity measurements of the hole-spin polarization before pump incidence were performed for different pump-beam powers between 0.5 and 3.5 mW. The results are presented in Fig. 5.8(a). The signal amplitudes $\varepsilon_0^{\Delta t\to 0^-}$ ob-

---

[3] Equation (5.6) also contains T_2 as an unknown parameter, which has to be estimated in several preliminary T_R-dependent measurements using different values for P_Pu.

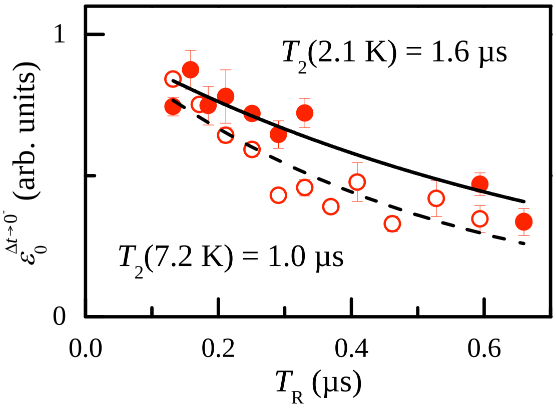

Figure 5.9 Normalized ellipticity amplitudes at negative delays $\varepsilon_0^{\Delta t \to 0^-}$ depending on the pulse separation T_R for two temperatures $T = 2.1\,\mathrm{K}$ (solid circles) and $T = 7.2\,\mathrm{K}$ (open circles) at $B = 1\,\mathrm{T}$. Fits with Eq. (5.7) provide the corresponding coherence times $T_2(2.1\,\mathrm{K}) = 1.6\,\mu\mathrm{s}$ and $T_2(7.2\,\mathrm{K}) = 1.0\,\mu\mathrm{s}$.

tained by fits according to Eq. (5.1) are plotted against P_{Pu} in Fig. 5.8(b). At first, the amplitude increases with power until a maximum is reached for $\sim 1.5\,\mathrm{mW}$. After that the amplitude slightly decreases and tends to saturate, which is interpreted as a strong damping of the expected Rabi-like oscillation due to QD inhomogeneities of the effective pulse area and dipole moments [Bor02]. Therefore, only the rising part of the data is fitted with Eq. (5.6) using a global scaling factor $k = \varepsilon_0^{\Delta t \to 0^-}/S_z^{t \to 0^-}$ and the measured ellipticity amplitude as additional fitting parameter. The parameter r is found to be $r = 13.3\,\mathrm{mW}^{-1}$ so that the pump power corresponding to a π pulse is $P_{\mathrm{Pu}}^{\pi} = 0.74\,\mathrm{mW}$.

With that pump power, a series of pump-probe ellipticity measurements was performed successively increasing the pulse separation T_R. The obtained signal amplitudes at negative delays are plotted in dependence on T_R, see Fig. 5.8(c). The fit with Eq. (5.6) (and again the global scaling factor k) provides a hole-spin coherence time of $T_2 = 0.7\,\mu\mathrm{s}$ at a magnetic field of $B = 2\,\mathrm{T}$ and a temperature of $T \approx 6\,\mathrm{K}$. This value of $T_2 = 0.7\,\mu\mathrm{s}$ is on the same order of magnitude (even slightly below) as the coherence time of $T_2^{\mathrm{e}} = 3\,\mu\mathrm{s}$ for electrons in similar QD structures [Gre06b]. This is unexpected since the hyperfine interaction, which is the main source for electron-spin decoherence at cryogenic temperatures [Mer02, Kha02], is reduced by an order of magnitude for hole spins, see the previous Sec. 5.1 and Refs. [Fal10, Che11].

5.2.1 Temperature dependence

To get more insight into the mechanisms, which are responsible for hole-spin decoherence, it might be helpful to study the temperature dependence of the hole-spin coherence time. This was done using three different experimental techniques.

As long as $T_2 \gtrsim 100\,\mathrm{ns}$, the procedure of measuring T_2 works as described above, successively increasing T_R and measuring the ellipticity SML amplitude at negative time delays $\varepsilon_0^{\Delta t \to 0^-}$. Such measurements were performed for different temperatures between 2 and 11 K at $B = 1\,\mathrm{T}$. For each temperature the SML amplitudes were

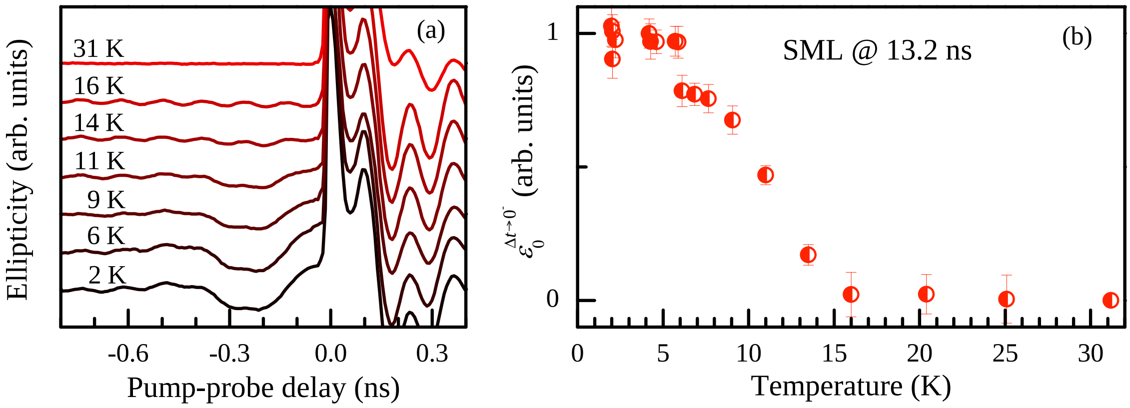

Figure 5.10 **(a)**Time-resolved ellipticity measurements with focus on the negative time delays for different temperatures at $B = 1\,\mathrm{T}$. The pulse separation is fixed at $T_\mathrm{R} = 13.2\,\mathrm{ns}$. Fits to the hole-spin contributions of the signal oscillations provide the SML amplitudes $\varepsilon_0^{\Delta t\to 0^-}$ in panel (b). **(b)** Temperature dependence of the (normalized) hole SML amplitudes, 13.2 ns after the previous pump pulse.

plotted against T_R and fitted by

$$\varepsilon_0^{\Delta t\to 0^-}(T_\mathrm{R}) = A\exp\left[-\left(2+\frac{1}{2\sqrt{3}+3}\right)\frac{T_R}{T_2}\right]. \tag{5.7}$$

to obtain T_2. This fitting function is an approximation of Eq. (5.6) for $\Theta = \pi$ and was derived in the supporting online material of Ref. [Gre06b]. Within the measurement uncertainty, both functions provide the same results. Two data sets, for $T = 2.1\,\mathrm{K}$ and $T = 7.2\,\mathrm{K}$, are shown as an example in Fig. 5.9. The obtained coherence times are $T_2(2.1\,\mathrm{K}) = 1.6\,\mu\mathrm{s}$ and $T_2(7.2\,\mathrm{K}) = 1.0\,\mu\mathrm{s}$. The deviation of these values from the one obtained above [see Fig. 5.8(c)] is due to its assigned temperature of $T \approx 6\,\mathrm{K}$. This temperature is approximate as it was measured in the variable temperature inset of the cryostat, but not in the direct vicinity of the sample. Most probably the temperature at the sample was a few kelvin higher here. During all measurements of the coherence time in dependence on the temperature, the latter was measured by means of a zirconium-oxynitride thin-film thermal sensor mounted directly onto the sample holder. The remaining results of the measurements with various pulse separations are plotted below in Fig. 5.13, together with two other data points of $T_2(T)$ deduced from experiments described in the following.

Due to technical limitations of the pulse picker, it is not possible to reduce the pump- and probe-pulse separation below 132 ns without losing efficiency at larger separations. Therefore, the method of measuring T_2 used so far could not be used for temperatures above 11 K, where the coherence time drops below 100 ns. However, the hole-spin coherence time can here be estimated from the temperature dependence of spectroscopic quantities such as the SML amplitude $\varepsilon_0^{\Delta t\to 0^-}$. For this purpose,

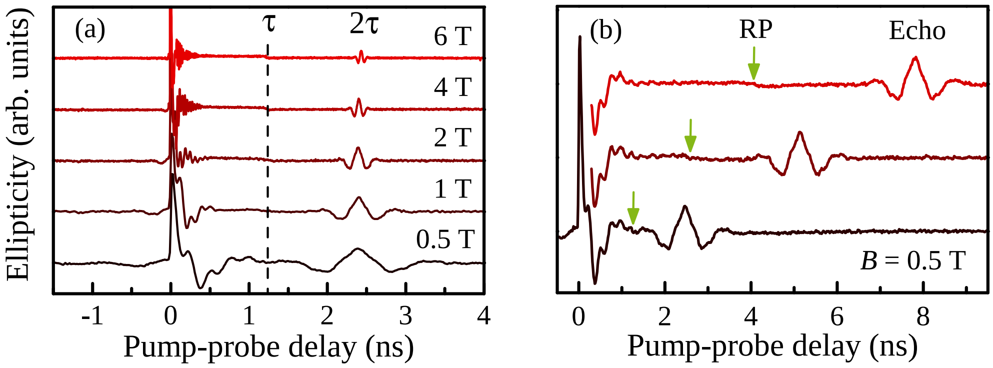

Figure 5.11 **(a)** Hole-spin echoes at different magnetic fields with RP incidence at $\tau = 1.2\,\mathrm{ns}$. **(b)** Hole-spin echoes for different RP delays $\tau = 1.2$, 2.6, and 3.9 ns at $B = 0.5\,\mathrm{T}$. The echo appearance time 2τ shifts in accordance with the RP incidence.

a simple pump-probe setup without pulse picker was used to monitor the SML amplitudes for different temperatures at the fixed pulse separation of $T_{\mathrm{R}} = 13.2\,\mathrm{ns}$. The results are given in Fig. 5.10(a). Only at low temperatures $T \lesssim 14\,\mathrm{K}$ a hole-spin contribution to the ellipticity SML signal at negative delays can be observed. At higher temperatures the signal consists solely of the higher-frequency contributions assigned to electron spins, which also vanish at $T \gtrsim 30\,\mathrm{K}$. These signals are fitted by the sum of two Gaussian-damped oscillating functions with different Larmor frequencies. The hole SML amplitude is extracted and plotted in Fig. 5.10(b). The amplitude drops from maximum to zero between 5 and 15 K because the coherence time has become comparable to or shorter than the pulse separation of 13.2 ns for these temperatures. Hence, one can estimate that the hole-spin coherence time has to be around 7 ns at $T = 15\,\mathrm{K}$. The corresponding data point is inscribed in Fig. 5.13 by the vertically halved red circle.

For even higher temperatures another data point in the temperature dependence of T_2 can be obtained from the temperature dependence of a coherent hole-spin echo emerging in between two pump pulses. Such echoes can be induced by means of additional 2π pulses, which rotate the hole spins by $\Phi = \pi$ about the optical axis and invert the ensemble dephasing process, just as it works for electron spins (see Sec. 2.3.2). However, optically induced hole-spin echoes have not been observed in QD ensembles so far. To provide the additional train of rotation pulses (RP), the setup is extended by an additional pulsed laser system, whose repetition rate is synchronized to the pump-probe laser oscillator (see Sec. 4.1 for the rotation experiments on electron spins). Pulse duration and spectral width are also equal for the two lasers. The pulse area is set to be $\Theta_{\mathrm{RP}} = 2\pi$ in order not to populate trion states, but to remain in the spin subspace of resident holes. The RP photon energy is here, in contrast to the experiments in Sec. 4.1, in resonance with the trion transition addressed by the pump-probe laser to achieve a rotation angle of $\Phi = \pi$.

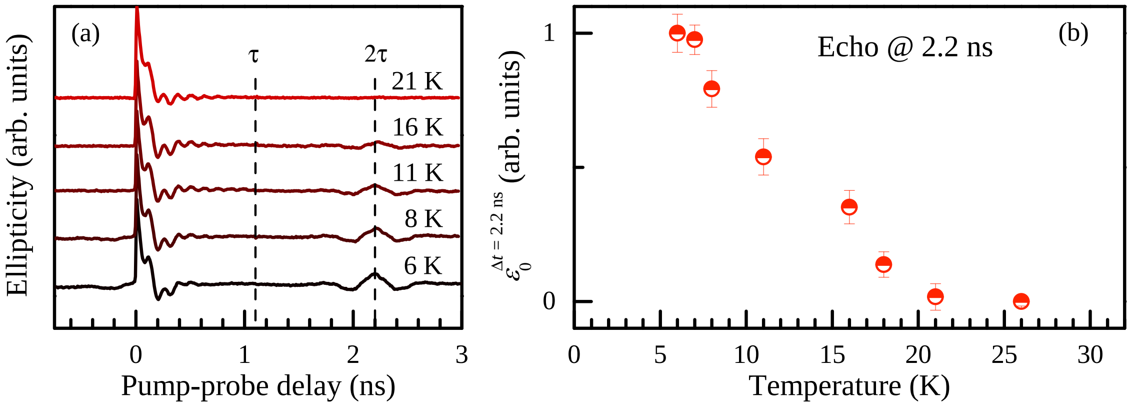

Figure 5.12 Hole-spin echoes recorded for different temperatures at $B = 1\,\mathrm{T}$ and $T_\mathrm{R} = 13.2\,\mathrm{ns}$. RPs are applied at $\tau = 1.1\,\mathrm{ns}$. The echo amplitudes $\varepsilon_0^{\Delta t=2.2\,\mathrm{ns}}$ provide the data points in panel (b). **(b)** Temperature dependence of the (normalized) hole-spin echo amplitudes at a pump-probe delay of 2.2 ns.

Figure 5.11(a) shows such hole-spin echoes induced by the application of RPs at a fixed time delay τ after pump incidence for different magnetic fields. At this delay the hole-spin polarization has completely dephased, but as the individual spins in the ensemble are all rotated by π about the optical axis, the ensemble rephases on the same timescale and an echo of the spin polarization consequently appears at a delay of 2τ. This relation is also demonstrated in Fig. 5.11(b), where the RP delay is shifted with respect to the pump incidence. The shift of the echo appearance is twice the RP shift. The precession frequencies within the echo signal match the hole g factor of 0.14.

A temperature dependence of hole-spin echoes is given in Fig. 5.12. Panel (a) shows time-resolved ellipticity measurements of echoes appearing at $2\tau = 2.2\,\mathrm{ns}$ for different temperatures between 6 and 21 K. The echo signal amplitudes are plotted against the corresponding temperatures in Fig. 5.12(b). Similar to the temperature dependence of the SML amplitude in Fig. 5.10(a), the amplitude decreases with higher temperatures. It drops to zero at $\sim 20\,\mathrm{K}$ due to the loss of coherence. Hence, the coherence time is estimated to be around 1 ns at this temperature. This data point is added to the temperature dependence of T_2 in Fig. 5.13.

For comparison, also data taken from Ref. [Her08] showing the temperature dependence of the electron-spin coherence time in sample # 11955 (see Sec. 3.3) is shown in Fig. 5.13. The maximum of both dependences for holes and electrons is found in the order of a microsecond at low temperatures. For electrons, this value is constant up to about 15 K before it decreases over a 30-K range to a few nanoseconds. This decrease was associated with elastic scattering due to phonon-mediated fluctuations in the hyperfine interaction [Her08]. For holes, the coherence time drops abruptly above a temperature of only 8 K losing almost three orders of magnitude

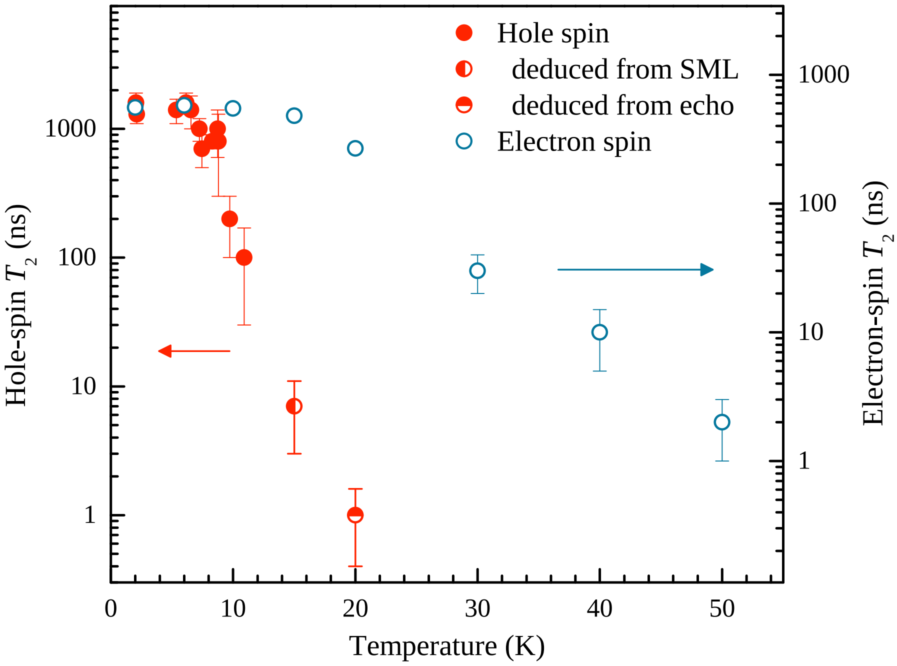

Figure 5.13 Temperature dependence of the coherence time T_2 for hole spins (red circles, left scale) and electron spins (blue circles, right scale). The filled red circles are measured by SML experiments with various pulse separations for different temperatures at $B = 1\,\mathrm{T}$ (see Fig. 5.9). The vertically halved circle is deduced from the temperature dependence of the SML amplitude $\varepsilon_0^{\Delta t \to 0^-}$ with $T_\mathrm{R} = 13.2\,\mathrm{ns}$ (see Fig. 5.10). The horizontally halved circle is deduced from the temperature dependence of the hole-spin echo (see Fig. 5.12). The electron data are taken from Ref. [Her08], being measured at $B = 2\,\mathrm{T}$. They are valid for comparison as from 1 T up to 3 T no magnetic-field dependence was observed.

within $\sim$ 10 K. The reasons for this fast drop, compared to the slower decrease for electrons, as well as the limitation of the hole-spin coherence time to about a microsecond at low temperatures are yet unexplained.

Possible decoherence mechanisms are based either on hyperfine or on spin-orbit related interactions. The Fermi-contact interaction is not relevant for holes, but it was theoretically shown in Ref. [Fis08] that the dipole-dipole interaction or the nuclear interaction with the orbital angular momentum may play an important role. They might be of comparable strength as the Fermi-contact interaction for electrons. Experimental indications for that are given in Ref. [Tes09]. However, in Sec. 5.1 and in other studies it was demonstrated that in (In,Ga)As/GaAs QD structures the hyperfine interaction for holes is at least an order of magnitude weaker than for electrons [Ebl09, Fal10, Che11, DeG11, Fra12b, Wan12]. Therefore, it seems to be unlikely that the hyperfine interaction is responsible for the limitation of the hole-spin coherence time to a microsecond and its faster drop with increasing temperature compared to the electron-spin coherence time.

Disregarding the hyperfine interactions, the spin-orbit coupling might account for the observed hole-spin coherence times and their temperature dependence. Responsible transitions between involved spin levels might be mediated by phonons. Based on that, theoretical models predicted longitudinal spin relaxation times T_1 of hundreds of microseconds at $B = 2\,\mathrm{T}$ and cryogenic temperatures [Lü05, Tri09]. Recent experiments, however, measured T_1 times of only a few microseconds at the same experimental conditions [Fra12a] so that a much stronger spin-orbit coupling might need to be assumed.

This would also affect the transverse relaxation or coherence time T_2. The coherence can be lost when the hole is excited into a higher state, where the effective g factor determined by the energy gap is different. The temporarily altered precession frequency leads to a phase change of the spin precession after relaxation, even when the transitions happen without spin flip [Sem07]. This mechanism was described for electrons, but it is obviously also relevant for holes, not least in case of a stronger spin-orbit coupling. It remains to be explained what process activates these transitions. At the low temperature scale ($T \sim 10\,\mathrm{K}$) at which the drop of T_2 sets in, the thermal energy is about 1 meV. However, the splitting of the corresponding valence band states is estimated to be at least 5 meV.[4] Hence, thermal excitation of holes is not possible. Two-phonon scattering processes are also very unlikely to explain the strong temperature dependence of elastic spin scattering.

An alternative possibility is offered by the interaction between charge carriers and phonons forming a *polaron*, a bound state of the injected charges and a phonon population. The pulsed carrier excitation on a picosecond timescale leads to a distortion of the lattice and to the emission of a phonon wave package escaping on the same timescale. In the spectral domain, this results in broad flanks of the zero-phonon line of the excitonic transition [Bor01, Vag02]. This mechanism is, e. g., a source for decoherence of the exciton polarization after pulsed excitation [Tsi02]. It can also reduce the laser threshold of QDs embedded in an optical resonator, because the phonon sidebands allow the decay of excitons, whose energies do not match a resonator mode [Hen07, Pre07, Kan08, Ate09, Win09]. In that way the continuum of interaction energies offered by the phonon sidebands could also increase the efficiency of elastic two-phonon scattering processes, which in the end destroy the phase coherence of the hole spin. This might explain the coherence time limitation to a microsecond at low temperatures and the drop starting at 8 K, where acoustic phonon modes can thermally be activated as they are within the phonon sidebands. However, still more spectroscopic studies on the hole-spin relaxation mechanisms need to be performed to test these assumptions.

---

[4] This value is based on the splitting between the emissions of the first excited and the QD ground state of 20 meV obtained from PL measurements under pulsed excitation, and the findings in Ref. [Zib05]. Thermal escape of carriers out of the QD confinement potential is also neglected at the studied temperature scale since the PL ground state emission intensity is constant.

5.3 Dynamical decoupling

Concerning quantum information processing, the possible advantages of electron- and hole-spin ensembles embedded in solid state materials, such as robustness, scalability and connection to "classical" information processing hardware [Llo93, Bur00], are on the other hand accompanied by the coupling of the spins to the environment (e. g., nuclear spins, phonons), which is the main source for their decoherence. A way to decouple the spins from surrounding baths is to apply specific pulse sequences which flip the spins and average the bath coupling to zero [Yan11]. An example is the *Carr-Purcell-Meiboom-Gill* (CPMG) protocol suggested already in 1958 [Mei58]. Several improved decoupling protocols have been developed recently, most of which are based on electronically controlled microwave pulses with durations on the nanosecond scale [Uhr07, Lee08, Du09, Sou12]. Thereby the coherence time of electron spins in gate-defined QDs, e. g., could be enhanced from a few to 200 µs [Blu10]. Due to the limitations in varying the pulse properties, optical pulses have not yet been implemented for decoupling protocols. However, such pulses with durations on the picosecond scale are supposed to improve the performance of dynamical decoupling protocols, since they allow shorter pulse intervals to suppress coupling mechanisms with a shorter characteristic timescale and larger coupling constant. Higher pulse rates can cover a broader range of frequencies blocked for the coupling of the spin system to its environment.

The feasibility of an all-optical dynamical decoupling protocol is presented in this section, which uses optically induced hole-spin echoes as introduced in Sec. 5.2.1 (see also Sec. 2.3.2). The idea is to perform multiple π rotations, which invert the inhomogeneous dephasing of the ensemble spin polarization in between two pump pulses. For that purpose the pump- and probe-pulse separation is again increased by the pulse picker (see Sec. 5.2). It picks every nth pulse and blocks all the others such that the pump- and probe-pulse period T_R is a multiple of the intrinsic laser repetition period of 13.2 ns. It is varied from 132 to 462 ns in these experiments. The QD sample is the same as in the previous sections, # 11376 (see Sec. 3.3). The upper trace (black) in Fig. 5.14(a) shows a time-resolved ellipticity measurement of the spin polarization around the pump incidence at zero pump-probe delay. After this incidence spin precessions of resident holes and photo-created electrons (with a higher precession frequency) can be observed. The number of observable hole spin oscillations is small due to fast inhomogeneous dephasing, which results from large g-factor variations in the ensemble (see Sec. 5.1). The decay of electron-spin precessions is mainly due to radiative trion recombination. The oscillation shortly before pump incidence, at negative delays, results from mode-locked resident hole spins (see Sec. 5.1).

To obtain spin echoes, an additional pulsed Ti:Sapphire laser that is used for optical spin rotations as in the experiments described in previous sections is added to the setup. The laser photon energy and pulse duration are identical to the pump-

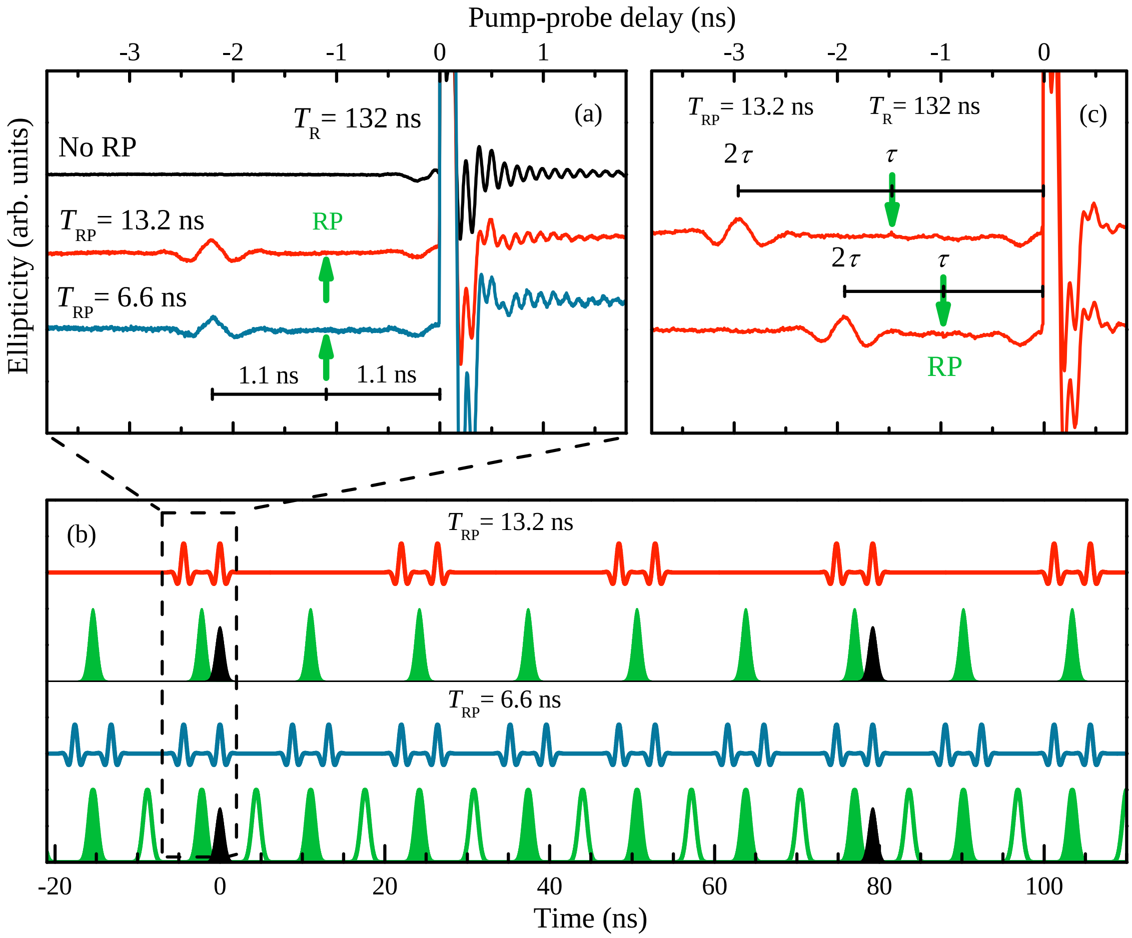

Figure 5.14 **(a)** Time-resolved ellipticity measurements at $B = 1\,\mathrm{T}$ with a pump-probe repetition period of $T_\mathrm{R} = 132\,\mathrm{ns}$. The top trace (black) shows the spin polarization around the pump incidence at zero delay without applying rotation pulses (RP). The middle trace (red) shows such a measurement with additional RP applied 1.1 ns before pump incidence (green arrow) with an RP period of $T_\mathrm{RP} = 13.2\,\mathrm{ns}$. A hole spin echo can be observed 2.2 ns before (or 129.8 ns after previous) pump incidence. In the lower trace (blue) the RP period is reduced to $T_\mathrm{RP} = 6.6\,\mathrm{ns}$ so that the number of rotations between two pump pulses is doubled. **(b)** Scheme of RP pulses (green; filled for $T_\mathrm{RP} = 13.2\,\mathrm{ns}$, outlined for $T_\mathrm{RP} = 6.6\,\mathrm{ns}$) and corresponding echo appearances (red and blue) between two pump pulses (black; $T_\mathrm{R} = 79.2\,\mathrm{ns}$). **(c)** Hole-spin echo emergence at delay 2τ for two different RP arrival times $\tau = -1.5\,\mathrm{ns}$ and $\tau = -1.0\,\mathrm{ns}$, indicated by the green arrows.

probe laser. However, the pulse period is not elongated so that the rotation pulses (RP) are separated by $T_{\mathrm{RP}} = 13.2\,\mathrm{ns}$ at this stage of the experiment. The power is adjusted to a pulse area of $\Theta_{\mathrm{RP}} = 2\pi$ in order to perform a Rabi-flops, which correspond to rotations about the optical axis by an angle of π for the given resonant condition (see Sec. 2.3.2). As a reminder, in an ensemble of dephasing spins, the incidence of such rotation pulses leads to echoes of the overall spin polarization, because the spin ensemble rephases after the single spins are rotated by an angle of π. These echoes appear at a time 2τ, when τ is the time of the RP incidence after the spin ensemble was fully aligned before. This alignment can be the pump-pulse orientation, but also a previous echo. Since $T_{\mathrm{RP}} \ll T_{\mathrm{R}}$ in this experiment, the spins are rotated multiple times between two pump pulses. This leads to a sequence of dephasing, rephasing, and the formation of multiple echoes between two pump pulses.

The RP and echo sequences between two subsequent pump pulses are schematically illustrated in Fig. 5.14(b). The upper part shows the case in which the RP separation is 13.2 ns, as depicted by the filled green pulses. For reasons of clarity, the separation between the black colored pump pulses is assumed to be $T_R = 79.2\,\mathrm{ns}$, much smaller than the minimum separation used in the experiment. The upper red trace shows the expected echo sequence as a result of the RP application. After pump incidence at $\Delta t = 0$ the first RP hits at 12.1 ns, leading to the formation of an echo at 24.2 ns. The next RP arrives 1.1 ns later at $\Delta t = 25.3\,\mathrm{ns}$ and inverts the spin dephasing, which started after the previous echo, so that it induces another echo further 1.1 ns later at 26.4 ns. The situation at this point in time is comparable to the moment of pump pulse application and subsequent RPs induce identical echo sequences. It is worth to be noted that due to the particular periodicity of RP and pump pulses, the appearance condition for echoes is symmetric in time: when the RP incidence is at τ, the echo appearance is at 2τ, independent on the sign of τ. This is confirmed by the measurement results in Fig. 5.14(c), where the echo emergence at 2τ is shown for two different moments of RP arrival τ. When changing τ from $-1\,\mathrm{ns}$ to $-1.5\,\mathrm{ns}$, the echo at 2τ shifts correspondingly from $-2\,\mathrm{ns}$ to $-3\,\mathrm{ns}$.

The length of the mechanical delay stage for adjusting the different pulse trains relative to each other allows to cover a delay range of about 6 ns. It is chosen to cover the range from about $-4\,\mathrm{ns}$ to 2 ns so that the pump incidence and the last echo before can be monitored, when the RP arrival is shortly before pump incidence. This is demonstrated by the middle, red trace in Fig. 5.14(a). The RP delay relative to the pump incidence is chosen such that a RP appears 1.1 ns before (and, e. g., 12.1 ns after) pump incidence, denoted by the green arrow. Consequently, a hole-spin echo appears 2.2 ns before pump orientation. At the given pump repetition period of $T_{\mathrm{R}} = 132\,\mathrm{ns}$, this is 129.8 ns after previous pump orientation. In comparison with the black reference trace without RP, the amplitude of photocreated electrons at positive delays is slightly reduced. This might be due to the fact that the pump-pulse arrival always coincides with an echo appearance, where, irrespective of the

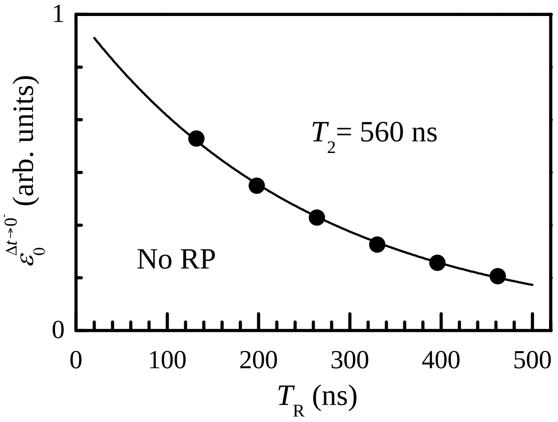

Figure 5.15 Normalized ellipticity amplitudes shortly before pump incidence $\varepsilon_0^{\Delta t\to 0^-}$ depending on the pump-pulse separation T_R without RP application. A fit according to Eq. (5.7) provides a coherence time of $T_2 = 560\,\mathrm{ns}$ at $T = 6\,\mathrm{K}$ and $B = 1\,\mathrm{T}$.

fulfillment of the PSC for mode-locking, the coherent spins are oriented along the initial pump-induced direction so that in this case no new trion excitation can take place.

In the next stage of the experiment, the rotation rate is doubled by another extension to the pump-probe setup. The RP beam is therefore split into two beams of identical power. One part is delayed by 6.6 ns and recombined with the non-delayed one so that the RP arrival period is reduced to $T_\mathrm{RP} = 6.6\,\mathrm{ns}$. The resulting ellipticity measurement is shown in the lower, blue trace in Fig. 5.14(a). The echo appearance is still 2.2 ns before pump incidence, in accordance with the adjusted pulse scheme in the lower part of Fig. 5.14(b). The additional RP train delayed by 6.6 ns is depicted by the outlined green pulses at the bottom. The resulting echo appearance is given by the blue trace above. In the monitored time frame, illustrated by the dashed rectangle around the left pump pulse, the echo appearance pattern is identical.

To determine the coherence time, the pump-probe pulse period T_R is incrementally increased and the amplitudes of the last echo before pump incidence at $2\tau = -2.2\,\mathrm{ns}$ are measured [by fitting the ellipticity traces with Eq. (5.1)] in dependence of the time after previous pump incidence $t = T_\mathrm{R} + 2\tau$. As a reference, also the coherence time without RP application is determined by exploiting the dependence of the signal amplitude of mode-locked hole-spins shortly before pump incidence $\varepsilon_0^{\Delta t\to 0^-}$ on the pump-pulse separation T_R. These amplitudes $\varepsilon_0^{\Delta t\to 0^-}$ are plotted in Fig. 5.15. Except for the absence of RPs, the experimental conditions are equal to the case with RP application. This is decisive because the measured coherence times sensitively depend on the sample temperature and the pump power (see Sec. 5.2). The data are normalized to the ordinate intercept A of an exponential fit according to Eq. (5.7). The coherence time without RP application is determined to be $T_2 = 560\,\mathrm{ns}$. This value is taken as a reference for the decay of $\varepsilon_0^{\Delta t\to 0^-}(T_\mathrm{R})$ in all measurements with RP application to account for possible variations in experimental parameters such as the RP area Θ_RP. Therefore, the amplitudes $\varepsilon_0^{\Delta t\to 0^-}$ are determined in each recorded

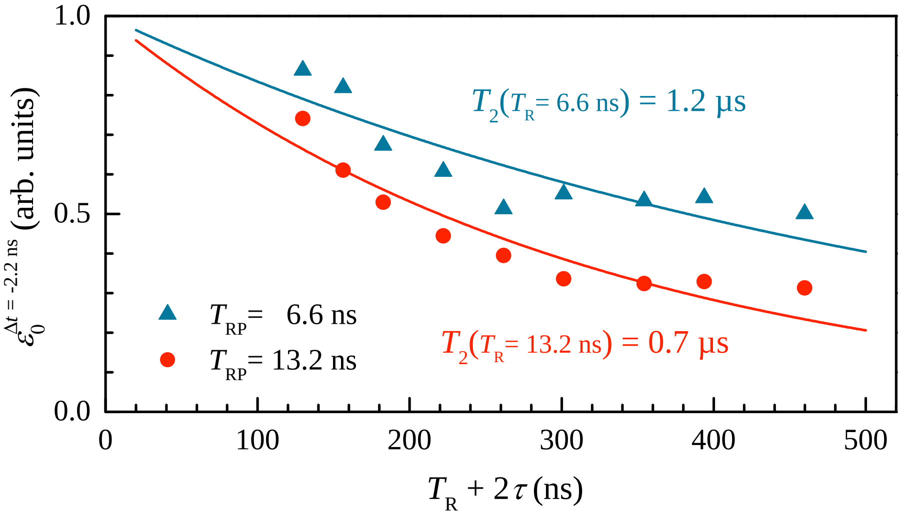

Figure 5.16 Normalized amplitudes of the last echo before pump incidence $\varepsilon_0^{\Delta t=-2.2\,\mathrm{ns}}$ in dependence on the time after previous pump incidence $t = T_\mathrm{R} + 2\tau$, which is determined by the pump-probe repetition period T_R and the RP delay $\tau = -1.1\,\mathrm{ns}$. The red dots show the amplitudes for a RP period of $T_\mathrm{RP} = 13.2\,\mathrm{ns}$ while the blue triangles show the amplitudes for $T_\mathrm{RP} = 6.6\,\mathrm{ns}$. Fits according to Eq. (5.8) provide coherence times of $T_2(T_\mathrm{RP} = 13.2\,\mathrm{ns}) = 0.7\,\mathrm{\mu s}$ and $T_2(T_\mathrm{RP} = 6.6\,\mathrm{ns}) = 1.2\,\mathrm{\mu s}$.

ellipticity trace which is then normalized to the value of $\varepsilon_0^{\Delta t\to 0^-}$ in the corresponding reference trace without RP application.

The echo amplitudes $\varepsilon_0^{\Delta t=-2.2\,\mathrm{ns}}$ are shown in Fig. 5.16 for both RP periods $T_\mathrm{RP} = 13.2\,\mathrm{ns}$ and $T_\mathrm{RP} = 6.6\,\mathrm{ns}$ in dependence of the time after the previous pump incidence $t = T_\mathrm{R} + 2\tau$ with $\tau = -1.1\,\mathrm{ns}$. The dependences are fitted by exponential decay functions similar to Eq. (5.7), but adapted to the temporally shifted measuring point, the echo appearance:

$$\varepsilon_0^{\Delta t=-2.2\,\mathrm{ns}}(T_\mathrm{R}) = A\,\exp\left[-\left(2+\frac{1}{2\sqrt{3}+3}\right)\frac{T_\mathrm{R}+2\tau}{T_2}\right]. \tag{5.8}$$

For both RP periods, the amplitudes decrease with increasing T_R due to the loss of coherence, but the decay with RP application does not seem to be purely exponential anymore. In comparison with the exponential fit functions, the amplitudes drop faster at the beginning followed by a much slower decrease at the end. However, the decay is clearly faster for $T_\mathrm{RP} = 13.2\,\mathrm{ns}$ and slower for $T_\mathrm{RP} = 6.6\,\mathrm{ns}$. In the first case, the fit provides a hole-spin coherence time of $T_2(T_\mathrm{RP} = 13.2\,\mathrm{ns}) = 0.7\,\mathrm{\mu s}$. When the RP rate is doubled, the coherence time increases to $T_2(T_\mathrm{RP} = 6.6\,\mathrm{ns}) = 1.2\,\mathrm{\mu s}$. These values are both larger than the reference value without RP application (see Fig. 5.15); in the case of $T_\mathrm{RP} = 6.6\,\mathrm{ns}$ it has increased by more than a factor of two. If only the data points beyond 200 ns were considered, decay times of about ten microseconds would be obtained.

These results indicate that the spins are dynamically decoupled from surrounding baths by the recurrent spin inversion so that the decoherence mechanisms are suppressed. The potential of an all-optical dynamical decoupling protocol with RP sequences is demonstrated. However, further work needs to be done to understand the nonexponential decay. This might go hand in hand with the investigations on the hole-spin decoherence mechanisms, which are still unclear as well (see Sec. 5.2.1). The understanding of one aspect might help to obtain new insights into the other aspect. The dynamical decoupling protocol could be adapted such that RP and pump arrival coincide. Thus, the number of rotations and echo appearances would be halved as two echoes would coincide with every second RP. Additionally, the experiments could be repeated with an n-doped QD sample to test the effects on resident electrons.

6 Summary and outlook

In this thesis experimental studies on the optical manipulation of electron and hole spins in (In,Ga)As/GaAs QD ensembles are presented.

In Chap. 4 the feasibility of an all-optical tomography measurement on an ensemble of electron spins is shown. The spin ensemble is periodically oriented by circularly polarized optical pump pulses and precesses in an external magnetic field perpendicular to the optical axis. The spin components in the plane of precession are determined by measuring the polarization of probe pulses transmitted through the QD sample. At a certain phase of the precessional evolution the spins are rotated by additional rotation pulses by an angle of $\pi/2$ about the optical axis so that the former component along the magnetic field is rotated into the precession plane, where it can be measured. By varying the time delay of the rotation pulses the temporal evolution of the spin component along the field is thus obtained. Such a tomography measurement is obligatory with regard to the complete read-out process of the spin information, which is the fifth DiVincenzo criterion for qubit implementation (see Chap. 1). The presented technique is based on optically induced spin rotations by means of picosecond laser pulses. This allows the read-out of all spin-vector components on timescales at least an order of magnitude shorter compared to tomography techniques based on radio-frequency pulses used, e. g., in NMR experiments.

The tomography measurement is performed on a spin subset that is interacting with another subset of spins within the same QD ensemble. Due to this interaction introduced in Refs. [Spa11a, Spa11c] a spin component along the field is expected to build up in time. The time evolution of this component of one subset is measured and confirms the theory predicting this behavior in addition to the findings in the earlier experiments by S. Spatzek. Furthermore, the interaction strength is determined to be $J = 0.05\,\mu\text{eV}$, which is about an order of magnitude smaller than the value found in Refs. [Spa11a, Spa11c], but still coincides with the assumptions concerning the microscopic interaction mechanisms therein. The investigated spin-spin interaction is of particular interest concerning the third DiVincenzo criterion as it could play a role in the implementation of quantum gates. As a next step a tomography measurement of the system of both spin-subsets is desirable. This can technically be achieved by means of two more laser-pulse trains for measuring the spin-vector components of the second subset. Modern broadband fiber-based pulsed laser systems could provide the required laser protocols for the initialization and read-out of interacting spin-ensemble qubits.

In preliminary measurements discussed at the beginning of Chap. 4, the applicability of optically induced rotations is studied with respect to the strength of the external magnetic field. It is found that due to the finite pulse duration and the ensemble inhomogeneity of precession frequencies, clean spin-ensemble rotations can only be achieved at magnetic fields weaker than $B = 0.5\,\mathrm{T}$ under the given sample and laser-pulse conditions.

A third experiment is presented at the end of Chap. 4, in which a pumplike rectification pulse is used to reveal the spin-orientation patterns in a mode-locked electron-spin ensemble. The rectification pulses hit the sample at the same moment as the probe pulses. Exploiting the Pauli blocking, this leads to signal bursts oscillating with higher harmonics of the fundamental Larmor precession frequency at certain pump-probe delays, where the spin ensemble forms well-ordered orientation patterns. The shape of the pattern is reflected by the respective oscillation frequency. Thus, information about the single-spin orientations in a dephased ensemble is provided that might, e. g., help to understand the spin-spin interaction within this ensemble.

Chapter 5 focuses on hole-spin ensembles. In the first part of this chapter experiments are presented that show hole-spin mode-locking, the precession-phase synchronization with the periodical laser-pulse excitation. This phenomenon reduces the precession frequencies contributing to the measured spin polarization to a few discrete modes and provides the opportunity to study the spin coherence of resident holes in an inhomogeneous ensemble of positively charged QDs. The mode-locking regime is shown by experiments with a pump-doublet excitation, which alters the phase synchronization condition. The measured variable is here the ellipticity of the transmitted probe beam. Measuring the Faraday rotation of that probe beam provides an altered signal, which shows spin precessions of resident electrons from negatively charged QDs within the same sample. The reason for the signal change is the different spectral dependences of the two measured variables, Faraday rotation and ellipticity, and the different interactions between the QD nuclei and the two carriers, electrons and holes. The hole-nuclear interaction is found to be much weaker than the electron-nuclear interaction. This becomes apparent by switching from the double to a single pump-pulse protocol, which demonstrates that electron spins are subject to a nuclei induced precession-frequency focusing and hole spins are not. At low magnetic fields the electron-nuclear interaction contributes significantly to the spread of precession frequencies so that even in this case a sufficient number of modes is efficiently pumped to enable spin mode-locking. The reduced hole-nuclear interaction, instead, leads to a narrow frequency spread solely determined by the g factor distribution. Thus, hole spins can enter a regime of resonant spin amplification including pure single-mode precession for fields $B \lesssim 100\,\mathrm{mT}$.

In the second part of Chap. 5 the hole-spin coherence time and especially its temperature dependence is investigated. A long spin-coherence time is a key requirement for qubit implementation, formulated as the fourth DiVincenzo criterion. Exploiting the spin mode-locking effect and spin echoes formed by optically induced spin rotations, the hole-spin coherence time is determined to be about $T_2 = 1\,\mu\mathrm{s}$ at temperatures $T < 8\,\mathrm{K}$. It drops down to a few nanoseconds during a temperature increase of $\sim 10\,\mathrm{K}$. In comparison with the temperature dependence of electron spins in similar QD structures measured by F. G. G. Hernandez, this drop is faster and starts at lower temperatures. The maximum value for low temperatures is about a microsecond for both carriers. Both the maximum value and the faster decrease are unexpected since the interaction with the nuclei, which was found to be the main source for electron-spin decoherence, is much weaker for holes. An alternative hole-spin decoherence mechanism is offered by the broad flanks of the zero-phonon line induced by polarons. They could provide an increase of elastic two-phonon scattering processes, which excite the holes to a higher state where an altered precession frequency leads to decoherence.

Finally, in the last part of Chap. 5, an experiment is presented, in which a sequence of several π rotations inverting the dephasing process and leading to multiple echoes in between two pump pulses is applied to dynamically decouple the spins from their sources of decoherence. The hole-spin coherence is observed by incrementally enlarging the pump-pulse separation and monitoring the signal amplitude of the last echo before a pump incidence. When the rotation rate is doubled by halving the rotation-pulse separation, the decay of this echo amplitude and thus the coherence time is elongated.

However, some questions concerning the decay behavior of the echo amplitude could not be clarified in the latter experiment. This, together with the uncertainty about the hole-spin decoherence mechanisms, requires further investigations. Future studies should aim for an improvement of the dynamical decoupling efficiency, e. g., by adapting the pulse sequence as mentioned at the end of the respective section. A better understanding of the decoupling process might be helpful in the search for the hole-spin decoherence mechanisms. Besides, the decoupling protocol is worth to be transferred to electron spins in QDs. Another approach to hole-spin coherence is provided by special QD samples, where membranes are used to change the sign of the strain in the QDs. Thus, also the sign of the heavy-hole–light-hole splitting is changed so that the ground state is a light-hole state with different g factor properties.

For electron-spin ensembles, the full tomography measurement of the interacting qubit pair needs to be implemented by extending the presented technique to the second spin subset. Then it should be possible to obtain the two-qubit density matrix. Moreover, the spin-spin interaction could be investigated with regard to the initialization of three or even more spin subsets each representing a qubit within the QD ensemble. The interaction should also, though perhaps very weakly, manifest between single spins within one subset and influence the dephasing process, especially at low magnetic fields. It is further certainly sensible to continue and extend optical studies on gated QD samples, where it is possible to change the charge state of the QDs by applying electrical gate voltages. At small voltages,

e. g., photo-excited electrons can be sucked out of the dots, while the holes remain inside. By further increasing the voltage it is possible to charge the dots with a single electron each so that an ensemble can show spin mode-locking under periodical pump excitation. The spin polarization can also be canceled when the voltage is high enough to charge the QDs with two electrons, whose spins compensate each other. The combination of electrical charge control and optical spin manipulation might be advantageous in many aspects as, for example, quantum gate operations and facilitates the introduction of spin qubits into classical information technology.

To summarize, this thesis examines and provides new insights into the optical control, manipulation and read-out of carrier spins in low-dimensional semiconductor nanostructures, which are specifically relevant for possible implementations in quantum information technologies.

Bibliography

[All87] L. Allen, J. H. Eberly: *Optical Resonance and Two-Level Atoms.* Dover Publications Inc., Mineola 1975.

[Alt04] J. B. Altepeter, D. F. V. James, P. G. Kwiat: *Quantum State Tomography.* M. Paris. J. Rehacek (Eds.): *Quantum State Estimation* - Lecture Notes in Physics, 649, 113-146. Springer, Berlin 2004.

[Ate09] S. Ates, S. M. Ulrich, A. Ulhaq, S. Reitzenstein, A. Löffler, S. Höfling, A. Forchel, P. Michler: *Non-resonant dot-cavity coupling and its potential for resonant single-quantum-dot spectroscopy.* Nature Photon. **3**, 724 (2009).

[Bar04] L. D. Barron: *Molecular Light Scattering and Optical Activity.* Cambridge University Press, New York 2004.

[Bar11] E. Barnes, S. E. Economou: *Electron-Nuclear Dynamics in a Quantum Dot under Nonunitary Electron Control.* Phys. Rev. Lett. **107**, 047601 (2011).

[Bel10] T. Belhadj, T. Amand, A. Kunold, C.-M. Simon, T. Kuroda, M. Abbarchi, T. Mano, K. Sakoda, S. Kunz, X. Marie, B. Urbaszek: *Impact of heavy hole-light hole coupling on optical selection rules in GaAs quantum dots.* Appl. Phys. Lett. **97**, 051111 (2010).

[Bes05] B. Beschoten: *Spin coherence in semiconductors.* S. Blügel, T. Brückel, C. M. Schneider: *Magnetism goes Nano* - Reihe Materie und Material, 26, E7.1-E7.27. Forschungszentrum Jülich 2005.

[Blo46] F. Bloch: *Nuclear Induction.* Phys. Rev. **70**, 460 (1946).

[Blu10] H. Bluhm, S. Foletti, I. Neder, M. Rudner, D. Mahalu, V. Umansky, A. Yacoby: *Dephasing time of GaAs electron-spin qubits coupled to a nuclear bath exceeding 200 μs.* Nature Physics **7**, 109 (2011).

[Boc10] C. Bock: *Self-assembled InAs quantum dots in GaAs/AlGaAs.* - `http://www.lwe.ruhr-uni-bochum.de/start\_nano\_en.jsp?page=qdInAs-1` on 03-30-2010, Ruhr-Universität Bochum 2010.

[Bor01] P. Borri, W. Langbein, S. Schneider, U. Woggon, R. L. Sellin, D. Ouyang, D. Bimberg: *Ultralong Dephasing Time in InGaAs Quantum Dots*. Phys. Rev. Lett. **87**, 157401 (2001).

[Bor02] P. Borri, W. Langbein, S. Schneider, U. Woggon, R. L. Sellin, D. Ouyang, D. Bimberg: *Rabi oscillations in the excitonic ground-state transition of InGaAs quantum dots*. Phys. Rev. B **66**, 081306(R) (2002).

[Buc66] A. D. Buckingham, P. J. Stephens: *Magnetic Optical Activity*. Annu. Rev. Phys. Chem. **17**, 399 (1966).

[Bur00] G. Burkard, H.-A. Engel, D. Loss: *Spintronics and Quantum Dots for Quantum Computing and Quantum Communication*. Fortschr. Phys. **48**, 965 (2000).

[Bri05] K.-A. Brickman, P. C. Haljan, P. J. Lee, M. Acton, L. Deslauriers, C. Monroe: *Implementation of Grover's quantum search algorithm in a scalable system*. Phys. Rev. A **72**, 050306(R) (2005).

[Car09] S. G. Carter, A. Shabaev, S. E. Economou, T. A. Kennedy, A. S. Bracker, T. L. Reinecke: *Directing Nuclear Spin Flips in InAs Quantum Dots Using Detuned Optical Pulse Trains*. Phys. Rev. Lett. **102**, 167403 (2009).

[Che11] E. A. Chekhovich, A. B. Krysa, M. S. Skolnick, A. I. Tartakovskii: *Direct Measurement of the Hole-Nuclear Spin Interaction in Single InP/GaInP Quantum Dots Using Photoluminescence Spectroscopy*. Phys. Rev. Lett. **106**, 027402 (2011).

[Chu98] I. L. Chuang, L. M. L. Vandersypen, X. Zhou, D. W. Leung, S. Lloyd: *Experimental realization of a quantum algorithm*. Nature **393**, 143 (1998).

[Cla08] J. Clarke, F. K. Wilhelm: *Superconducting quantum bits*. Nature **453**, 1031 (2008).

[Cro10] S. A. Crooker: *Coherent Spin Dynamics of Carriers and Magnetic Ions in Diluted Magnetic Semiconductors*. J. Kossut, J. A. Gaj (Eds.): *Introduction to the Physics of Diluted Magnetic Semiconductors* - Springer Series in Materials Sciences, 144, 305-334. Springer, Berlin 2010.

[Cus96] M. A. Cusack, P. R. Briddon, and M. Jaros: *Electronic structure of InAs/GaAs self-assembled quantum dots*. Phys. Rev. B **54**, R2300 (1996).

[DeG11] K. De Greve, P. L. McMahon, D. Press, T. D. Ladd, D. Bisping, C. Schneider, M. Kamp, L.Worschech, S. Höfling, A. Forchel, Y. Yamamoto: *Ultrafast coherent control and suppressed nuclear feedback of a single quantum dot hole qubit*. Nat. Phys. **7**, 872 (2011).

[Den02] G. Denninger: *Hyperfine interaction.* - `http://www.uni-stuttgart.de/gkmr/lectures/lectures_WS_0203/GKMR2002.html` on 12-10-2013, University of Stuttgart 2002.

[Dev04] M. H. Devoret, J. M. Martinis: *Implementing Qubits with Superconducting Integrated Circuits.* Quantum Inf. Process. **3** (2004).

[DiC09] L. DiCarlo, J. M. Chow, J. M. Gambetta, L. S. Bishop, B. R. Johnson, D. I. Schuster, J. Majer, A. Blais, L. Frunzio, S. M. Girvin, R. J. Schoelkopf: *Demonstration of two-qubit algorithms with a superconducting quantum processor.* Nature **460**, 240 (2009).

[DiV00] D. P. DiVincenzo: *The Physical Implementation of Quantum Computation.* Fortschr. Phys. **48**, 771 (2000).

[Dol13] F. Dolde, I. Jakobi, B. Naydenov, N. Zhao, S. Pezzagna, C. Trautmann, J. Meijer, P. Neumann, F. Jelezko, J. Wrachtrup: *Room-temperature entanglement between single defect spins in diamond.* Nat. Phys. **9**, 139 (2013).

[Du09] J. Du, X. Rong, N. Zhao, Y. Wang, J. Yang, R. B. Liu: *Preserving electron spin coherence in solids by optimal dynamical decoupling.* Nature **461**, 1265 (2009).

[Dya73] M. I. Dyakonov, V. I. Perel: *Optical orientation in a system of electrons and lattice nuclei in semiconductors. Theory.* Zh. Eksp. Teor. Fiz. **65**, 362 (1973) [Sov. Phys. JETP **38**, 177 (1974)].

[Dya84] M. I. Dyakonov, V. I. Perel: *Theory of Optical Spin Orientation of Electrons and Nuclei in Semiconductors.* F. Meier, B. P. Zakharchenya (Eds.): *Optical Orientation* - Modern problems in condensed matter sciences Volume 8, 11. North-Holland, Amsterdam 1984.

[Dya08] M. I. Dyakonov: *Basics of Semiconductor and Spin Physics.* M. I. Dyakonov (Ed.): *Spin Physics in Semiconductors* - Springer Series in Solid-State Sciences, 157, 1-28. Springer, Berlin 2008.

[Ebl09] B. Eble, C. Testelin, P. Desfonds, F. Bernardot, A. Balocchi, T. Amand, A. Miard, A. Lemaitre, X. Marie, M. Chamarro: *Hole-Nuclear Spin Interaction in Quantum Dots.* Phys. Rev. Lett. **102**, 146601 (2009).

[Eco10] S. E. Economou, T. L. Reinecke: *Optically induced spin rotations in quantum dots.* G. Slavcheva, P. Roussignol (Eds.): *Optical Generation and Control of Quantum Coherence in Semiconductor Nanostructures* - Nanoscience and Technology, 63-83. Springer, Berlin 2010.

[Fal10] P. Fallahi, S. T. Yilmaz, A. Imamoglu: *Measurement of a Heavy-Hole Hyperfine Interaction in InGaAs Quantum Dots Using Resonance Fluorescence.* Phys. Rev. Lett. **105**, 257402 (2010).

[Fey82] R. P. Feynman: *Simulating Physics with Computers.* Int. J. Theor. Phys. **21**, 1896-1899 (1982).

[Fis08] J. Fischer, W. A. Coish, D. V. Bulaev, D. Loss: *Spin decoherence of a heavy hole coupled to nuclear spins in a quantum dot.* Phys. Rev. B **78**, 155329 (2008).

[Fla02] M. E. Flatté, J. M. Byers, W. H. Lau: *Spin Dynamics in Semiconductors.* D. D. Awschalom, D. Loss, N. Samarth (Eds.): *Semiconductor Spintronics and Quantum Computation*, 107-146. Springer, Berlin 2002.

[Fol09] S. Foletti, H. Bluhm, D. Mahalu, V. Umansky, A. Yacoby: *Universal quantum control of two-electron spin quantum bits using dynamic nuclear polarization.* Nat. Phys. **5**, 903 (2009).

[Fra12a] F. Fras, B. Eble, P. Desfonds, F. Bernardot, C. Testelin, M. Chamarro, A. Miard, A. Lemaître: *Two-phonon process and hyperfine interaction limiting slow hole-spin relaxation time in InAs/GaAs quantum dots.* Phys. Rev. B **86**, 045306 (2012).

[Fra12b] F. Fras, B. Eble, B. Siarry, F. Bernardot, A. Miard, A. Lemaître, C. Testelin, M. Chamarro: *Hole spin mode locking and coherent dynamics in a largely inhomogeneous ensemble of p-doped InAs quantum dots.* Phys. Rev. B **86**, 161303(R) (2012).

[Gaj10] J. A. Gaj, J. Kossut: *Basic Consequences of sp-d and d-d Interactions in DMS.* J. Kossut, J. A. Gaj (Eds.): *Introduction to the Physics of Diluted Magnetic Semiconductors* - Springer Series in Materials Sciences, 144, 305-334. Springer, Berlin 2010.

[Gam02] D. Gammon, D. G. Steel: *Optical studies of single quantum dots.* Phys. Today **55**, 36 (2002).

[Gla10] M. M. Glazov, I. A. Yugova, S. Spatzek, A. Schwan, S. Varwig, D. R. Yakovlev, D. Reuter, A. D. Wieck, M. Bayer: *Effect of pump-probe detuning on the Faraday rotation and ellipticity signals of mode-locked spins in (In,Ga)As/GaAs quantum dots.* Phys. Rev. B **82**, 155325 (2010).

[Gla12] M. M. Glazov: *Coherent spin dynamics of electrons and excitons in nanostructures (a review).* Phys. Solid State **54**, 1 (2012).

[Gre06a] A. Greilich, R. Oulton, E. A. Zhukov, I. A. Yugova, D. R. Yakovlev, M. Bayer, A. Shabaev, Al. L. Efros, I. A. Merkulov, V. Stavarache, D. Reuter, A. Wieck: *Optical Control of Spin Coherence in Singly Charged (In,Ga)As/GaAs Quantum Dots*. Phys. Rev. Lett. **96**, 227401 (2006).

[Gre06b] A. Greilich, D. R. Yakovlev, A. Shabaev, Al. L. Efros, I. A. Yugova, R. Oulton, V. Stavarache, D. Reuter, A. Wieck, M. Bayer: *Mode Locking of Electron Spin Coherences in Singly Charged Quantum Dots*. Science **313**, 341-345 (2006).

[Gre07a] A. Greilich: *Spin coherence of carriers in (In,Ga)As/GaAs quantum dots and quantum wells*. Diss. Faculty of Physics, Dortmund University, 2007.

[Gre07b] A. Greilich, A. Shabaev, D. R. Yakovlev, Al. L. Efros, I. A. Yugova, D. Reuter, A. D. Wieck, M. Bayer: *Nuclei-Induced Frequency Focusing of Electron Spin Coherence*. Science **317**, 1896-1899 (2007).

[Gre07c] A. Greilich, M. Wiemann, F. G. G. Hernandez, D. R. Yakovlev, I. A. Yugova, M. Bayer, A. Shabaev, Al. L. Efros, D. Reuter, A. D. Wieck: *Robust manipulation of electron spin coherence in an ensemble of singly charged quantum dots*. Phys. Rev. B **75**, 233301 (2007).

[Gre09a] A. Greilich, S. E. Economou, S. Spatzek, D. R. Yakovlev, D. Reuter, A. D. Wieck, T. L. Reinecke, M. Bayer: *Ultrafast optical rotations of electron spins in quantum dots*. Nat. Phys. **5**, 262-266 (2009).

[Gre09b] A. Greilich, S. Spatzek, I. A. Yugova, I. A. Akimov, D. R. Yakovlev, Al. L. Efros, D. Reuter, A. D. Wieck, M. Bayer: *Collective single-mode precession of electron spins in an ensemble of singly charged (In,Ga)As/GaAs quantum dots*. Phys. Rev. B **79**, 201305 (2009).

[Gre11] A. Greilich, S. G. Carter, D. Kim, A. S. Bracker, D. Gammon: *Optical control of one and two hole spins in interacting quantum dots*. Nat. Photon. **5**, 702 (2011).

[God12] T. M. Godden, J. H. Quilter, A. J. Ramsay, Y. Wu, P. Brereton, S. J. Boyle, I. J. Luxmoore, J. Puebla-Nunez, A. M. Fox, M. S. Skolnick: *Coherent Optical Control of the Spin of a Single Hole in an InAs/GaAs Quantum Dot*. Phys. Rev. Lett. **108**, 017402 (2012).

[Gru02] D. Grundler: *Spintronics*. Physics World **15**, 39 (2002).

[Gul03] S. Gulde, M. Riebe, G. P. T. Lancaster, C. Becher, J. Eschner, H. Häffner, F. Schmidt-Kaler, I. L. Chuang, R. Blatt: *Implementation of the Deutsch–Jozsa algorithm on an ion-trap quantum computer*. Nature **421**, 48 (2003).

[Gyw10] O. Gywat, H. J. Krenner, J. Berezovsky: *Spins in Optically Active Quantum Dots*. WILEY-VCH, Weinheim 2010.

[Hen07] K. Hennessy, A. Badolato, M. Winger, D. Gerace, M. Atatüre, S. Gulde, S. Fält, E. L. Hu, A. Imamoglu: *Quantum nature of a strongly coupled single quantum dot-cavity system*. Nature **445**, 896 (2007).

[Her96] M. A. Herman, H. Sitter: *Molecular Beam Epitaxy*. Springer, Berlin 1996.

[Her08] F. G. G. Hernandez, A. Greilich, F. Brito, M. Wiemann, D. R. Yakovlev, D. Reuter, A. D. Wieck, M. Bayer: *Temperature-induced spin-coherence dissipation in quantum dots*. Phys. Rev. B **78**, 041303(R) (2008).

[Ivc04] E. L. Ivchenko: *Optical Spectroscopy of Semiconductor Nanostructures*. Springer, Berlin 2004.

[Jon98] J. A. Jones, M. Mosca, R. H. Hansen: *Implementation of a quantum search algorithm on a quantum computer*. Nature **393**, 344 (1998).

[Kan08] M. Kaniber, A. Laucht, A. Neumann, J. M. Villas-Boas, M. Bichler, M.-C. Amann, J. J. Finley: *Investigation of the nonresonant dot-cavity coupling in two-dimensional photonic crystal nanocavities*. Phys. Rev. B **77**, 161303(R) (2008).

[Kes90] H. W. van Kesteren, E. C. Cosman, W. A. J. A. van der Poel, C. T. Foxon: *Fine structure of excitons in type-II GaAs/AlAs quantum wells*. Phys. Rev. B **41**, 5283 (1990).

[Kha02] A. V. Khaetskii, D. Loss, L. Glazman: *Electron Spin Decoherence in Quantum Dots due to Interaction with Nuclei*. Phys. Rev. Lett. **88**, 186802 (2002).

[Kik98] J. M. Kikkawa, D. D. Awschalom: *Resonant Spin Amplification in n-Type GaAs*. Phys. Rev. Lett. **80**, 4313 (1998).

[Kit89] C. Kittel: *Einführung in die Festkörperphysik*. 8th edition. Oldenbourg, München 1989.

[Kop07] K. Kopitzki, P. Herzog: *Einführung in die Festkörperphysik*. 6th edition. Teubner, Wiesbaden 2007.

[Kot01] R. Kotlyar, T. L. Reinecke, M. Bayer, A. Forchel: *Zeeman spin splittings in semiconductor nanostructures*. Phys. Rev. B **63**, 085310 (2001).

[Kou04] A. V. Koudinov, I. A. Akimov, Yu. G. Kusrayev, F. Henneberger: *Optical and magnetic anisotropies of the hole states in Stranski-Krastanov quantum dots*. Phys. Rev. B **70**, 241305(R) (2004).

[Kre09] O. Krebs, E. Benjamin, A. Lemaître: *Magnetic anisotropy of singly Mn-doped InAs/GaAs quantum dots.* Phys. Rev. B **80**, 165315 (2009).

[Kri05] D. N. Krizhanovskii, A. Ebbens, A. I. Tartakovskii, F. Pulizzi, T. Wright, M. S. Skolnick, and M. Hopkinson: *Individual neutral and charged* $In_xGa_{1-x}As$*-GaAs quantum dots with strong in-plane optical anisotropy.* Phys. Rev. **B** 72, 161312(R) (2005).

[Kro04] M. Kroutvar, Y. Ducommun, D. Heiss, M. Bichler, D. Schuh, G. Abstreiter, J. J. Finley: *Optically programmable electron spin memory using semiconductor quantum dots.* Nature **432**, 81 (2004).

[Kun86] H.-J. Kunze: *Physikalische Messmethoden.* Teubner, Stuttgart 1986.

[Lee08] B. Lee, W. M. Witzel, D. Das Sarma: *Universal Pulse Sequence to Minimize Spin Dephasing in the Central Spin Decoherence Problem.* Phys. Rev. Lett. **100**, 160505 (2008).

[Lég07] Y. Léger, L. Besombes, L. Maingault, H. Mariette: *Valence-band mixing in neutral, charged, and Mn-doped self-assembled quantum dots.* Phys. Rev. B **76**, 045331 (2007).

[Llo93] S. Lloyd: *A Potentially Realizable Quantum Computer.* Science **261**, 1569 (1993).

[Lü05] C. Lü, J. L. Cheng, M. W. Wu: *Hole spin relaxation in semiconductor quantum dots.* Phys. Rev. B **71**, 075308 (2005).

[Lut56] J. M. Luttinger: *Quantum Theory of Cyclotron Resonance in Semiconductors: General Theory.* Phys. Rev. **102**, 1030 (1956).

[Mal09] P. Maletinsky, A. Imamoglu: *Quantum Dot Nuclear Spin Polarization.* P. Michler (Ed.): *Single Semiconductor Quantum Dots*, 145-184. Springer Berlin 2009.

[Med13] J. Medford, J. Beil, J. M. Taylor, S. D. Bartlett, A. C. Doherty, E. I. Rashba, D. P. DiVincenzo, H. Lu, A. C. Gossard, C. M. Marcus: *Self-consistent measurement and state tomography of an exchange-only spin qubit.* Nat. Nanotech. **8**, 654 (2013).

[Mei58] S. Meiboom, D. Gill: *Modified Spin-Echo Method for Measuring Nuclear Relaxation Times.* Rev. Sci. Instrum. **29**, 688 (1958).

[Mer02] I. A. Merkulov, Al. L. Efros, M. Rosen: *Electron spin relaxation by nuclei in semiconductor quantum dots.* Phys. Rev. B **65**, 205309 (2002).

[Mon11] T. Monz, P. Schindler, J. T. Barreiro, M. Chwalla, D. Nigg, W. A. Coish, M. Harlander, W. Hänsel, M. Hennrich, R. Blatt: *14-Qubit Entanglement: Creation and Coherence.* Phys. Rev. Lett. **106**, 130506 (2011).

[Now07] K. C. Nowack, F. H. L. Koppens, Y. V. Nazarov, L. M. K. Vandersypen: *Coherent Control of a Single Electron Spin with Electric Fields.* Science **318**, 1430 (2007).

[Oul07] R. Oulton, A. Greilich, S. Yu. Verbin, R. V. Cherbunin, T. Auer, D. R. Yakovlev, M. Bayer, I. A. Merkulov, V. Stavarache, D. Reuter, A. D. Wieck: *Subsecond Spin Relaxation Times in Quantum Dots at Zero Applied Magnetic Field Due to a Strong Electron-Nuclear Interaction.* Phys. Rev. Lett. **98**, 107401 (2007).

[Pai11] H. Paik, D. I. Schuster, L. S. Bishop, G. Kirchmair, G. Catelani, A. P. Sears, B. R. Johnson, M. J. Reagor, L. Frunzio, L. I. Glazman, S. M. Girvin, M. H. Devoret, R. J. Schoelkopf: *Observation of High Coherence in Josephson Junction Qubits Measured in a Three-Dimensional Circuit QED Architecture.* Phys. Rev. Lett. **107**, 240501 (2011).

[Pet08] M. Yu. Petrov, I. V. Ignatiev, S. V. Poltavtsev, A. Greilich, A. Bauschulte, D. R. Yakovlev, M. Bayer: *Effect of thermal annealing on the hyperfine interaction in InAs/GaAs quantum dots.* Phys. Rev. B **78**, 045315 (2008).

[Pet05] J. R. Petta, A. C. Johnson, J. M. Taylor, E. A. Laird, A. Yacoby, M. D. Lukin, C. M. Marcus, M. P. Hanson, A. C. Gossard: *Coherent Manipulation of Coupled Electron Spins in Semiconductor Quantum Dots.* Science **309**, 2180-2184 (2005).

[Pie02] C. Piermarocchi, P. Chen, L.J. Sham, D.G. Steel: *Optical RKKY Interaction between Charged Semiconductor Quantum Dots.* Phys. Rev. Lett. **89**, 167402 (2002).

[Pre07] D. Press, S. Götzinger, S. Reitzenstein, C. Hofmann, A. Löffler, M. Kamp, A. Forchel, and Y. Yamamoto: *Photon Antibunching from a Single Quantum-Dot-Microcavity System in the Strong Coupling Regime.* Phys. Rev. Lett. **98**, 117402 (2007).

[Rot59] L. M. Roth, B. Lax, S. Zwerdling: *Theory of Optical Magneto-Absorption Effects in Semiconductors.* Phys. Rev. **114**, 90 (1959).

[Sch02] F. Schwabl: *Quantenmechanik.* 6th edition. Springer, Berlin 2002.

[Sch11] A. Schwan, B.-M. Meiners, A. B. Henriques, A. D. B. Maia, A. A. Quivy, S. Spatzek, S. Varwig, D. R. Yakovlev, M. Bayer: *Dispersion of electron* *g-factor with optical transition energy in (In,Ga)As/ GaAs self-assembled quantum dots.* Appl. Phys. Lett. **98**, 233102 (2011).

[Sem07] Y. G. Semenov, K. W. Kim: *Elastic spin-relaxation processes in semiconductor quantum dots.* Phys. Rev. B **75**, 195342 (2007).

[Sik01] V. Siklitsky: *Physical Properties of Semiconductors.* - `http://www.ioffe.ru/SVA/NSM/Semicond/index.html` on 11-27-2013, Ioffe Physico-Technical Institute St. Petersburg 2001.

[Sha03] A. Shabaev, Al. L. Efros, D. Gammon, I. A. Merkulov: *Optical readout and initialization of an electron spin in a single quantum dot.* Phys. Rev. B **68**, 201305 (2003).

[Sho97] P. W. Shor: *Polynomial-Time Algorithms for Prime Factorization and Discrete Logarithms on a Quantum Computer.* SIAM J. Comput. **26**, 1484-1509 (1997).

[Shu12] M. D. Shulman, O. E. Dial, S. P. Harvey, H. Bluhm, V. Umansky, A. Yacoby: *Demonstration of Entanglement of Electrostatically Coupled Singlet-Triplet Qubits.* Science **336**, 202 (2012).

[Sou12] A. M. Souza, G. A. Álvarez, D. Suter: *Robust dynamical decoupling.* Philos. T. Roy. Soc. A **370**, 4748 (2012).

[Spa11a] S. Spatzek: *Kohärente Kontrolle und Wechselwirkung von Elektronenspins in einem (In,Ga)As/GaAs Quantenpunktensemble.* Diss. Faculty of Physics, TU Dortmund University, 2011.

[Spa11b] S. Spatzek, S. Varwig, M. M. Glazov, I. A. Yugova, A. Schwan, D. R. Yakovlev, D. Reuter, A. D. Wieck, M. Bayer: *Generation and detection of mode-locked spin coherence in (In,Ga)As/GaAs quantum dots by laser pulses of long duration.* Phys. Rev. B **84**, 115309 (2011).

[Spa11c] S. Spatzek, A. Greilich, S. E. Economou, S. Varwig, A. Schwan, D. R. Yakovlev, D. Reuter, A. D. Wieck, T. L. Reinecke, M. Bayer: *Optical Control of Coherent Interactions between Electron Spins in InGaAs Quantum Dots.* Phys. Rev. Lett. **107**, 137402 (2011).

[Ste98] A. Steane: *Quantum computing.* Rep. Prog. Phys. **61**, 117–173 (1998).

[Sti01] T. H. Stievater, Xiaoqin Li, D. G. Steel, D. Gammon, D. S. Katzer, D. Park, C. Piermarocchi, L. J. Sham: *Rabi Oscillations of Excitons in Single Quantum Dots.* Phys. Rev. Lett. **87**, 133603 (2001).

[Sto04] J. Stolze, D. Suter: *Quantum Computing.* WILEY-VCH, Weinheim 2004.

[Str39] I. N. Stranski, L. Krastanov: *Abhandlungen der Mathematisch-Naturwissenschaftlichen Klasse.* Akad. Wiss. Lit. Mainz **146**, 797 (1939).

[Tes09] C. Testelin, F. Bernardot, B. Eble, M. Chamarro: *Hole-spin dephasing time associated with hyperfine interaction in quantum dots.* Phys. Rev. B **79**, 195440 (2009).

[Tri09] M. Trif, P. Simon, D. Loss: *Relaxation of Hole Spins in Quantum Dots via Two-Phonon Processes.* Phys. Rev. Lett **103**, 106601 (2009).

[Tsi02] E. Tsitsishvili, R. v. Baltz, H. Kalt: *Temperature dependence of polarization relaxation in semiconductor quantum dots.* Phys. Rev. B **66**, 161405(R) (2002).

[Uhr07] G. S. Uhrig: *Keeping a Quantum Bit Alive by Optimized π-Pulse Sequences.* Phys. Rev. Lett. **98**, 100504 (2007).

[Vag02] A. Vagov, V. M. Axt, T. Kuhn: *Electron-phonon dynamics in optically excited quantum dots: Exact solution for multiple ultrashort laser pulses.* Phys. Rev. B **66**, 165312 (2002).

[Van05] L. M. K. Vandersypen, I. L. Chuang: *NMR techniques for quantum control and computation.* Rev. Mod. Phys. **76**, 1037 (2005).

[Var12] S. Varwig, A. Schwan, D. Barmscheid, C. Müller, A. Greilich, I. A. Yugova, D. R. Yakovlev, D. Reuter, A. D. Wieck, M. Bayer: *Hole spin precession in a (In,Ga)As quantum dot ensemble: From resonant spin amplification to spin mode locking.* Phys. Rev. B **86**, 075321 (2012).

[Var13] S. Varwig, A. René, A. Greilich, D. R. Yakovlev, D. Reuter, A. D. Wieck, M. Bayer: *Temperature dependence of hole spin coherence in (In,Ga)As quantum dots measured by mode-locking and echo techniques.* Phys. Rev. B **87**, 115307 (2013).

[Var14a] S. Varwig, A. Greilich, D. R. Yakovlev, M. Bayer: *Spin mode-locking in quantum dots revisited.* Phys. Status Solidi B **251**, 1892–1911 (2014).

[Var14b] S. Varwig, A. René, S. E. Economou, A. Greilich, D. R. Yakovlev, D. Reuter, A. D. Wieck, T. L. Reinecke, M. Bayer: *All-optical tomography of electron spins in (In,Ga)As quantum dots.* Phys. Rev. B **89**, 081310(R) (2014).

[Var14c] S. Varwig, I. A. Yugova, A. René, T. Kazimierczuk, A. Greilich, D. R. Yakovlev, D. Reuter, A. D. Wieck, M. Bayer: *Excitation of complex spin dynamics patterns in a quantum dot electron spin ensemble.* Phys. Rev. B **90**, 121301(R) (2014).

[Var14d] S. Varwig, E. Evers, A. Greilich, D. R. Yakovlev, D. Reuter, A. D. Wieck, M. Bayer: *All-optical implementation of a dynamic decoupling protocol for hole spins in (In,Ga)As quantum dots*. Phys. Rev. B, **90**, 121306(R) (2014).

[Wan12] X. J. Wang, S. Chesi, W. A. Coish: *Spin-Echo Dynamics of a Heavy Hole in a Quantum Dot*. Phys. Rev. Lett. **109**, 237601 (2012).

[War13] R. J. Warburton: *Single spins in self-assembled quantum dots*. Nat. Mat. **12**, 483 (2013).

[Way61] K. Way, N. B. Gove, C. L. Nakasima: *References for* $A = 21$ *to* $A = 212$. A. M. Hellwege, K. H. Hellwege (Eds.): *Energie-Niveaus der Kerne:* $A = 5$ *bis* $A = 257$ - Landolt-Börnstein Neue Serie - Gruppe I: Kernphysik und Kerntechnik, Band I, 2-242. Springer, Berlin 1961.

[Wei13] H. Weimer, N. Y. Yao, M. D. Lukin: *Collectively Enhanced Interactions in Solid-State Spin Qubits* . Phys. Rev. Lett. **110**, 067601 (2013).

[Win09] M. Winger, T. Volz, G. Tarel, S. Portolan, A. Badolato, K. J. Hennessy, E. L. Hu, A. Beveratos, J. J. Finley, V. Savona, A. Imamoglu: *Explanation of Photon Correlations in the Far-Off-Resonance Optical Emission from a Quantum-Dot-Cavity System*. Phys. Rev. Lett. **103**, 207403 (2009).

[Wol01] S. A. Wolf, D. D. Awschalom, R. A. Buhrman, J. M. Daughton, S. von Molnár, M. L. Roukes, A. Y. Chtchelkanova, D. M. Treger: *Spintronics: A Spin-Based Electronics Vision for the Future*. Science **294**, 1488 (2001).

[Yan11] W. Yang, Z.-Y. Wang, R.-B. Liu: *Preserving qubit coherence by dynamical decoupling*. Front. Phys. **6**, 2-14 (2011).

[Yug09] I. A. Yugova, M. M. Glazov, E. L. Ivchenko, Al. L. Efros: *Pump-probe Faraday rotation and ellipticity in an ensemble of singly charged quantum dots*. Phys. Rev. B **80**, 104436 (2009).

[Yug12] I. A. Yugova, M. M. Glazov, D. R. Yakovlev, A. A. Sokolova, M. Bayer: *Coherent spin dynamics of electrons and holes in semiconductor quantum wells and quantum dots under periodical optical excitation: Resonant spin amplification versus spin mode locking*. Phys. Rev. B **85**, 125304 (2012).

[Zhu12] E. A. Zhukov, O. A. Yugov, I. A. Yugova, D. R. Yakovlev, G. Karczewski, T. Wojtowicz, J. Kossut, M. Bayer: *Resonant spin amplification of resident electrons in CdTe/(Cd,Mg)Te quantum wells subject to tilted magnetic fields*. Phys. Rev. B **86**, 245314 (2012).

[Zib05] E. Zibik, A. Andreev, L. Wilson, M. Steer, R. Green, W. Ng, J. Cockburn, M. Skolnick, M. Hopkinson: *Effect of the electron population on intraband absorption in InAs/GaAs self-assembled quantum dots*. Physica E (Amsterdam) **26**, 105 (2005).

[Zve97] A. K. Zvezdin, V. A. Kotov: *Modern Magnetooptics and Magnetooptical Materials*. Institute of Physics, London 1997.

List of Publications

1. M. M. Glazov, I. A. Yugova, S. Spatzek, A. Schwan, **S. Varwig**, D. R. Yakovlev, D. Reuter, A. D. Wieck, M. Bayer: *Effect of pump-probe detuning on the Faraday rotation and ellipticity signals of mode-locked spins in (In,Ga)As/GaAs quantum dots.* Phys. Rev. B **82**, 155325 (2010).

2. A. Schwan, B.-M. Meiners, A. B. Henriques, A. D. B. Maia, A. A. Quivy, S. Spatzek, **S. Varwig**, D. R. Yakovlev, M. Bayer: *Dispersion of electron g-factor with optical transition energy in (In,Ga)As/ GaAs self-assembled quantum dots.* Appl. Phys. Lett. **98**, 233102 (2011).

3. S. Spatzek, **S. Varwig**, M. M. Glazov, I. A. Yugova, A. Schwan, D. R. Yakovlev, D. Reuter, A. D. Wieck, M. Bayer: *Generation and detection of mode-locked spin coherence in (In,Ga)As/GaAs quantum dots by laser pulses of long duration.* Phys. Rev. B **84**, 115309 (2011).

4. S. Spatzek, A. Greilich, S. E. Economou, **S. Varwig**, A. Schwan, D. R. Yakovlev, D. Reuter, A. D. Wieck, T. L. Reinecke, M. Bayer: *Optical Control of Coherent Interactions between Electron Spins in InGaAs Quantum Dots.* Phys. Rev. Lett. **107**, 137402 (2011).

5. A. Schwan, **S. Varwig**, A. Greilich, D. R. Yakovlev, D. Reuter, A. D. Wieck, M. Bayer: *Non-resonant optical excitation of mode-locked electron spin coherence in (In,Ga)As/GaAs quantum dot ensemble.* Appl. Phys. Lett. **100**, 232107 (2012).

6. **S. Varwig**, A. Schwan, D. Barmscheid, C. Müller, A. Greilich, I. A. Yugova, D. R. Yakovlev, D. Reuter, A. D. Wieck, M. Bayer: *Hole spin precession in a (In,Ga)As quantum dot ensemble: From resonant spin amplification to spin mode locking.* Phys. Rev. B **86**, 075321 (2012).

7. A. B. Henriques, A. Schwan, **S. Varwig**, A. D. B. Maia, A. A. Quivy, D. R. Yakovlev, M. Bayer: *Spin coherence generation in negatively charged self-assembled (In,Ga)As quantum dots by pumping excited trion states.* Phys. Rev. B **86**, 115333 (2012).

8. **S. Varwig**, A. René, A. Greilich, D. R. Yakovlev, D. Reuter, A. D. Wieck, M. Bayer: *Temperature dependence of hole spin coherence in (In,Ga)As quantum dots measured by mode-locking and echo techniques.* Phys. Rev. B **87**, 115307 (2013).

9. **S. Varwig**, A. Greilich, D. R. Yakovlev, M. Bayer: *Spin mode-locking in quantum dots revisited.* Phys. Status Solidi B **251**, 1892–1911 (2014).
10. **S. Varwig**, A. René, S. E. Economou, A. Greilich, D. R. Yakovlev, D. Reuter, A. D. Wieck, T. L. Reinecke, M. Bayer: *All-optical tomography of electron spins in (In,Ga)As quantum dots.* Phys. Rev. B **89**, 081310(R) (2014).
11. **S. Varwig**, I. A. Yugova, A. René, T. Kazimierczuk, A. Greilich, D. R. Yakovlev, D. Reuter, A. D. Wieck, M. Bayer: *Excitation of complex spin dynamics patterns in a quantum dot electron spin ensemble.* Phys. Rev. B **90**, 121301(R) (2014).
12. **S. Varwig**, E. Evers, A. Greilich, D. R. Yakovlev, D. Reuter, A. D. Wieck, M. Bayer: *All-optical implementation of a dynamic decoupling protocol for hole spins in (In,Ga)As quantum dots.* Phys. Rev. B, **90**, 121306(R) (2014).

Acknowledgment

Finally, I would like to thank all the people whose support, help, and encouragement were essential for the completion of this thesis. First, I would like to thank my supervisor Prof. Manfred Bayer for his ideas, his scientific experience and the fruitful collaboration. I am grateful for the opportunity to work at his chair and the support with high-quality equipment. I also thank Prof. Dmitri Yakovlev for sharing his scientific opinion as well as Prof. Dietmar Fröhlich and Dr. Ilya Akimov for giving helpful advice several times. Great thanks go to Lars Wieschollek, Thomas Stöhr, and especially Michaela Wäscher and Klaus Wiegers for tremendous technical and administrative support. We can be glad to have them at E2.

In the laboratory, I learned the most from Stefan Spatzek who introduced me to the pump-probe setup and the experimental work. I am thankful for his company during the first steps of the tomography experiment. I would also like to thank Prof. Evgeny Zhukov for the nice atmosphere in the lab, his helping hands and several tricks and jokes that made work easier. I am very grateful to have Alexander Schwan as a coworker in the lab for most of the time. His drive, his sense for the experiments and devices, and his unreserved helpfulness motivated and supported me a lot. I very much appreciate the collaboration of Crispin Müller, Dennis Barmscheid, Alexandre René, Eiko Evers, and Johannes Thewes, whose work in the lab and during the data analysis contributed to the results presented in this thesis. Whenever I had an experimental problem or a theoretical question, Alex Greilich, Jörg Debus, Tomasz Kazimierczuk, or Irina Yugova - who I would also like to thank explicitly together with Sophia Economou for their theoretical calculations to my experimental work - could solve or answer it, or at least tried to.

All other colleagues and former members of E2 also deserve my appreciation as they form a great environment where colleagues soon become friends. I hope everybody addressed here knows that he or she is meant. Furthermore, I am sincerely thankful for the proofreading by Lukas Langer and Björn Röbke. I will return the favor! At the end, I want to express my deep gratitude to my family, who supported me - not only financially but also emotionally - all the time.

Thank you very much!